DOTTORATO DI RICERCA IN
ELECTRONICS AND TELECOMMUNICATIONS

SCUOLA DI DOTTORATO IN
INFORMATION AND COMMUNICATION TECHNOLOGIES

XXIV CICLO

UNIVERSITÀ DEGLI STUDI DI MODENA E REGGIO EMILIA

DIPARTIMENTO DI INGEGNERIA DELL'INFORMAZIONE

TESI PER IL CONSEGUIMENTO DEL TITOLO DI DOTTORE DI RICERCA

METHODS OF ESTIMATION OF OCULAR HEMODYNAMICS IN HUMAN FUNDUS USING LASER DOPPLER FLOWMETRY AND OCULAR FUNDUS REFLECTOMETRY

Tesi di:
NITHIYANANTHAM PALANISAMY
Relatore:
Prof. LUIGI ROVATI
Il Direttore:
Prof. GIORGIO MATTEO VITETTA

DEGREE OF DOCTOR OF PHILOSOPHY IN
ELECTRONICS AND TELECOMMUNICATIONS

DOCTORATE SCHOOL IN
INFORMATION AND COMMUNICATION TECHNOLOGIES

XXIV CYCLE

UNIVERSITY OF MODENA AND REGGIO EMILIA

INFORMATION ENGINEERING DEPARTMENT

Ph.D. DISSERTATION

METHODS OF ESTIMATION OF OCULAR HEMODYNAMICS IN HUMAN FUNDUS USING LASER DOPPLER FLOWMETRY AND OCULAR FUNDUS REFLECTOMETRY

Candidate:
NITHIYANANTHAM PALANISAMY
Advisor:
Prof. LUIGI ROVATI
The Director of the School:
Prof. GIORGIO MATTEO VITETTA

Acknowledgement

This thesis arose in part out of years of research that has been done since I came to Optolab, University of Modena and Reggio Emilia. By that time, I have worked with a great number of people whose contribution in assorted ways to the research and the making of the thesis deserved special mention. It is a pleasure to convey my gratitude to them all in my humble acknowledgment.

Foremost, I would like to express my sincere gratitude to my advisor Dr. Luigi Rovati for the continuous support of my Ph.D study and research, for his patience, motivation, enthusiasm, and immense knowledge. His guidance helped me in all the time of research and writing of this thesis. I could not have imagined having a better advisor and mentor for my Ph.D study.

I gratefully acknowledge Dr. Charles E Riva for his advice, supervision, and crucial contribution, which made him a backbone of this research and so to this thesis. His involvement with his originality has triggered and nourished my intellectual maturity that I will benefit from, for a long time to come.

Many thanks go in particular to Dr. Matteo Bonaiuti and Dr. Stefano Cattini. I am much indebted to Matteo for his valuable advice in development of image acquition system and spending his precious times with me working on this instrument and gave his critical comments about it. I have also benefited by advice and guidance from Stefano who also always kindly grants me his time even for answering some of my unintelligent questions about optical measurements.

I would like to acknowledge the enormous support and encouragement of my friends and colleagues at Modena and Ophthalmic clinic, University of Bologna, with whom I have had the pleasure of working over the years. These include Dr. Mauro Cellini, Dr. Corrado Gizzi, Dr. Ernesto Strobbe, Paolo Santinelli, Luca Ferrari, Dr. Vijayaharan A Venugopal, other friends, well-wishers and researchers in ICT doctorate school.

I would like to thank members of Ophthalmic Clinic, University of Bologna for supporting my research activities and also for arranging subjects for my research activity.

I would like to thank the Director and all Professors in the Department of Information Engineering at the University of Modena and Reggio Emilia.

Where would I be without my family? My parents deserve special mention for their inseparable support and prayers. My Father, Palanisamy kolanthaiah, in the first place is the person who put the fundament my learning character, showing me the joy of intellectual pursuit ever since I was a child. My Mother, Ramathal, is the one who sincerely raised me with her caring and gently love.

Words fail me to express my appreciation to my wife Manimegalai, whose dedication, love and persistent confidence in me, has taken the load off my shoulder. I owe her for being unselfishly let her intelligence, passions, and ambitions collide with mine.

I would like to thank my daughter Indhu Shri and son Shayam Kaarthick for their love and care.

Finally I would like to thank the god almighty to give ways for me to complete my thesis.

Contents

List of Tables

List of Figures

Introduction

Millions of people all over the world affected from different types of ocular disease. The recent report on ocular diseases by world health organisation (WHO) focuses on four disorders that pose the greatest threats to vision after the age of 40: cataract, glaucoma, age-related macular degeneration, and diabetic retinopathy. Cataract is the single most prevalent cause of blindness in the world, accounting for upto 80% of mass blindness. There are lot of methods are used to detect and differentiate the diseases and based on the detection, new treatment methods are proposed. However, they do not provide any relationship between blood flow and ocular diseases. My research activities mainly focused on non-invasive optical techniques for blood flow measurements.

The application of laser Doppler techniques for investigation of blood flow in the posterior segment of human eye has provided much useful information on the physiology of ocular blood flow in the retina, optic nerve head and choroid [1] and alterations in perfusion in these tissues in diseases [2]. Laser Doppler flowmetry (LDF) is a non-invasive technique to investigate ocular microvascular hemodynamics in humans. The technique was introduced into the field of biomedical engineering in the year 1970. LDF parameters derived from the model of Bonner and Nossal [3] was first applied to the human eye by Riva et al [4]. LDF has number of limitations that may have reduced the clinical impact of the technique.

LDF measurements depends on the scattering geometry defined by the directions of the incident and scattered laser beams, the separation between theses beams at the sampled volume [5] and the scattering properties of the tissue [6].

Timolol-maleate, a non-selective β-adrenergic receptor blocking agent that commonly used to lowers intraocular pressure (IOP) in ocular hypertensive and glaucoma patients. Most of my research is focused on measurement of blood flow in the choroidal region of human fundus. The present thesis is proposed to report the effect of timolol on heart rate, IOP and choroidal blood flow (ChBF). LDF measurements do not provide absolute blood flow measurements, because of uncertainty in knowing the sampling volume. Changes in pupil diameter resulted in larger scattering angles for the beam emerging out of the pupil and bigger variations of the location of the incident beam at the pupil. Both presumably affect the LDF values and their variability. In this thesis, a new method is proposed to reduce the variability and increase the sensitivity of LDF measurements for the study of various pharmacological agents on ChBF.

Optical imaging of human retina is a novel method to estimate spatial and temporal activation properties of retinal layers can be revealed in normal and pathologic states. The basic principle of functional imaging of human retina is to study the characteristics of the visual stimulus induced hemodynamical response in different regions of the eye [7]. The reflectance changes are originated from visual stimulus induced changes in the light scattering and light absorbance changes associated with metabolic and hemodynamic changes in blood volume or the oxygenated state of haemoglobin of neural tissues [8]. Neural activation of ocular tissues is predominant at near-infrared wavelengths causes decrease in reflectance due to decreased scattering of light. The reflectance changes are very small, and the changes induced by visual stimulus on neural activity are less than 1 % of total reflectance of light from the ocular tissues. In this thesis, I have reported the development of an instrument for functional imaging of human ocular fundus in near infrared wavelength at 770 nm and the reflectance changes in response to diffuse flicker stimulation at three wavelengths (430, 523 and 572 nm).

Chapter 1 introduces different type of ophthalmic instrumentation used in clinical application.

Chapter 2 reports the theoretical background, development and practical considerations behind laser Doppler flowmetry and ocular fundus reflectometry.

Chapter 3 describes the experimental setup and measurements of effect of timolol on subfoveal choroidal blood flow (ChBF)

Chapter 4 describes the effect of tropicamide on scattering geometry and the technique to reduce the variability in LDF measurements

Chapter 5 describes the development of functional imaging system and visual stimulus induced changes in human near-infrared fundus

CHAPTER 1

Ophthalmic Instrumentation

During the last twenty years, there have been rapid and often dramatic developments in the applications of technology in medicine and health care. Several major eye diseases may be characterized by deficits in ocular blood flow [9]. There are many instruments that the eye doctors might use to evaluate the eye and vision system. The most commonly used instruments in ophthalmology were divided into two sections: instruments for the diagnosis of eye health and instruments used to determine the status of the vision system.

1.1 Instruments for eye health evolution

The crucial part of eye health evolution is determining the health of retina and the vitreous humor. The ophthalmoscope or funduscope allows the health professionals to see the inside fundus of the eye during the physical examination. The commonly used ophthalmoscopes were either direct or indirect types.

The direct ophthalmoscopes are handheld device and produces images in upright and un-reversed with approximately 15 times magnification. The direct ophthalmoscope was used to examine the back of the eye; the back of the eye constitutes optic nerve, blood vessels, the macula and the fundus. It can also detect changes in the clarity or obstructions in the normally transparent ocular media. The instrument was located at about few millimetres in front of the pupil for viewing the back of the eye. On the other hand, the indirect ophthalmoscope constitutes a light mounted headband and a handheld lens produces inverted and reversed images with approximately about 3 times magnification.

(a) (b)

Figure 1.1 Ophthalmoscopes. (a) Direct Ophthalmoscope and (b) Indirect Ophthalmoscope

The slit lamp instrument consists of a high-intensity light source. It can be focused to shine a thin sheet of light into the eye. The slit-lamp bio-microscope provides a high magnification view of the front structures of the eye, including the cornea, iris and lens, and with the use of the condensing lens, it allows a detailed, stereoscopic view of the retina. It is used to detect tissue damage to the ocular surface including the cornea, conjunctiva and lids. It can also detect inflammation of the internal structures, cataract changes of the crystalline lens and more. It is used extensively for the fitting of contact lenses and detecting contact lens related to tissue changes in the cornea and surrounding tissues.

Figure 1.2 Slit-lamp microscope

Figure 1.3 Visual field tester

The visual field tester is a primary tool detects the vision field loss due to glaucoma, retinal tears, artery and vein occlusions and tumours along the optic nerve pathway and brain [10]. Visual field testing is essential in determining retina disease or neurological deficits in the visual pathways between the eye and the brain.

The recently developed Humphrey FDT (Frequency Doubling Technology) unit (Figure 1.3) offers a very rapid screening protocol and fast full-threshold comparative testing compared to the other devices. The patient observes an oscillating bar pattern which appears in various locations on a video screen in the unit and indicates that the subject see the image by pressing a mouse button on a clicker. Other field testers include the "big bowl" and "big box" units by a number of manufacturers. These are larger machines that display individual points of light on the inside of hemispherical shell. The patient sit and place the head just inside the box and observes the light show and, as with the FDT, indicates seeing the target by pressing a mouse button. For all machines, a software program plots the observed targets in the field and uses a database to compare patient responses to expected age-relative normals.

(a) (b) (c)

Figure 1.4 Intraocular pressure measuring instruments. (a) Goldman tonometer (b) Applanation meter (c) Ocular response analyser

Tonometer is a device that measures intraocular fluid pressure in human eyes. A portable Goldmann type tonometer was shown in Figure 1.4. The Goldman tonometer was gold standard for diagnostic testing of human eye pressure. Other

Goldmann tonometers are mounted on the slit lamp. These units require the use of fluorescein dye and, most often, a drop of topical anaesthetic. Ocular response analyser is one type of non-contact tonometer. The Ocular Response Analyzer utilizes a rapid air impulse, and an advanced electro-optical system to record two applanation pressure measurements; one while the cornea is moving inward, and the other as the cornea returns. Due to its biomechanical properties, the cornea resists the dynamic air puff causing delays in the inward and outward applanation events, resulting in two different pressure values.

1.2 Instruments for refractive error determination

Figure 1.5 Keratometer

The keratometer measures the curvature of the anterior cornea and determining the degree of astigmatism error. The keratometer is a useful instrument in diagnosing cornea diseases.

Figure 1.6 Corneal topographer

The automated topographer maps many data points on the surface of the cornea relating the curvature changes at different locations. The information is displayed on a video screen and can be printed out as hard copy using printers. The instrument is not used during the standard examination and widely used in the process of contact lens fitting. The automated topographer is very much helpful in the diagnosis of keratconus and in preparation for laser refractive surgery.

Figure 1.7 Retina Scope

The retina scope is a handheld device was used to determine the optical prescription and the lens power presents in the retina with help of clearly focused image. The retina scope projects a light source to the back of the eye. The operator made use of a dial to adjust the lens power required to focus that light source correctly on the retina. The retina scope is used routinely in ophthalmic clinics to test the refractive error.

The refractor or phoropter is an instrument with combination of lenses and prisms and used for optical correction. The data from the retina scope was used by the examiner subjectively adjusts the lens powers for optimum usefulness and patient comfort. The examiner asked questions to the subjects about the vision afforded by two different lenses. The examiner uses this information to fine tune the lens power. The initial settings of the phoropter were done by use of a retinoscope or any other automated refractor.

Figure 1.8 Phoropter

The major components of the phoropter are the JCC (Jackson Cross-Cylinder) used for astigmatism correction, Risley prisms to measure phorias and vergences, and the (+), (−), and cylinder lenses. From the measurements taken, the specialist will write an eyeglass prescription that contains at least 6 numerical specifications (3 for each eye): sphere, cylinder, and axis and possibly pupillary distance.

The lenses within a phoropter refract light in order to focus images on the patient's retina. The optical power of these lenses is measured in 0.25 diopter increments. The examiner is able to determine the spherical power, cylindrical power, and cylindrical axis necessary to correct a person's refractive error by changing the lenses. The presence of cylindrical power indicates the presence of astigmatism which has an axis measured from 0 to 180 degrees away from being aligned horizontally. The instrument contains many lenses and some of them used to present double image of the chart and compare the visions of the two eyes.

1.3 Instruments for blood flow measurements

The blood vessels of the iris and inner retina are observable through the clear cornea, and the blood flow measurement in the eye is extremely difficult. The simple approaches are ineffective to access the different vessels, capillaries and vascular beds. The clear optical path between cornea to retina leads to the basic principles in many optical imaging techniques.

Figure 1.9 Optical coherence tomography

Figure 1.10 Retinal vessel analyser

The film-based fundus photography is the oldest technique to assess the vessels and measure the blood flow. However, they are modified in the years to the instruments like scanning laser ophthalmoscopes and optical coherence tomography. The retinal vessel analyzer (Imedos, Jena, Germany), is a video based imaging technique mainly devoted for measuring retinal vessel diameters. The information about the retinal vessel is response of the alterations in the biological system due to internal or external mechanisms or due to drug. The measurement of velocity in the same vessel is used to calculate the volumetric blood flow. Such a velocity measurement on larger vessels is done with dual-beam laser Doppler velocimetry [11]. The blood flow in retinal artery, posterior ciliary arteries are measured with ultrasound Doppler imaging technique, and the blood flow in retinal and optic nerve head microcirculations are measured with Doppler speckle technique.

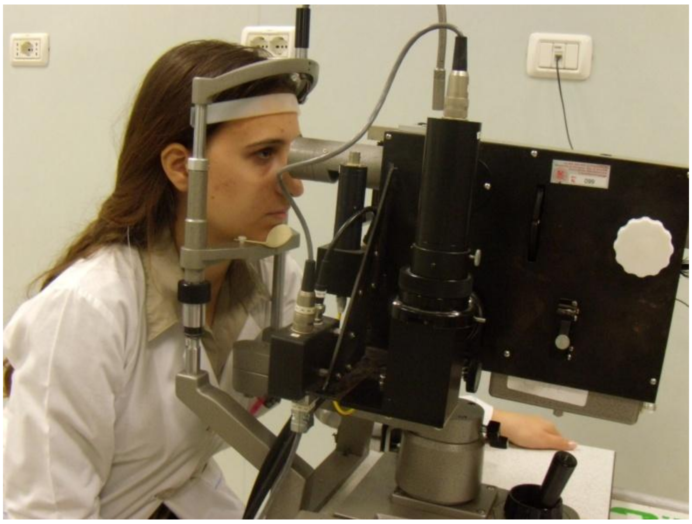

Figure 1.11 Laser Doppler flowmetry

Laser Doppler flowmetry (LDF) is a non-invasive technique based on fundus camera and fiber optic unit to provide relative measurement of red blood cell flux (the product of mean velocity and the mean volume) in a small area of laser-illuminated tissue. These techniques mainly used for blood flow measurement in optic nerve head, sub-foveal choroid, iris and small blood vessels. The advantage this technique is able to provide continuous real time blood flow measurements at different sites on the human ocular fundus.

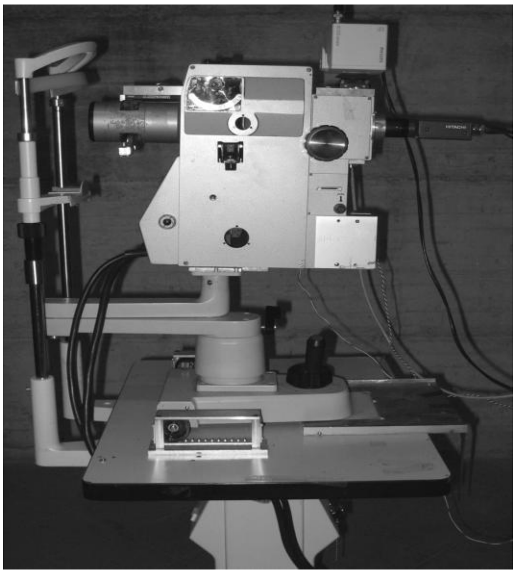

Figure 1.12 Ocular fundus reflectometry

Ocular fundus reflectometry is a technique aimed at the in-vivo measurement of reflectance of tissues of the ocular fundus. Its principle is based on imaging the changes in tissue reflectance of light are elicited by stimulus-induced changes in neuronal activity. Such reflectance changes are originate from stimulus-induced changes in light scattering properties of neural tissue, and from changes in light absorption associated with hemodynamic changes in blood volume. Imaging the stimulus-induced changes in near-infrared fundus reflectance in humans is a novel method for the study of the physiology of human visual system, and for early detection of disease states.

CHAPTER 2

Theoretical Background

Laser Doppler flowmetry

Laser Doppler flowmetry (LDF) is an accurate continuous non-invasive real-time measurement of flow of red blood cells in ocular tissue. The microvascular blood flow of red blood cell (RBC) is sometimes referred as ocular perfusion. Number of in-vitro and in-vivo experiments predicts LDF output has been shown to be reproducible and to correlate with ocular blood flow as estimated by other methods. "Doppler" refers to the frequency shift that arises in light that has been scattered by moving red blood cells (RBC) in blood vessels or capillaries in human eye. Laser Doppler Flowmetry (LDF) works by illuminating the tissue under observation with single frequency low power laser light and the blood flow was estimated by processing the frequency distribution of the backscattered light.

The first experimental studies using LDF were performed on rabbits using Helium-Neon laser in 1970 [12]. The instrumentation setups have been modified and improved over the years [13]. Laser Doppler perfusion monitoring (LDPM) is a continuous non-invasive optical fiber based technique used for assessing the quality of the microcirculation of the skin. In this system an optical fiber is used to guide the light from the laser source to the tissue and from the tissue to the detector. The laser Doppler perfusion imaging (LDPI) technique was developed to scan over the tissue of interest to from an image. The perfusion value in each scanning position is calculated and transformed into a pixel value, and the scanning procedure lasts for a couple of minutes to form an entire image. The detector is typically placed some 10-20 cm above the tissue surface. In some systems a lens focuses the light on the detector.

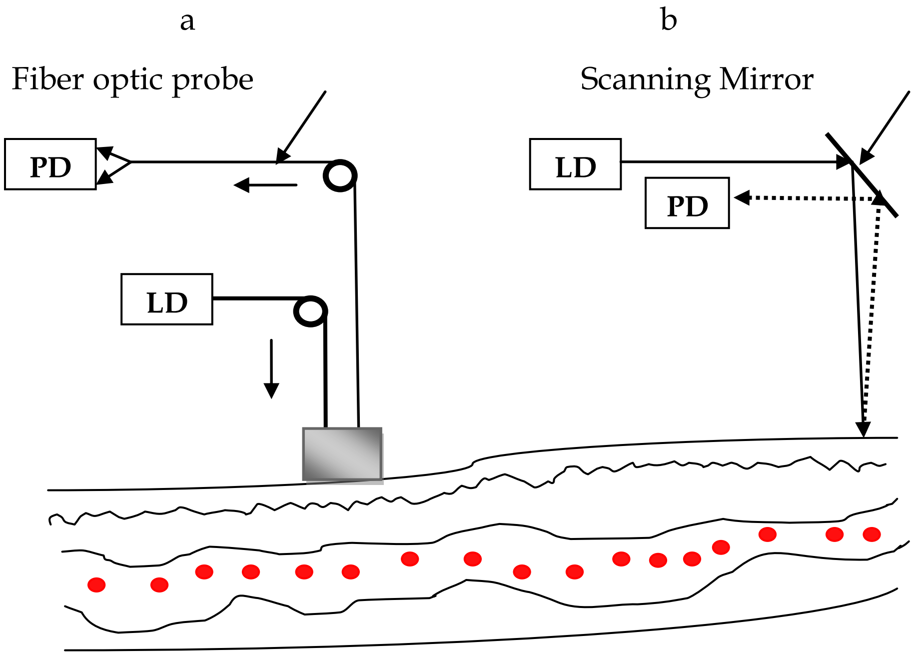

Figure 2.1 (a) LDPM and (b) LDPI on tissue model. LD laser diode, PD Photodetector

2.1 Light source

A laser source produces an intense beam of light with single wavelength. The light generated by laser source is a monochromatic, directional, and coherent in nature. The backscattered light forms an interference pattern on the avalanche photodetector and the fluctuations carry information about the Doppler shifts. The primary wavelengths used in laser include the ultraviolet, visible, and infrared spectrum and the maximum input power at the human eye was always kept below 1 mW to avoid any eye damage due to heating [14].

2.2 Doppler shift and Light interaction with ocular tissue

The basis of laser Doppler flowmetry is the optical Doppler effect described by the Austrian physicist Christian Doppler in an article entitled "*On the Colored of Double Stars and Some Other Heavenly Bodies*", which describes that the light scattered by a moving particle induces frequency shifts depending on the movement of the particle, the direction of the incoming light and the direction of the scattered light.

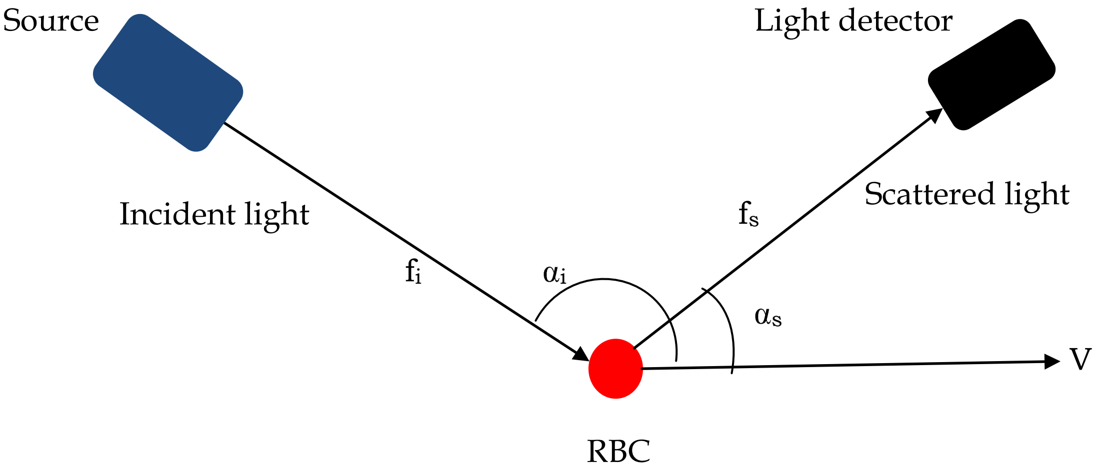

Figure. 2.2. Schematic diagram of the Doppler effect

Consider a red blood cell (RBC) moving at velocity V in the direction shown in Figure 2.2. A laser beam of single frequency f_i is impinging on this RBC at an angle α_i to the direction of V. The incident light is scattered by RBC in different directions. In the direction of the detector, defined by the angle α_s with V, the frequency of this light will differ from f_i by an amount equal to

$$\Delta f = f_{i-}f_s = n|v|(\cos\alpha_{s-}\cos\alpha_i)/\lambda \tag{2.1}$$

where Δf is the Doppler shift. The magnitude of frequency shift depends upon V, α_s and α_i, the index of refraction n of the medium containing the particle and the wavelength, λ, of the laser light in vacuum [15]. According to equation 2.1, the larger scattering angles will produce a larger frequency shift, with the largest frequency shift is possible when the impinging light is scattered back on the same direction of impinging ($\alpha_i = \pi$ rad). Biological tissue is a transparent medium allows multiple scattering of lights. When the tissue is not moving, red blood cells flowing in that tissue induce some considerable amount of frequency shifts. The light scatters by the moving red blood cells in the direction of the incoming light f_i induces larger scattering and regarded as random compared to the direction of the blood flow.

Laser Doppler measurements are insensitive to the direction of blood flow due to the movement of the red blood cells in capillary and vessels. When the scattering angle α_s is very small, the frequency of the scattered light f_s, is independent from the frequency incoming light f_i for red blood cells. The scattering angle with equal probability produces same frequency shift. The total frequency shift is large, if the light scattered multiple times by moving red blood cells. According to the equation 2.1, when the red blood cells moving orthogonal to the incoming light, the frequency shift is very large even though scattering angle ($\alpha_s \approx 0$ rad) is small. The Doppler shifts usually very large due to the movement of RBCs parallel to the light propagation and smallest for movement orthogonal to the light propagation.

2.3 Principles of light scattering and absorption

Electromagnetic theory and Quantum theory is very much needed to understand the complex nature of propagation the light. Light propagation through a medium dependent upon the refractive index of medium as described by Ray optics, Snell's and Fresnel's laws. Ray optics is most inadequate in describing the propagation of light in biomedical applications. When the light interacts with a particle two process can occur: it can be either scattered or absorbed.

Scattering

Scattering is a physical process of light deviate from the original path when they pass through a medium [16]. The deviation of the incoming light with an angle is predicted as reflection. The light hit by a particle is scattered in many directions and some time reflected back on the direction of the incoming light. In a homogeneous medium, the particles are arranged in an ordered pattern giving a constant refractive index, so the waves are re-radiated in all directions and the light beam propagating in the forward direction only. [17]

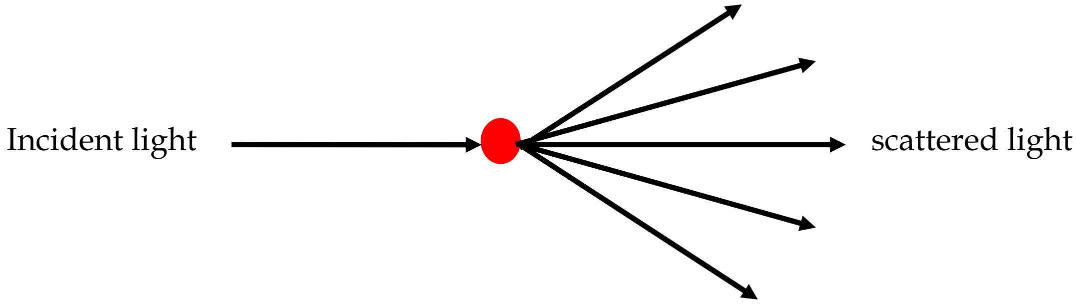

Figure 2.3 Scattering of incident light by a particle

The change in ordered pattern of the particle induces a change in refractive index. The inhomogeneous refractive index causes the light to propagate in all directions than in the forward direction. The scattering angle depends upon the size and shape of the objects. When the size of the object is larger than the wavelength a fraction of the light is reflected at the boundary and the remaining light refracted. The angle of refraction is given by Snell's law

$$n_1\sin\theta_1=n_2\sin\theta_2 \tag{2.2}$$

where n1 and n2 are the refractive indexes of the object and surrounding medium and θ_1 and θ_2 are angle of incidence and transmittance respectively. The specular reflectance is obtained, when a fraction of un-polarized light is reflected. The amount of specular reflectance is calculated using Fresnel's law

$$r = \frac{1}{2}\left(\frac{\sin^2(\theta_1-\theta_2)}{\sin^2(\theta_1+\theta_2)} + \frac{\tan^2(\theta_1-\theta_2)}{\tan^2(\theta_1+\theta_2)}\right) \tag{2.3}$$

The efficiency of the scattering by a particle (ρ_s) is depending upon the scattering cross section (σ_s) and the scattering coefficient of the medium (μ_s). The distribution of the scattering angles was described by scattering phase function. The mean cosine of the scattering angle is anisotropy factor which describes the level of forward scattering. The anisotropy factor (g) is proportional to the absorption coefficient. The red blood cell (RBC) is an example of a particle with a very high anisotropy factor.

Absorption

The energy of the light is transferred during the absorption process. The quantum theory denotes the energy absorption by a molecule leads to change in energy level from lower level to higher level [18]. The complex structure of biological molecules induces infinite amount of transitions. The absorption spectra of the biological tissues are smooth and continuous. The efficiency of an absorbing particle at a certain wavelength is denoted as absorption cross section (σ_a) and is given by the geometrical cross section of the particle, weighted with an absorption efficiency factor. The absorption coefficient is given by

$$\mu_a = \rho_a \, \sigma_a \tag{2.4}$$

where ρ_a is the number density of absorbers in a medium. The mean path length of the light propagating through the media before absorbed by a particle is given by Beer-Lambert's law [16]. This law gives a logarithmic dependence between the transmission of light (T) through a substance and the product of the absorption coefficient of the substance (α) and the distance the light travels through the material (*l*).

$$T = \frac{I_l}{I_0} = e^{-l\sigma N} \tag{2.5}$$

where N is the no of density absorbers. The light intensity decays with the penetration distance *l* through an absorbing material, where I_0 is the intensity of the incident light.

2.4 Doppler shift power spectrum

The light impinging on the avalanche photodetector contains all lights includes, non-shifted light, single shifted, and multiple shifted. The interference of the coherent light gives small frequency differences within the light, caused by the Doppler shifts. This leads to amplitude variations in the detector current which can be analyzed by looking at the power spectral density of the signal, called the Doppler shift power spectrum (DSPS).

Let us consider a light back scattered by an RBC flowing through a vessels or optic nerve in human ocular tissue. The back scattered light contains sum of un-shifted light and Doppler shifted light. The un-shifted light retains the same frequency of the laser source. The optical path length and the angle of the shifted light vary with medium it scatters and longer optical path light having larger wavelength of the light. Most of the light emerging from the tissue is scattered by the static structural components of the tissue. This non-shifted light acts as a reference signal and that is mixed at the surface of the photodetector with the Doppler-shifted light scattered by the moving RBCs. The Doppler shifted signal contains both the positive and negative shifted light according to the direction of the movement of RBC [6]. The detector squares the sum of the shifted and non-shifted light at its surface; its output current contains only the positive oscillating components oscillating at the various Δfs, not the original f_i. A plot of the power of the photocurrent as a function of Δf constitutes the Doppler shift power spectrum (DSPS).

2.5 Practical considerations in LDF technique

Measurement Volume

Most LDF techniques involved in blood flow measurements provide only relative measurements due to the uncertainty in knowing the sampling volume. The most of the signals impinging on the optical fiber originating from the volume is close to the probing beam on the ocular tissue. Scattering and absorption properties of such tissue affect the measurement of volume.

Monte Carlo method is able to simulate complex structure of the vascular beds with different Doppler shifts to obtain the measurement volume. Various studies exploited for the measurement of volume using the Monte Carlo technique have previously reported that most of the reflected light comes from close to the detector and signal from the deeper vascular beds or vessels having higher velocity [19,20]. The measurement volume in biological tissues depends on the optical properties of the tissues.

Movement of artefacts

LDF measurement of blood flow is affected by the movement of artefacts associated with the perfusion signal. The movement of measuring tissue or fiber-optic probe may causes larger perfusion signal [21-22]. The movement of the fiber collecting the reflected light from the human eye contributes some uncertainty at the low frequency part of the Doppler shift power spectrum. The uncertainty at low frequencies is avoided to some extent using a small aperture fiber placing very close to the tissue [23]. The low frequency component below 30 Hz is filtered using a high-pass filter. The noise associated with optical fiber may be reduced using a same fiber for delivery and detection [24-26].

The total Doppler shift of the light reflected at the surface tissue having a same velocity component. In LDF instruments, the laser source and the detector is sufficiently separated from the tissue surface. The time-varying components of effective scattering vector for all reflected light are same. A large amount of light may be directly reflected in the tissue surface adding only to the movement artefact without gaining any frequency shifts from the blood perfusion. Tissue motion and the physical movements of the subjects produce more artefacts in a non-contact measurement technique such as laser Doppler perfusion imaging than with monitoring using the probe fixed on the skin [27]. Large motion of artefacts was introduced in LDPI method, because it takes few minutes to complete one scan of entire image under the detector. This motion of artefacts in LDPI method may be reduced by placing a polarized filter in front of the detector. The recently developed full-field technique is more efficient to reduce the influence of movement of artefacts compared with the scanning techniques.

2.6 Laser safety issues

Human eye is the most sensitive part of the body. The laser radiation focused on the eye's lens to a small spot on the retina cause serious permanent damage within fractions of a second – even when the power level is only of the order of a few milliwatts [28]. Damage can result from both thermal and photochemical effects.

All instruments uses laser as a light source must follow specific laser safety standards. The laser safety rules may vary from country to country and depends upon the legal regulation enforced in that country. However, the rules are framed based on some international standards like IEC (International Electrotechnical Commission), ISO (International Organization for Standardization), or other national societies such as ANSI (American National Standardization Institute). Most of the world, the applicable laser safety standard is the international standard set by the International Electrotechnical Commission (IEC), and known as IEC 60825 [29].

Different parts of the eye can be damaged by the laser light depending upon the wavelength and power. Most of the impinging optical power is usually absorbed by melamine pigments in the pigment epithelium [30].

Table 2.1 Wavelength regions of optical radiations and pathological effects defined by international commission of illumination [31]

Region	Wavelength	Pathological effect
UVC	100-280 nm	Photokeratitis
UVB	280-315 nm	Photochemical cataract
UVA	315- 400 nm	Pigment darkening , Photo sensitivity
Light *	400- 780 nm	Retinal burn, Photochemical retinal injury, Skin burn
IRA	780 – 1400 nm	Retinal burn, Thermal cataract
IRB	1.4 – 3.0 µm	Corneal burn
IRC	3.0 µm – 1mm	Corneal burn, Skin burn

* The limits for the human eye vary among individuals over the ranges indicated

ISO 15004-2 specifies fundamental requirements for optical radiation safety for ophthalmic instruments and is applicable to all ophthalmic instruments that direct optical radiation into or at the eye. It is also applicable to all new and emerging ophthalmic instruments that direct optical radiation into or at the eye [32].

Maximum permissible exposure (MPE) is the level of laser radiation to which a person may be exposed without hazardous effects or biological changes in the eye. MPE levels are determined as a function of laser wavelength, exposure time and pulse repetition. The MPE is usually expressed either in terms of radiant exposure in J/cm^2 or as irradiance in W/cm^2 for a given wavelength and exposure duration. The ANSI standard defines MPE levels for specific laser wavelengths and exposure durations. The ANSI Z136 series is recognized by OSHA (Occupational Safety and Health Administration), and is the authoritative series of laser safety documents in the United States [33].

2.7 Recent LDF improvements

The Doppler effect induced by the blood cells to measure the blood flow was described by Stern [34]; LDF is approved recently as clinically applicable tool to estimate ocular perfusion after passing through several steps of improvements and developments. The major steps in the developments are reported by Watkins and Holloway [35], and followed by Stern [34]. Bonner and Nossal [3] developed a theoretical model of signal processor for estimation of blood flow. The technical modification of LDF instrument and development of signal processor based on Bonner and Nossal method was reported in [36-38]. The most improvements made in the field of LDF were related to hardware enhancement including the development of LDPI. Many improvements were contributed in the field of signal processing and signal analysis techniques over the years. A detailed review of recent methodological developments in LDF can be found in [39].

LDF research involves spectral analysis of perfusion signal using a spectrum or wavelets. The average RBC velocity was estimated using logarithmic slope of Doppler shift power spectrum of the reflected light [40]. The major limitations are the depth of the measurement is influenced with optical properties of ocular tissues.

Related techniques

Before the development of LDF, the xenon washout technique [41] and the radioactively labelled microsphere technique [42, 43], are the main alternative methods to measure the microvascular blood flow. The injection of radioactive substance into the blood greatly limits their usefulness in clinical diagnoses of ocular diseases.

Ultrasound Doppler techniques are widely used to measure the unidirectional blood flow in larger vessels. The thermography can be used as estimator, when the blood flow is related to the temperature of the tissue [44-46]. The major disadvantage of this method is the blood flow and temperatures are not directly connected. The information about the blood flow in human eyes is estimated with number of non-invasive optical techniques. The most direct method is capillary microscopy technique for the study of microcirculation in several diseases, especially disorders of connective system. The blood velocity can be estimated by inspecting the spatial dislocation of the RBCs frame by frame [47]. This technique is unable to measure the blood flow velocity due to the difficulty in identifying the number of active capillary vessels in that area.

The blood volume and oxygen saturation was estimated with other optical methods like photoplethysmography (PPG), pulse oximetry, and diffuse reflection spectroscopy. However, these methods do not provide any information about blood flow. Diffusing wave spectroscopy (DWS) is an optical method based on strong multiple scattering [48]. The DWS method results in larger measurement volume due to the larger separation of source and detector and the output are depends on high flow blood vessels. LDF is currently used in various fields including neuro surgery, cancer treatment and wound healing.

Ocular fundus reflectometry

The study of hemodynamics of the posterior segment of the eye can solve many problems in ocular diagnoses. Mainly the retinal circulations are investigated more, because it contains large amount of information. Photographic methods give fairly accurate estimate of the diameter of the larger retinal vessels and veins. The blood circulation time in the retinal vessels may be changed due to the raised intraocular pressure.

The study of choroidal blood flow is more difficult in fluorescein angiography, because the choroidal tissues contain dense of pigments. Many researches oriented towards study of behaviour of choroidal vessels using microscope was disturb the pathological conditions of the eye. Radio isotopes are used to estimate the choroidal blood flow and volume through continuous measurement process.

2.8 Functional imaging methods

Functional imaging is an interdisciplinary activity that allows scientists, engineers and physicians to simultaneously quantify the structural and functional aspects of a biological system. Functional imaging is a method used to detect the changes in blood flow. However, in the medical field images from the various part of the human body can be used for clinical purposes. Modern functional imaging methods are experimental tool to evaluate significant physiological changes occurred in the tissues through non-invasive technique.

The study of human brain function based on analysis of data acquired using brain imaging methods such as Electroencephalography (EEG), Magneto-encephalography (MEG), functional Magnetic Resonance Imaging (fMRI), Position Emission Tomography (PET) or Optical Imaging.

Functional magnetic resonance imaging (fMRI) and visual field mapping methods are used in clinical environment to diagnose and predict visual field defects. fMRI can be used to map the topography and function of visual cortex in and near a potential site of surgery. A visual defect simulator can provide the predicted regions of blindness in the visual field. Electroencephalogram (EEG) which records electrical voltages from electrodes placed on the scalp and the Magneto-encephalogram (MEG) which records the magnetic field from SQUID (superconducting quantum interference device) sensors placed above the head. Both MEG and EEG have a high temporal resolution and spatial resolution in the order of centimetres. However, functional Magnetic Resonance Imaging (fMRI) has low temporal but relatively high spatial resolution.

Fundus photographs

The observation of the fundus of the eye was used to diagnosis of ocular diseases with the help of ophthalmoscope. Fundus photographs can provide permanent record of these observations. Recent advancements in the field of electro-optics lead to number of new methods for functional imaging. CCD arrays replaced the photographic film in the conventional optical system to imaging the extended area of fundus. The images formed by focusing laser beam across the fundus while collecting the reflected light. This technique is used in confocal scanning laser ophthalmoscope (cSLO), cSLO tomography, polarimetry, and optical coherence tomography (OCT). Electronic detectors used in these instruments required proper calibration to measure the reflected light.

Modern fundus camera design grew from the work of Helmholtz, who introduced direct ophthalmoscope in 1851. The design was modified and improved by Thorner in 1899 and Gullstrand in 1910. Nordenson introduced a camera based on Gullstrand principles in 1925. The first commercial fundus camera was marketed by Ziess in 1926 based on Nordenson design. This camera had a 10 degree field of view and required one-half second exposure with color film. The color fundus photography was attempted in early 1929. The image quality in fundus photography limits their use in clinical practice. The other limitations of the fundus photography are the slow film speed and longer shutter speed under carbon arc illumination system. Hartinger replaced an electrical lamp for the illumination instead of carbon arc lamps.

Fundus reflectometry had been initiated by Brindley and Willmer [49] and in this method measuring of the bleaching of visual pigments which occurs when light falls on the retina. This principle has been extended by Buchanan et al [50], to study the changes in fundus pigment degenerations of the retina. After a certain modification in the apparatus with a resulting increase in sensitivity, it was possible to obtain a continuous record indicating bleaching in the fundus of the living human eye after exposure to light. The first attempt for fundus photographs were used to taken in monochromatic light before and after bleaching by Mizuno et al [51]. The practical difficulties of fundus photography needed a photo-flash. Flower et al. [52] used fundus photographs at 10nm intervals from 400 to 900nm to study reflectance at several retinal sites. The reflectance values for wavelengths below 550 nm were very high due to stray light. The digital cameras are more advantages compared to film-based cameras. Digital cameras are lower cost, easy to use, good resolution, and ability to modify the image quality through computer based image processing software's.

Video based systems

Video based imaging systems are developed to avoid the problems in analyzing fundus photographs. The application of a television system to produce an electronic image of the human ocular fundus was described by Ridley [53]. This system was produced some unsatisfactory results due to optical artefacts. Ridley was modified the design using a flying spot monochrome television (TV) ophthalmoscope. Potts and Brown developed the colour television ophthalmoscope in 1959 [54]. The main disadvantage of these systems requires very high level of fundus illumination. Improvements in TV technology over the years produced larger number of high efficiency low cost cameras. Ziess produced first commercial TV funduscopy by coupling the cameras with high efficiency ophthalmoscope. This method allows high speed recording of the images, however it requires large amount of time for dark-room processing of films and subsequent need of projector screen. The fluorographic results are obtained using high-resolution TV funduscopy system at a faster rate [55]. Video-based fundus reflectometer offers greater flexibility in mapping the amount of visual photo-pigments and macular pigments. The major disadvantage of these imaging devices are having very low signal-to-noise ratio due to stray-light.

Scanning laser ophthalmoscopes

The development scanning laser ophthalmoscope for functional imaging of the retina effectively solved the stray-light problem [56, 57]. In SLO, a laser beam is moved in a raster pattern over the retina at video rate. This is achieved by using a combination of spinning and oscillating mirror. The reflected beam was collected by a photomultiplier. This beam moves in synchronise with laser beam, each pixel of the TV corresponds to a spot on the fundus. The laser’s high radiance allows using only a tiny central portion of the eye’s pupil for getting light in. The remaining part of the pupil is used to collect the reflected light.

Scanning laser ophthalmoscopy [58] is a retinal imaging technique that is based on the standard scanning laser microscope. The important difference is that in scanning laser ophthalmoscopy, the optics of the eye serve as the objective lens. Scanning laser ophthalmoscopes and microscopes are equipped with a confocal aperture, offers better performance compared to the conventional imaging instruments [59]. The confocal SLO generates high contrast images and can do optical slicing through weakly scattering media making it ideal for imaging the multilayered retina. SLO with larger field of view (40 × 23°) and a retinal detection area of 1.35° centred around the laser spot (0.06°) on the retina was built by Utrecht research group [60].

SLO were marketed for clinical purposes in late eighties and nineties [61]. These instruments were not suitable for quantitative determination of reflectance due to optical setup and lack of stability of the lasers and electronics. A commercial instrument was developed with linear detector amplifier, fast shutters for laser beams and trigger unit to study the distribution of photo-pigments [62]. The first generation SLOs operated at one or two wavelengths and at one fixed focal plane. More recently, SLOs uses multiple wavelengths and different confocal setups for indirect infrared imaging of human retina [63-65].

CCD devices

The CCD camera was introduced in 1997 as a recording device of images in spectroscopy [64]. The CCD devices use single flash slit-like spot to illuminate the fundus. The spot was imaged onto two-dimensional CCD chip and it records the local distribution of the ocular fundus spectra.

A digital camera captures video or still images digitally through electronic image sensor. The resolution of a digital camera is limited by the image sensor. However, the images are stored as discrete pixel by replacing the films in the commercial photography. The sensor is made up of millions of "buckets" that counts the number of photons strike the sensor. The brighter the image at any given point on the image sensor having larger pixel value.

2.9 Instruments used for fundus reflectometry

The eye is more sensitive part in human body. The cornea, lens and fluids in the eye are more transparent to the light at wavelengths between 400 - 700 nm. Fundus reflectometry allows in-vivo measurement of the tissues of ocular fundus. The first generation ophthalmoscope contains two parallel glass plates used to reflect the light into the investigating eye. The instrument used to measure the fundus reflectance must follow the certain design aspects like optical configuration in retinal and pupil plane, spectral range and retinal luminance of the measuring light. Principles and applications of fundus reflectometry, covering both the historical and modern developments can be found in [67]. Van Norren and van de Kraats built a single spot reflectometer for the assessment of the optical density of the visual pigments in a small area on the retina illuminated by 30 W halogen lamps [68]. In this instrument, the light entrance and exit from pupil was separated by 0.25 mm with half circular. The measuring beam wavelength can be changed using a 14 rotating filter wheel.

Delori and Pflibsen modified the single spot reflectometer with 3 ms flash of xenon arc lamp uses an annulus for the entrance beam and the beam exit from the pupil at the center of this annulus [69]. Delori improved spectrophotometer with a light source of 150 W xenon-arc lamps for measurement of spectral reflectance and the intrinsic fluorescence of the fundus [70]. The beam was attenuated with 2.5 neutral density filters and the illuminated field size was 3°. The spectral analysis of the fluorescent and reflected light was done with a multichannel analyzer.

Fundus camera with fundus spectrograph is allowed to measure the spectral reflectance of the retina and able to provide information about the spectral reflectance of blood vessels or small regions with retinal pathology [71]. This instrument uses a 40 × 1500 µm bar shaped pattern illuminated by a flash of a xenon-arc lamp. Gorrand and Delori built an instrument with 543 nm He-Ne laser and field of view of 5° to study the function of photoreceptor in normal eyes [72]. Delori and Elsner modified photoreceptor alignment reflectometers to measure orientation and directionality of photoreceptors using a 543 nm He-Ne laser and field of view of 2° and entrance beam at the pupil is about 28 µm in diameter. Most reflectometers have no reference beam to compensate for alterations with time in the spectral emissivity and radiant intensity of the light source and to minimise the effects of low frequency drift that usually limits the sensitivity of a single-beam apparatus [73].

2.10 Tissue reflectivity

Eye is an important organ in the human body. It acts as a photo receptor and capable of image formation. The eyeball contains three covering layers: the sclera, the choroid, and the retina. The cross section view of the eye was shown in Figure 2.4.

The sclera is a thin transparent layer of tissue covering the front of the eye. Its function is to protect the delicate working parts of the eye and direct light rays onto the retina. The choroid is the vascular layer of the eye with connective tissues and lying in between sclera and retina. The retina contains light-sensitive tissues and lying inner side of the eye. The optics of the eye create image of the visual field on the retina.

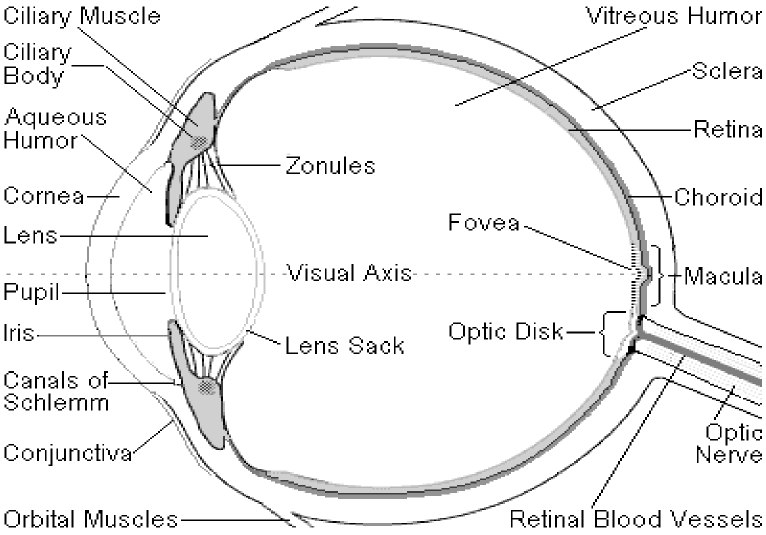

Figure 2.4 Cross section view of eye

The cornea is the transparent barrier between the eye and the environment, protecting the eye from pathogenic microbes and dryness. The cornea is comprised of three major cellular layers: an outermost stratified squamous epithelium, a stroma with corneal fibroblasts (keratocytes), and an innermost monolayer of specialized endothelial cells. The major eye disease like age-related macular degeneration (ARMD), glaucoma and diabetic retinopathy (DR) are leading causes of blindness occur due to failure in ocular tissues. The invention of laser initiates the diagnoses and treatment of eye diseases. There have been more studies in the past on ocular tissues [74].

The light interacted with ocular tissue may be absorbed or scattered depending upon the properties of the tissue. Many non-invasive methods used for the diagnoses of scattering and absorption characteristics of tissues [75]. The amount of light scattered by the tissue was depend upon the angle of light incident with the tissue. Fundus reflectance mainly depends on absorption of light by blood vessels in the fundus. The blood cells in vascularised choroid absorb more lights compared to other parts of eye. The ocular reflectance's are affected due to the incident and reflected light are pass over each other. The transmission through the ocular media is increase between 400 – 550 nm and reaches almost a constant value above 650 nm. The modern investigative ophthalmology and vision science uses human tissues for laboratory studies of physiology, anatomy, pathology. The studies on human tissues are most important to investigate the reason for diseases. There will be a continuing need to examine well-characterized human tissues in light. The interaction between light and ocular tissues plays an important role in diagnoses and treatments of ocular disease [75]. Eye research using human tissues is an important component in clinical ophthalmology for early detection of dieses.

CHAPTER 3

Effect of timolol on subfoveal choroidal blood flow

The measurement of blood flow in the ocular fundus is of scientific as well as clinical interest. The scientific value of blood flow measurements lies in knowing the physiology of deep vascular beds under local and central nervous control. Its clinical potential lies in the early assessment of alterations in blood flow associated with specific ocular diseases like glaucoma, age-related macular degeneration and diabetic retinopathy. The blood flow measurements should be accurate, reproducible and sensitive enough to detect the early pathologic alterations. The spatial resolution should permit blood flow measurement at discrete sites in human eye includes the retinal, optic nerve and choroidal vascular systems. The temporal response should be fast enough to investigate of blood flow responses induced by various physiological stimuli.

Laser Doppler flowmetry (LDF) is a non-invasive real time blood flow measurement technique which allows the measurement of the flux of moving red blood cells (RBCs) in the microvasculature of a tissue [38]. The application of LDF technique for measurement of blood flow in human fundus includes the optic nerve head [5] (ONH), the retinal microcirculation, [76] and the choroicappillaris in the foveal region of the choroid [4]. The measurement of the subfoveal choroidal blood flow (ChBF) may become important in the investigation of the pathogenesis of age-related macular degenerations. LDF has been applied invasively in cats and rabbits in the investigation of the effect of various physiological and pharmacologic conditions on ChBF [77, 78]. The studies performed on cats and rabbits use a fiber optic probe inserted into the eyes and placed near to the retinal surface. Studies performed in minipigs [79] and in cats [80] have demonstrated that LDF could also provide non-invasive measurements of ChBF. The laser Doppler flowmetry and blue field simulation techniques are truly non-invasive techniques to investigate ocular hemodynamics in humans.

The human eye is supplied by two separate vascular systems: the retinal blood vessels and the uveal blood vessels. The uveal vessels include the vascular beds of the iris, the ciliary body, and the choroid. The retinal vessels include the light-sensitive layers of cones and rods. The retinal metabolism entirely depends on the supply of nutrients and oxygen from the choroidal circulation. The choroidal blood flow (ChBF) is 10 to 15% higher than cortical blood flow. Alterations in human ocular blood flow are associated with many dominant eye diseases, including age-related macular degeneration [81–84], diabetic retinopathy [85] and glaucoma [86].

3.1 LDF instrument description

Laser Doppler flowmetry measurements of relative optic nerve head blood velocity (ONHVel), volume (ONHVol) and flow (ONHFlow), and foveal choroidal blood velocity (ChBVel), volume (ChBVol) and flow (ChBFlow) were obtained using the

Oculix instrument developed by Drs Charles E Riva and Benno L Petrig.

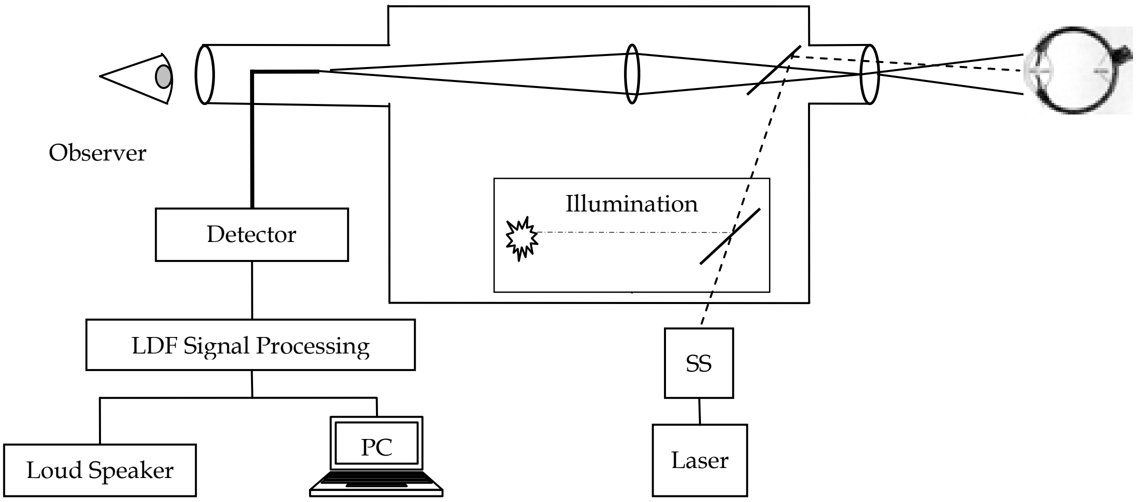

Figure 3.1 Schematic diagram of the fundus camera based laser Doppler flowmetry (LDF). The probing laser beam is delivered to the fundus through a steering system (SS) along the optical path of the fundus illumination.

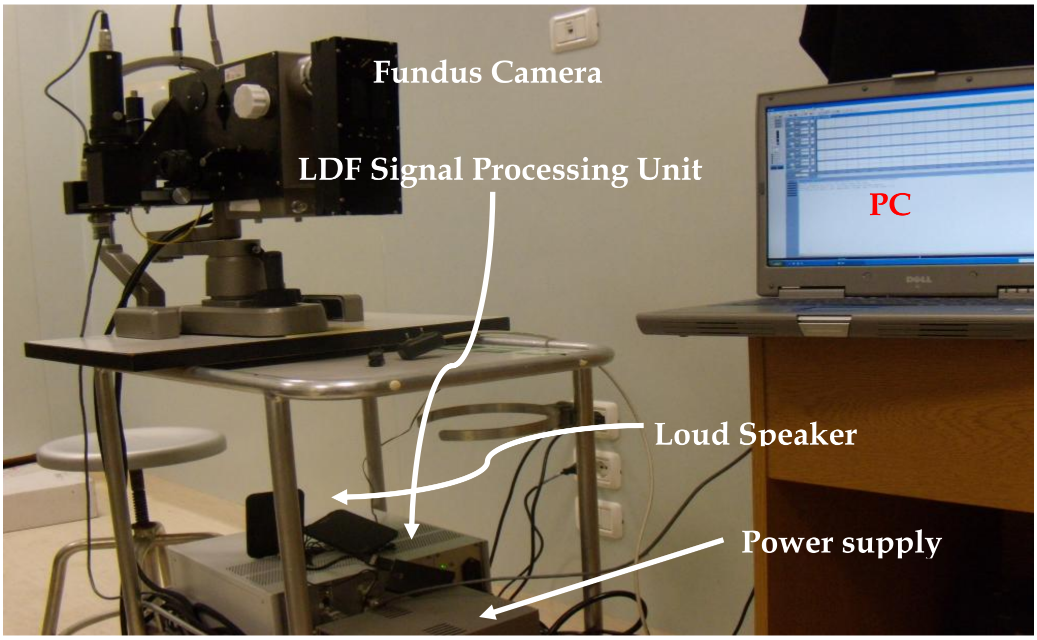

Figure 3.2 Experimental setup exploited for subfoveal choroidal blood flow measurements

The instrument is based on a modified fundus camera (Model TRC, Topcon-670, Tokyo, Japan). The optical systems for the delivery of the laser light and for the detection of the scattered light are based on the fundus camera arrangement shown in Figure 3.1. The complete experimental setup used for the subfoveal choroidal blood flow measurement was shown in Figure 3.2.

The fundus camera contains three important units namely: illumination system, laser steering system and the detector system. The human fundus was illuminated with a help of halogen continuous light source (Hosobuchi, 6V, 30W). The brightness of the light source was controlled by a power supply (Topcon, FD-30). The illumination produces a sharp green ring on the cornea and this can be achieved by moving the camera up and down and right and left. This green illumination was used to view the fundus and allowed the operator to place the probing laser beam on the retinal vessels and optic nerve head. The laser steering system contains a laser source and focusing lenses. The fundus camera was modified with a laser source of 670 nm, 40 µW. The laser light was delivered to the human eye through the same optical path of the fundus camera illumination. The optical power delivered by the laser diode was measured using PC-controlled optical power meter (SH-TO-USB, Ophir Optronics, Israel) equipped with an optical head (PD300-IR-SH, Ophir Optronics, Israel).

The laser source was controlled through Oculix LDF-4000 unit. This unit was used to provide the probing laser beam and to collect the reflected beam from human eye. The probing beam was directed to the human eye with rotating prism mounted along the optical path of the laser light. The rotating prism was composed of two prisms and that rotates in opposite direction and directs the laser beam into two points on the human eye. By rotating the prism in the proper direction, we can obtain convergence of two laser points and obtain a sharp pin point laser probing on the human fundus. The laser beam was focused on human eye about 150 µm in diameter.

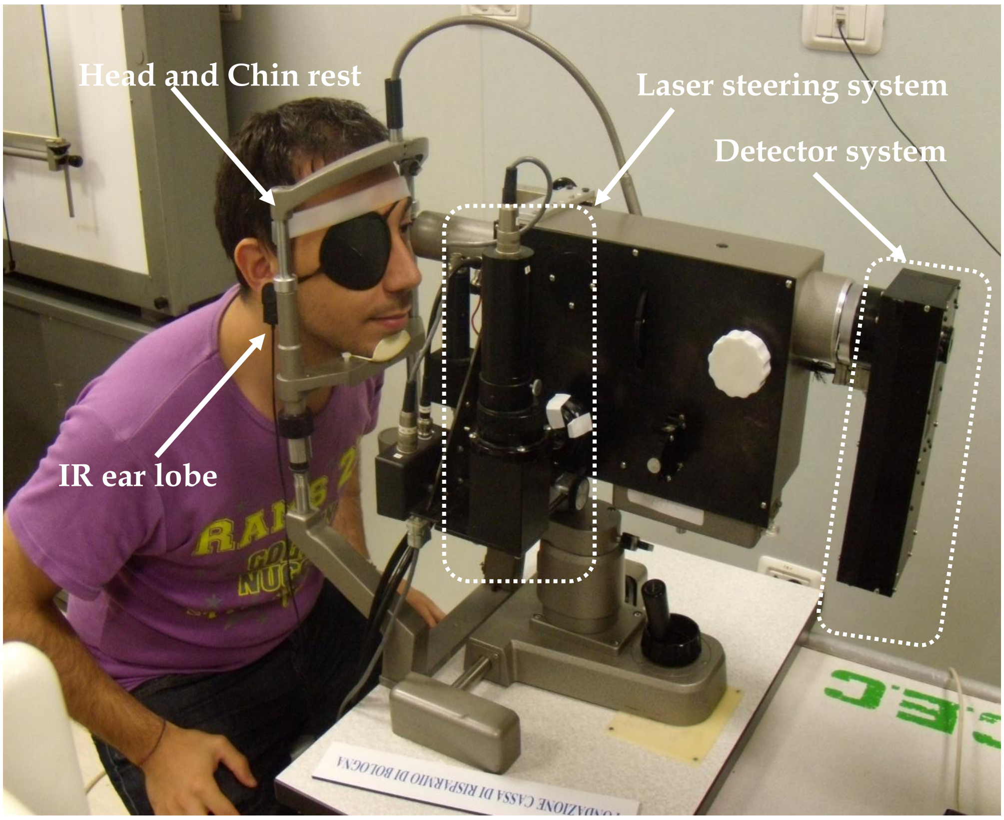

Figure 3.3 Picture of fundus camera based LDF system

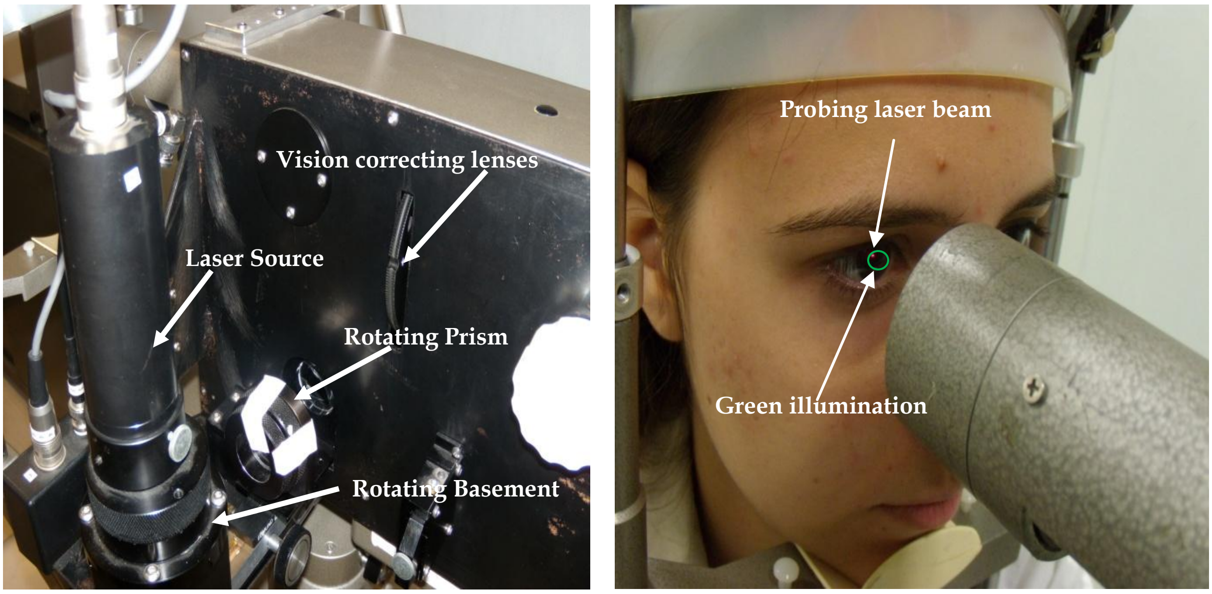

a b

Figure 3.4 (a) Laser steering system and (b) fundus illumination

The laser source was mounted on a rotating basement to rotate the focused beam around 360° in a circular path (Figure 3.4). This basement was used to adjust the probing beam entrance on the temporal side of human eye, between 7 to 11 o'clock for OD and between 2 to 5 o'clock for OS. The vision correcting lenses contains 4 lenses namely: normal vision, far vision, near vision and astigmatism. This rotatable vision correcting lenses should be adjusted according to the nature of the subject's eye vision.

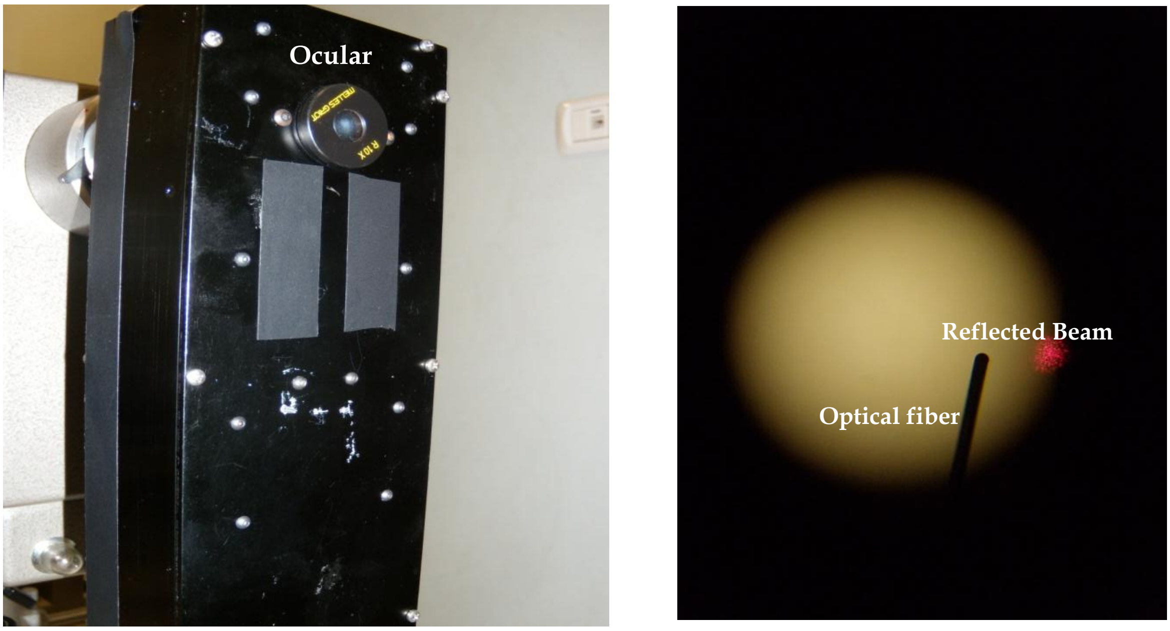

a b

Figure 3.5 (a) Detector system and (b) Illumination view seen through ocular

The detector contains an ocular, avalanche photodetector with optical fiber and the control buttons for moving the fiber (Figure 3.5). The ocular was used to view the fundus and allowed the operator to direct the impinging beam to the measurement site and allowed to place the optical fiber on the top of the reflected light to get a maximum Doppler sound. The maximum Doppler shift was identified with the audio sound of the Doppler signal heard through a loud speaker connected to the LDF signal processing unit. By moving the fiber using the control button and applying the joystick of the fundus camera to get a maximum sound as much as possible. The reflected light was collected by optical fiber with an aperture of 150 µm. The collected light was fed into an avalanche photodetector (R1463 Photomultiplier, Hamamatsu, New Jersey). The photocurrent at the output of photodetector contains the information about the Doppler shifts was amplified and analysed using LDF- 4000 (Oculix instruments, Pennsylvania, USA).

The LDF-4000 signal processing system (Figure 3.6) was consists of three units namely: DSP, Cam and Amp. The digital signal processing (DSP) unit was to process the LDF signal using software loaded on a personal computer (PC). This software was developed on Bonner and Nossal model using Doppler shifts power spectrum in real time and works with fast Fourier transform of the input detector signal.

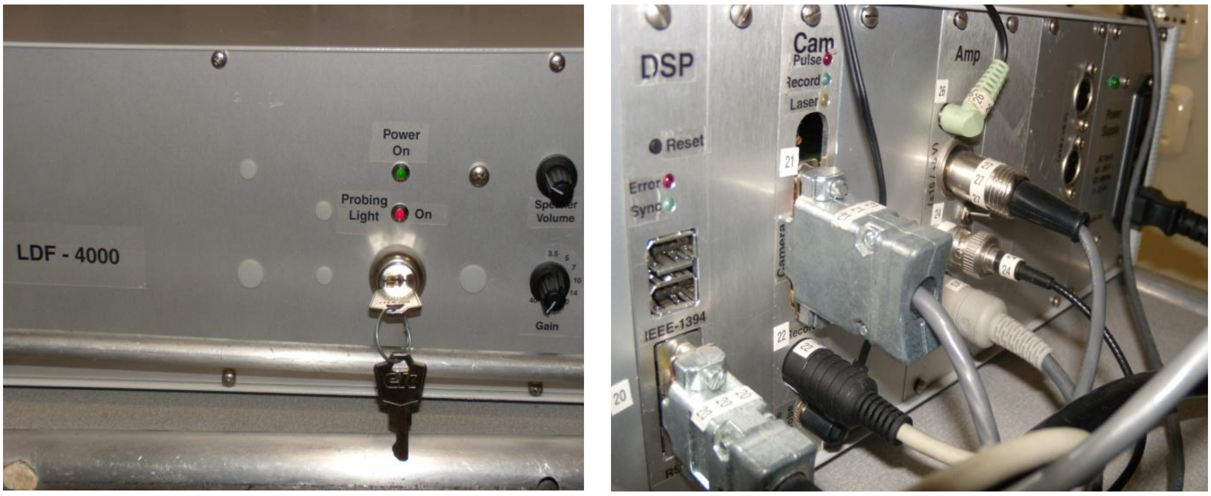

a b

Figure 3.6 (a) Front view and (b) Back view of signal processing unit

The unit was connected to the PC with an IEEE 1394 standard cable. The two signal indicators are present in this unit; Sync with green light, blinks continually means the data from DSP was sent to the PC synchronously and Error with red light glow means there was some error occurred with the transmission of data between DSP and PC. The reset button was used to reset the current processing of DSP. When pressing the reset button, all the LED's will lit for 0.5s and then green go off for 0.5s and then all other LED's go off for 0.5s and the green LED start to blinks again at 0.5 Hz.

The Cam unit contains three outputs with three indicators. The laser output provides necessary supply to the laser mount and the yellow colour indicator glows, when the probing laser was on. The probing laser can be switched ON using the key located in the front panel of the LDF signal processing unit.

Record output was connected to a pedal consists of two switches. One switch was used to initiate the recording and other was used to increase the intensity of the probing laser beam. During the measurement of blood flow, normally the laser switch is kept off. The recording switch can be ON/OFF several times to record the data. When the recording switch was off, the display of the trace will be in red color and during the on time it will be in blue. Once the recording was completed the red color traces are disappeared from the display and the blue color traces are turned into green and only the data corresponding to this trace will retained and stored into the file specified by the user. The green indicator will glow steadily during the recording process.

The third output of the Cam unit was connected to an Infrared earlobe. This can be attached to the ear or the fingers of the subjects to acquire the heart pulse. The data are processed by the software in phase with the heart pulse to display the systolic and diastolic effect of the pulse variation in flow parameters. The red indicator will blinks at the same rate of the heart pulse of the subjects.

The Amp unit consists of two signal inputs and two power outputs. The two power outputs with supply voltage of ±15V/+5V. This supply was directly connected to the camera and the detector. The two signal inputs are, one is from the avalanche photodetector and other is from the loud speaker. The Doppler signal captured by the optical fiber was fed into the signal processing unit and also fed into the loud speaker allowed to hear the pulsating pitch of the Doppler sound by both the operator and the subjects. The loud speaker allows the operator to place the laser probing beam and collection fiber in a place to get the maximum Doppler shifted signal. The amplifier having a square law device to squares the input signal components. The Doppler shifted signal contains sum of various frequency components including non-shifted components scattered by the static structural components of the ocular tissue. Some of the components are with positive shifts and the others are having negative shift depending on the movement of the red blood cells. The square law modulator squares the signal and the output contains only components with positive shifts and the signal was amplified and sends to the PC for processing with the help of software. The unit also contains two more standby power supply outputs with of supply voltage of ±15V/+5V.

The front panel of the signal processing unit consists of three controls. One control was used to switch ON/OFF the probing laser beam. The gain control knob was used to increase the gain of amplifier. The volume control knob was used to change the volume of the speaker sound.

The important parts of the LDF system was the personal computer (PC) loaded with LDF signal processing software. The LDF software was written in Java and designed to perform LDF data acquisition, analysis, and presentation and storage tasks. This unit contains a digital signal processor (DSP) that digitizes and analyzes one or more channels of Doppler signal and sends the results to the PC through an RS-232 communications interface over serial cable. The DSP serial port needs the specifications of 115200 baud, 8 data-bits, 1 stop-bit and no priority. When the LDF software was lunched, it resets the DSP and get ready to receive the data from the detector unit.

The LDF software panel display was shown in Figure 3.7. The LDF software was designed based on Bonner and Nossal model for blood flow measurement. This software was able to acquire data simultaneously from two channels. The Mode, Rate and Band used to set the LDF measurement type. The rate of acquition was always set to 25 Hz and the Band was set to 24 KHz for ChBF measurements and 6 KHz for optic nerve head measurements. The analog gain of the amplifier was changed with the help of the software and used to adapt the dynamic range of DSP to the signal levels provided by LDF-4000 detector system.

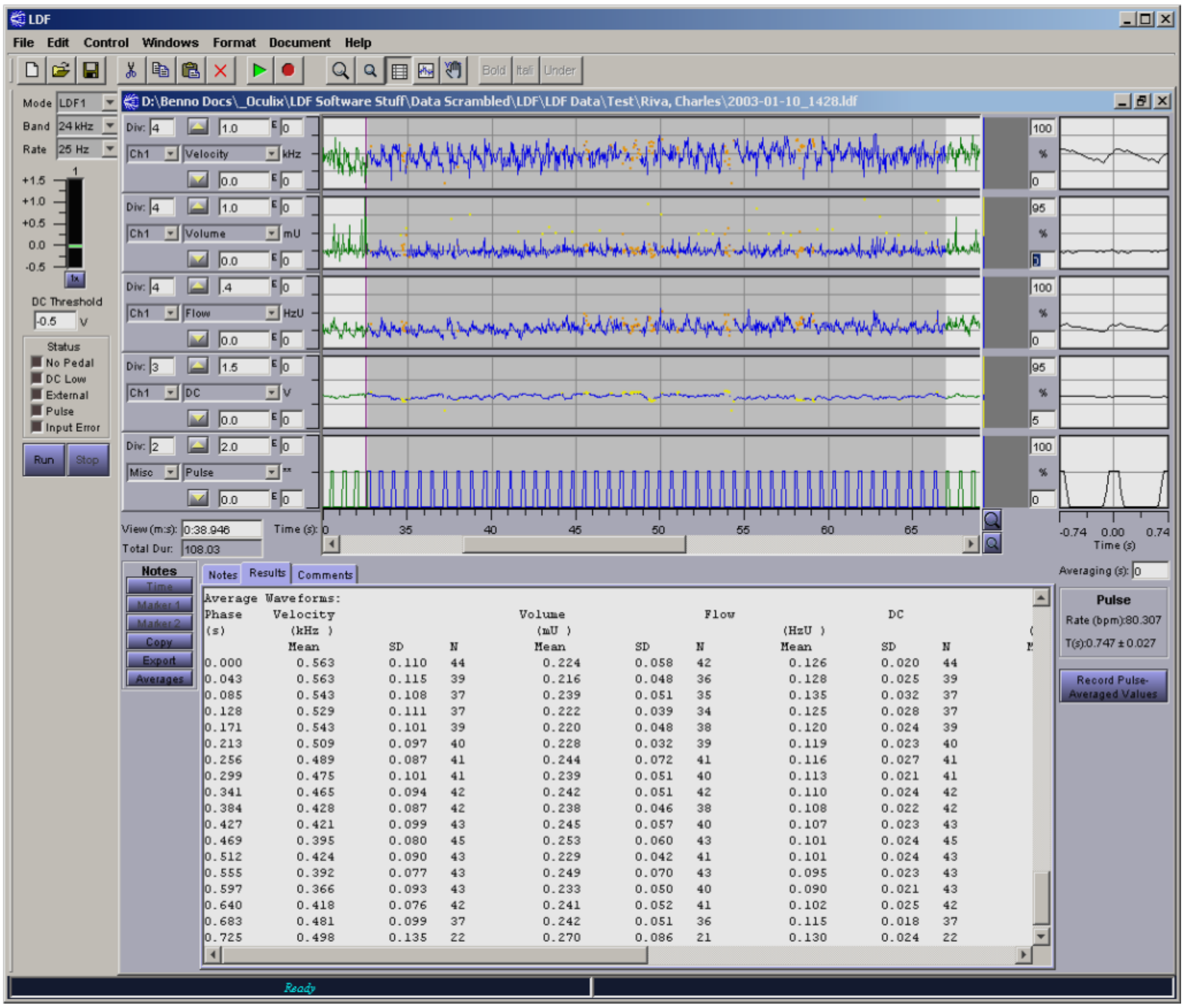

D:\Benno Docs_Oculix\LDF Software Stuff\Data Scrambled\LDF\LDF Data\Test\Riva, Charles\2003-01-10_1428.ldf

Mode: LDF1
Band: 24 kHz
Rate: 25 Hz
DC Threshold: -0.5 V
View (m:s): 0:38.946
Total Dur: 108.03
Averaging (s): 0
Pulse Rate (bpm):80.307
T(s):0.747 ± 0.027

```
Average Waveforms:
Phase    Velocity                              Volume                 Flow                                    DC
(s)        (kHz )                               (mU )                                     (HzU )
           Mean          SD       N            Mean          SD       N            Mean          SD       N
0.000      0.563         0.110    44           0.224         0.058    42           0.126         0.020    44
0.043      0.563         0.115    39           0.216         0.048    36           0.128         0.025    39
0.085      0.543         0.108    37           0.239         0.051    35           0.135         0.032    37
0.128      0.529         0.111    37           0.222         0.039    34           0.125         0.028    37
0.171      0.543         0.101    39           0.220         0.048    38           0.120         0.024    39
0.213      0.509         0.097    40           0.228         0.032    39           0.119         0.023    40
0.256      0.489         0.087    41           0.244         0.072    41           0.116         0.027    41
0.299      0.475         0.101    41           0.239         0.051    40           0.113         0.021    41
0.341      0.465         0.094    42           0.242         0.051    42           0.110         0.024    42
0.384      0.428         0.087    42           0.238         0.046    38           0.108         0.022    42
0.427      0.421         0.099    43           0.245         0.057    40           0.107         0.023    43
0.469      0.395         0.080    45           0.253         0.060    43           0.101         0.024    45
0.512      0.424         0.090    43           0.229         0.042    41           0.101         0.024    43
0.555      0.392         0.077    43           0.249         0.070    43           0.095         0.023    43
0.597      0.366         0.093    43           0.233         0.050    40           0.090         0.021    43
0.640      0.418         0.076    42           0.241         0.052    41           0.102         0.025    42
0.683      0.481         0.099    37           0.242         0.051    36           0.115         0.018    37
0.725      0.498         0.135    22           0.270         0.086    21           0.130         0.024    22
```

Figure 3.7 LDF software panel display

The display panel contains five data signals display namely: velocity, volume, flow, DC and the heart rate or pulse rate. The velocity, volume and flow are LDF parameters calculated using the Bonner and Nossal model. DC is the average voltage of the Doppler signal, which is proportional to the sum of shifted and non-shifted lights scattered by the moving red blood cells. The Misc parameter group allows selection of the Pulse or Pulse Delay. The pulse signal follows the heart pulse detected by the LDF-4000 system's pulse sensor. The pulse delay is a derived parameter and indicates the time elapsed (in seconds) since the rising edge of the pulse signal.

When LDF software was activated, it acquires the data continuously immediately after the Run button is pressed. The acquired data traced on the display panel in red color, when no pedal is pressed (Recording mode is off) and the trace in display panel is in blue color, when the pedal is pressed (Recording mode is on). When the stop button is pressed the blue color trace data points are turned into green color trace and the red color trace data's are disappeared from the display making gaps in the display and only the green trace data's are retained and used in future for the analysis.

The data's with high spikes are captured, when eye blinks or eye movement occurs and this data's are undesirable for analysis. This data portion can be hidden using hidden/visible button. When the pulse signal was recorded along with the LDF data, the pulse-phase averaging can be performed. This is the reason that LDF parameters can vary as a function of the cardiac cycle. All the data points having same delay after the raising edge of the pulse signal are averaged and plotted as a function of time delay. Using the pulse signal average method a histogram can be constructed, by setting the lower and higher percentile value from the selected area of the data, when the data falls within the range displayed in blue and the data falls outside the range displayed in yellow.

The data portions for analysis were selected using the shift + arrow. By pressing the result button on the window, it displays the result of the selected data over a cardiac cycle. The comment tab in the display window allows the user to write the comments regarding the measurement and act as a notepad. The record pulse averaging values button is pressed, it only displays the average values of the LDF parameters within the data range selected.

3.2 Effect of timolol on systemic parameters

Timolol Maleate is a non-selective, beta-adrenergic receptor antagonist similar to propranolol and nadolol. Timolol Maleate is used in the management of glaucoma, hypertension, angina pectoris, and myocardial infarction. Timolol is a β-adrenergic agonist used in clinical ophthalmic practice to reduce the intraocular pressure (IOP) in the treatment of glaucoma. The main mechanism of action of timolol is to decrease aqueous humor flow resulting in lowering IOP. Although the clinical effects of timolol on IOP are well established, little is known about the potential effects on ChBF. The purpose of this study is to describe the effect of timolol on the ChBF in the subfoveal region of human eye fundus.

The measurement of subfoveal choroidal blood flow is of great importance of knowing the normal visual function of human eye. Many researches on study of choroidal blood flow in the subjects with AMD showed the flow is much less compared to the normal eyes and that can cause severe visual impairment by disrupting normal macular function. The presence of abnormal choroidal blood flow induces ischemia and hypoxia, which triggers the development of angiogenesis and leads to the formation of choroidal neovascularisation (CNV).

A stable temperature in the macula region is maintained by a high blood flow in choroidal blood vessels. The choroidal vascular structure modulates the temperature in macula region through active and passive mechanisms. The active mechanisms involve a reflexive increase in choroidal blood flow in response to light [87]. The choroidal blood vessels lies between the outer retina and sclera, provides much information about retinal blood flow in humans and other mammals. The sympathetic vasoconstrictor and parasympathetic vasodilator nerves in choroidal region determines the level of choroidal perfusion [88]. The subject with diabetics, diminished ocular blood flow is the main cause of the progressive diabetic retinopathy. Abnormalities in blood flow contribute poor blood circulation and increased blood viscosity in diabetic human eyes [89].

3.2.1 Participants

Measurements were performed in 12 healthy volunteers (7 women and 5 men), ranging in age from 21 to 26 years with no history of systemic or intraocular disease was included in this study. Detailed explanations of all procedures were provided and informed consent was obtained from each subject prior to participation in the study. The protocol for the study was approved by the Medical Faculty Ethical Committee of the University of Bologna and conducted in accordance with the tenets of the Declaration of Helsinki. Subjects had no history of systemic or ocular disease, and results of their ocular examinations were normal. Intraocular pressure (IOP) at the beginning and end of the measurement was recorded using an Ocular Response Analyzer (Reichert Ophthalmic Instruments, USA) and was < 23 mmHg in all subjects. To perform accurate LDF measurements with fundus camera based system, adequate dilation of the patient's pupil is necessary. One drop of 1%Tropicamide was used to dilate the pupil of the subjects before instillation of the timolol or placebo in the eye in which the ChBF measurements were performed. The study protocol required abstinence from coffee, alcohol drinking and smoking, abstaining from a heavy meal, exercise, etc, all of which may affect the LDF measurements. None of the subjects was taking topical or systemic medication at the time of the study.

3.2.2 Specific parameters used in LDF measurements

The instrument used for the measurement of LDF was described in the previous section. For the measurements of ChBF, the LDF parameters of the Bonner and Nossal model [3] are derived from the Doppler shift power spectrum (DSPS) in real time using an algorithm operating on the PC [90]. This algorithm includes a fast Fourier transformation of the detector signal. The measured parameters are: (i) *Vel*: the mean speed of the RBC$_s$ in the sampling volume (proportional to the mean Doppler shift (Δf) derived from Doppler shift power spectrum) and (ii) *Vol*: the number of moving RBCs in sampled volume on the illuminating tissue by the laser beam proportional to the area under the DSPS curve. These LDF parameters are determined using the following equations:

The Doppler shift of the moving red blood cell is given by

$$\Delta f = f_{i-}f_s = n|v|(\cos\alpha_{s-}\cos\alpha_i)/\lambda \tag{3.1}$$

The velocity and volume of the red blood cell according to the Bonner and Nossal model with respect to the Doppler shift Δf is given by

$$Vel = \frac{\int_{30Hz}^{\Delta f_{high}} \Delta f p(\Delta f) d\Delta f}{\int_{30Hz}^{\Delta f_{high}} p(\Delta f) d\Delta f} \tag{3.2}$$

and $$Vol = \frac{1}{A_{dc}^2}\int_{30\,Hz}^{\Delta f_{high}} p(\Delta f) d\Delta f \tag{3.3}$$

where A_{dc} is the amplitude of the direct photocurrent (DC, non Doppler-shifted light). Doppler shifts below 30Hz are filtered out to avoid the low frequency artefacts due to slow motions of the tissue. Δf_{high} is set at 20 kHz for ChBF measurements. The RBC flux in the sampled volume is calculated as *ChBF*= k × *Vel* × *Vol*, where the *Vel* is expressed in Hz, and *Vol* and *ChBF* is expressed in arbitrary units. k is a proportionality constant or sometimes called as the instrument constant [15].

The LDF technique provides only the relative measurements due to laser radiation upon a tissue undergo scattering and absorption, both influencing the penetration pattern of the tissue. The penetration of the laser beam will differ from one region to another region depending on the optical properties of the tissue structure and composition.

3.2.3 Effect of timolol maleate on the artery blood pressure

The previous study reports that the topical timolol maleate 0.5 % produces an average increase in retinal blood flow in normal eyes [91]. The increase in blood flow is produced by the increase in perfusion pressure. The artery blood pressure (BP) was not measured and was estimated as

$$\frac{2}{3}\left(BP_{diast} + \frac{1}{3}\left[BP_{syst} - BP_{diast}\right]\right) - IOP \tag{3.4}$$

where BP_{syst} is systolic pressure and BP_{diast} is diastolic pressure and IOP is intraocular pressure. The factor 2/3 represents the drop in systemic mean arterial pressure between the brachial artery pressure and the ophthalmic artery. The mean perfusion pressure PP, was calculated according to the relationship

$$PP = 0.67\, BP_m - IOP \tag{3.5}$$

We performed this study to find the effect of topical timolol maleate on the diastolic, systolic and mean artery blood pressure. Measurements were performed in 24 normal healthy volunteers. After pupillary dilatation with one drop of 1% tropicamide, the intraocular pressure (IOP) was determined using ocular response analyser (Reichert Ophthalmic Instruments, USA). In sitting position, the heart rate and brachial systolic and diastolic blood pressures were measured by sphygmomanometry (Model: Contec 08A, China). In a double-masked randomized design, one eye of each subject received one drop of timolol maleate 0.5% ophthalmic solution, and the fellow eye received one drop of placebo. Two hours later, the experiment was repeated. Subjects were asked to refrain from eating or drinking during this time. Statistical evaluation of the data was performed using two-tailed paired student t-test and the findings with an error probability smaller than 0.05 were considered as statistically significant.

3.2.4 Results and Discussion

Measurements of brachial artery blood pressure, heart rate and IOP are shown in Table 3.1.

Table.3.1. Measurement of heart rate, mean brachial artery blood pressure (BP) and intraocular pressure (IOP) before and 120 min after application of the drop

Subjects	Heart rate		BP_m (mm Hg)			IOP (mm Hg)			
						Placebo		Timolol	
	Before	After	Before	After		Before	After	Before	After
1	82	72	103	100	100	21	19	22	18
2	88	70	102	100	100	14	12	15	13
3	60	56	95	100	100	15	13	16	14
4	88	78	90	91	91	17	19	16	13
5	80	72	90	92	92	19	18	17	18
6	90	74	93	87	87	15	13	17	13
7	70	58	90	90	90	14	11	15	12
8	90	78	93	92	92	18	15	18	14
9	92	79	92	88	88	18	17	14	15
10	68	74	88	90	90	17	15	16	13
11	88	72	102	98	98	15	14	16	13
12	84	86	97	93	93	15	15	15	12
13	78	62	90	90	90	21	20	23	20
14	80	68	93	93	93	14	13	14	11
15	52	62	98	95	95	17	16	17	14
16	76	78	92	87	87	13	14	15	17
17	66	58	87	90	90	18	14	17	14
18	80	62	87	88	88	16	13	17	12
19	72	60	92	87	87	13	11	15	13
20	76	58	102	100	100	19	15	18	15
21	90	72	88	82	82	19	16	21	16
22	70	72	93	93	93	15	17	17	13
23	78	82	100	103	103	16	17	15	12
24	82	66	100	95	95	15	14	17	13

Following the treatment, there was no significant change in diastolic (from 76.9 ± 6.2 mm Hg to 77.8 ± 6.1 mm Hg), systolic (from 128.3 ± 8.6 mm Hg to 122.4 ± 10.4 mm Hg) pressures. However, the average heart rate decreased significantly from 78.3 ± 10.3 to 69.5 ± 8.5 (paired t-test, p = <0.001) (Table 3.2).

Table.3.2 Average mean values and standard deviation of heart rate, artery blood pressure, IOP, and perfusion pressure before and 120 min after application of the drops

	Before	After 120 min	Significance *
Heart rate(bpm)	78.3 ± 10.3	69.5 ± 8.5	P<=0.001#
Artery blood pressure(mm Hg)	94.0 ± 5.2	92.7 ± 5.4	P>0.05
Intraocular pressure (mm Hg)			
Timolol	16.8 ± 2.3	14.1 ± 2.2	P<=0.001#
Placebo	16.4 ± 2.3	15.0 ± 2.5	P<=0.001#
Perfusion pressure (mm Hg)			
Timolol	46.2 ± 4.2	48.0 ± 4.5	P<=0.05#
Placebo	46.6± 4.3	47.1 ± 4.2	P>0.05

* Two tailed paired student-t test # statistically significant change

Intraocular pressure decreased significantly from an average of 16.8 ± 2.3 mm Hg to 14.1 ± 2.2 mm Hg (p<0.001) in the timolol-treated eyes, and from an average of 16.4 ± 2.3 mm Hg to 15.1 ± 2.5 mm Hg (p<0.001) in the placebo-treated eyes. The average decrease in IOP was significantly higher in the timolol-treated eyes than in the fellow eyes. No significant changes in blood pressure (p=0.06) was observed. The ocular perfusion pressure changes significantly in the timolol-treated eyes (from 46.2 ± 4.2 mm Hg to 48.1 ± 4.5 mm Hg, p=0.01) compared to the placebo-treated eyes (from 46.6 ± 4.3 mm Hg to 47.1 ± 4.2 mm Hg, p=0.39) were observed during the experiment.

The analysis of these results predicts that there may be some probability of an effect of the drug on the placebo-treated eyes causes a significant decrease in IOP observed in these eyes. Topical timolol instilled in one eye produce a decrease in IOP in the fellow eye. This phenomenon has been described previously [92-94] and is probably due to an influence of the drug reaching the fellow eye through systemic circulation. In addition, timolol lowers the heart rate and systemic blood pressure [95] thus affecting the circulation of both the timolol and placebo-treated eyes. The previous study on artery blood pressure using 2/3 of BP_m, estimated the average increase in perfusion pressure of 13% in the timolol-treated eyes and 7% in the placebo-treated eyes [91], using the formula BP_m- IOP, they estimated the average increase in perfusion pressure in timolol treated eyes 15 % and 1 % in the placebo-treated eyes [96].

The present study estimates that the average heart rate decreased by 11.2%, average artery blood pressure by 1.5%, the IOP in placebo-treated eyes by 8.3% and 16.1% in timolol-treated eyes. However, the ocular perfusion pressure estimated in the present study using 2/3 of BP_m shows an increase of 4% in timolol-treated eyes and an increase of 1% in placebo-treated eyes and using the formula BP_m- IOP, we estimated the average increase of 2% in the timolol-treated eyes and no changes in placebo-treated eyes. Our findings of a significant decrease in IOP both timolol-treated eyes and placebo-treated eyes predict that the placebo-treated eyes most probably affected by the timolol delivered in the fellow eye.

3.3 Effect of timolol maleate on choroidal blood flow (ChBF)

The influence of timolol maleate, a beta-adrenergic blocking agent on the choroidal blood flow was investigated using fundus camera based laser Doppler flowmetry technique. The previous studies reports a significant average increase in retinal blood flow on normal [91] and ocular hypertension subjects [97]. Two weeks of timolol maleate treatment on the retinal circulation of the normal volunteers was reported in [98]. Timolol is widely used to lowers the intraocular pressure in the management of glaucoma patients [99, 100]. The lowering in IOP has potential to cause vasoconstriction in retinal circulation and increase in vascular resistance with a less than optimal effect in blood flow [101]. Many researches are carried out on rabbit's retina about the influence of timolol on the choroidal circulation. The direct intervention of the blood vessels in human retina is more difficult [102].

3.3.1 Experimental Design

Design of the ChBF measurement was based on the double-masked randomized protocol proposed by Grunwald [97]. The systolic, diastolic, mean arterial blood pressures and IOP of the subjects were determined prior to the ChBF measurements. These measurements were repeated after 2 hrs. Two 50s duration measurements of LDF (*Velocity*, *Volume*, and *ChBF*) were performed on the both eyes of the subjects within 5 min. Both eyes of the subjects were fully dilated with one drop of 1% Tropicamide. The baseline measurements were performed 20 min after the application of the dilation drop. During the baseline measurement, a drop of timolol maleate 0.5% in one eye and a drop of placebo in the fellow eye were administered in a masked fashion according to the protocols of Grunwald, [95, 96] and Robinson [103]. Examiner was masked with regard to the eyes that had received timolol and placebo. Subfoveal ChBF in the choroicappillaris behind the fovea was measured for at-least 50s by LDF in both eyes at baseline. The LDF parameters were recorded 2 or 3 times on each eye with a rest period of 2 min between each recording. The same procedure was repeated every half hour during a 2-hour period following the instillation of the drop. The DC signal was kept as constant as possible between recordings and sessions for each eye. The measurements were repeated after a 2-week washout period by administering placebo in the eye previously treated with timolol and timolol in the eye previously treated with placebo. The data were analyzed statistically using paired student-t test (two-tailed) and the findings with an error probability smaller than 0.05 were considered to be statistically significant.

3.3.2 Results and Discussion

The mean and standard deviation values of Velocity, Volume and ChBF before and 2 hours after the instillation of the placebo and timolol drops are presented in Table 3.3. The percentage changes from the baseline values are summarized in Table 3.4.

Table.3.3 The mean and standard deviation values of Velocity, Volume, ChBF in 24 eyes during 120 min of measurement in timolol and placebo-treated eyes

	Baseline	After 30 min	After 60 min	After 90 min	After 120 min
Timolol-treated eyes					
Velocity (Hz)	1.437±0.19	1.521±0.18	1.603±0.22	1.657±0.30	1.676±0.32
Volume (a.u)	0.060±0.02	0.068±0.02	0.078±0.02	0.088±0.17	0.078±0.02
ChBF (a.u)	0.086±0.03	0.101±0.04	0.112±0.04	0.132±0.14	0.123±0.05
Placebo-treated eyes					
Velocity (Hz)	1.351±0.19	1.392±0.15	1.375±0.16	1.365±0.17	1.363±0.22
Volume (a.u)	0.060±0.02	0.070±0.03	0.080±0.03	0.084±0.03	0.081±0.03
ChBF (a.u)	0.085±0.04	0.097±0.03	0.104±0.04	0.113±0.04	0.115±0.04

Table.3.4 Percentage changes in Velocity, Volume and ChBF with respect to baseline values

	After 30 min	After 60 min	After 90 min	After 120 min
Timolol-treated eyes				
Velocity (Hz)	5.8%	12%	15%	16%
Volume (a.u)	13%	30%	47%	31%
ChBF (a.u)	17%	31%	54%	43%
Placebo-treated eyes				
Velocity (Hz)	3.1%	1.8%	1.1%	0.8%
Volume (a.u)	16 %	32%	39%	34%
ChBF (a.u)	13%	22%	33%	35%

Following the application of drops, the average percentage differences from baseline in velocity (p=0.081) is not statistically significant in placebo-treated eyes, however both the volume (p<=0.001) and ChBF (p<=0.001) shows statistical significant differences from the baseline values. The average percentage differences from baseline in velocity (p<=0.001), volume (p<=0.001), and ChBF (p<=0.001) are statistically significant in timolol treated-eyes. However the percentage changes in ChBF in the timolol-treated eyes are more compared to the placebo-treated eyes.

The results of this study show a significant average increase in ChBF following the instillation of timolol. This increase in ChBF was produced mainly by an average increase in velocity and volume of the red blood cells. The changes in intraocular pressure and ocular perfusion pressure also responsible for the changes in ChBF.

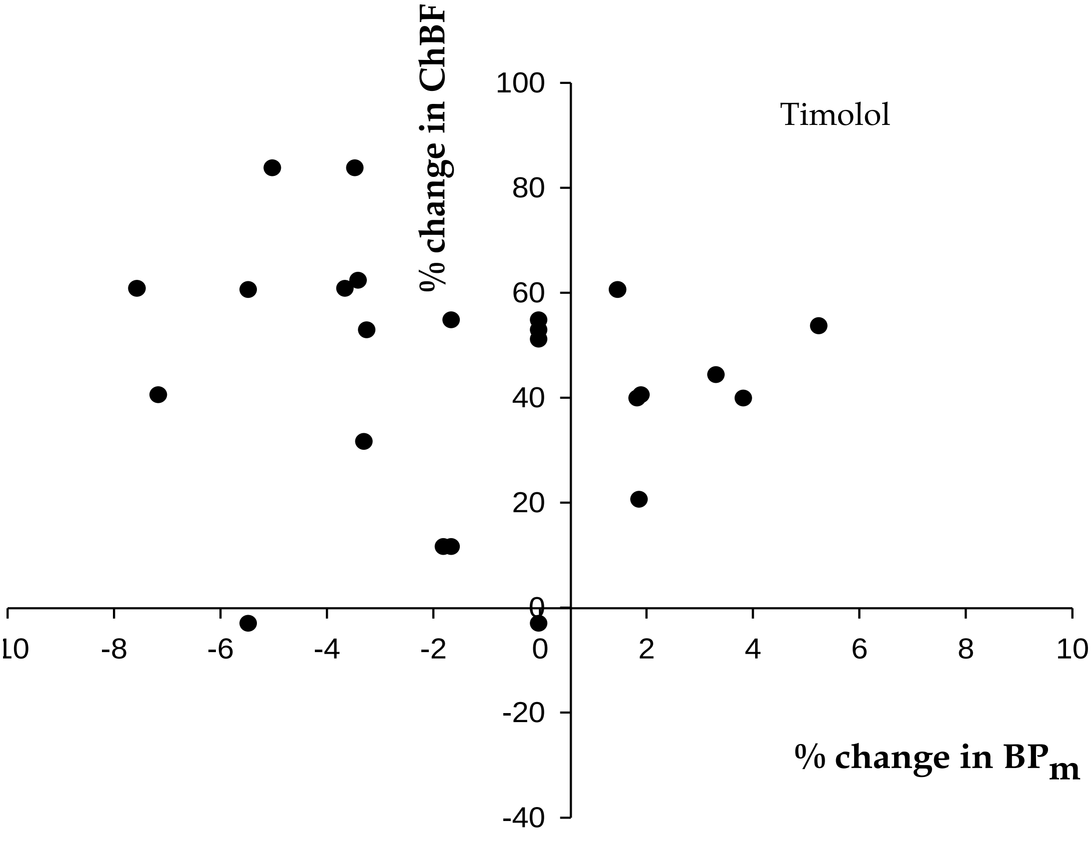

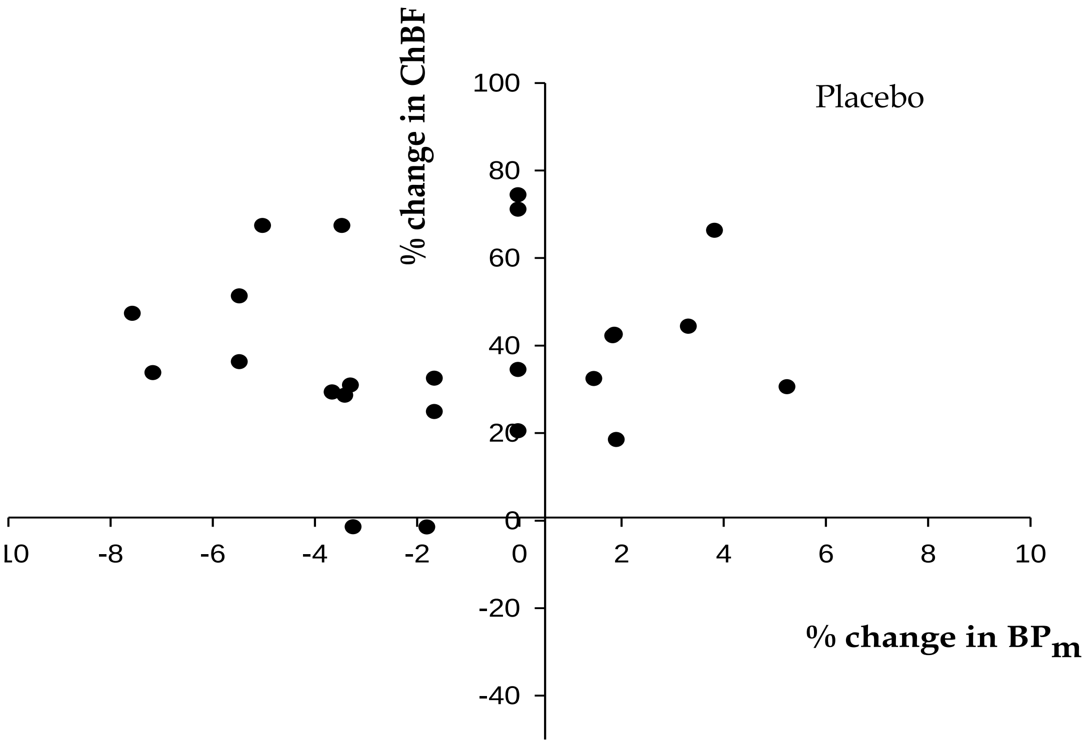

Figure 3.8 Percentage change in ChBF against percentage change in mean artery blood pressure in timolol and placebo-treated eyes

These results of this prospective study show that during the 120 min following their topical instillation, the LDF parameters are not statistically significantly different between timolol and placebo-treated eyes. However, a significant average increases in ChBF following the instillation of timolol or placebo was observed. No significant correlations were obtained between the changes in artery blood pressure and ChBF (Figure 3.8), between the percentage changes in ocular perfusion pressure and ChBF (Figure 3.9), and between the percentage changes in IOP and ChBF (Figure 3.10).

Previous studies [97, 98] showed much weaker effects of timolol on ocular hemodynamics. Therefore our experimental observation requires a deeper investigation, taking also into account that we observed a similar behaviour for the timolol and placebo-treated eyes. However, the placebo-treated eyes were most probably affected by the timolol delivered in the fellow eye. The concentrations of the drug reaching systemically the choroid of the fellow eye of the eye that received timolol [103] were probably much lower than those achieved in the instilled eye.

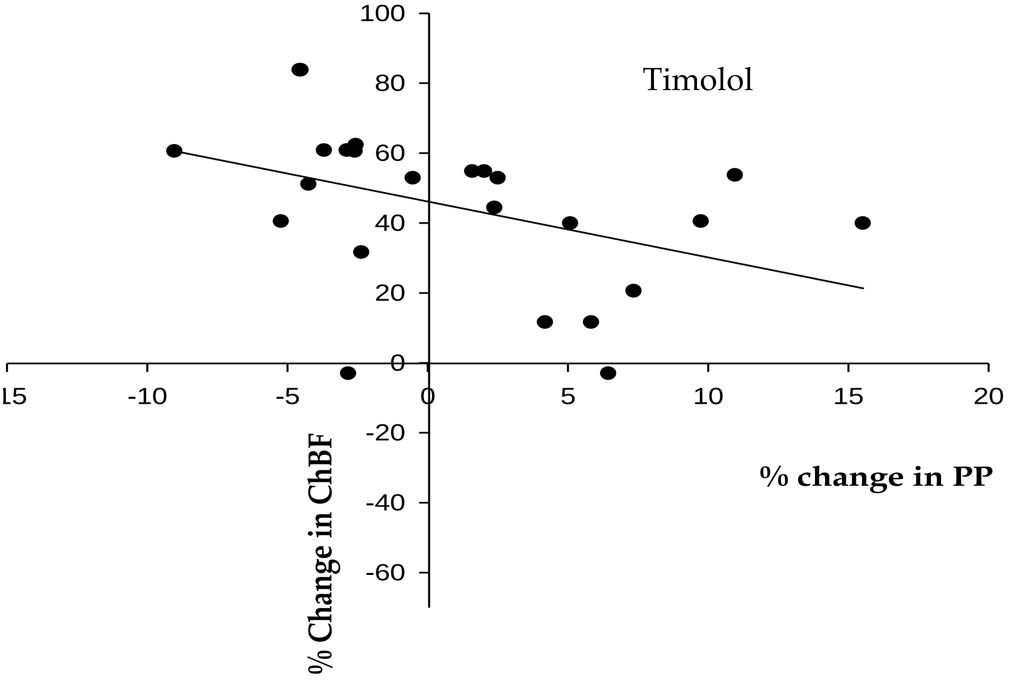

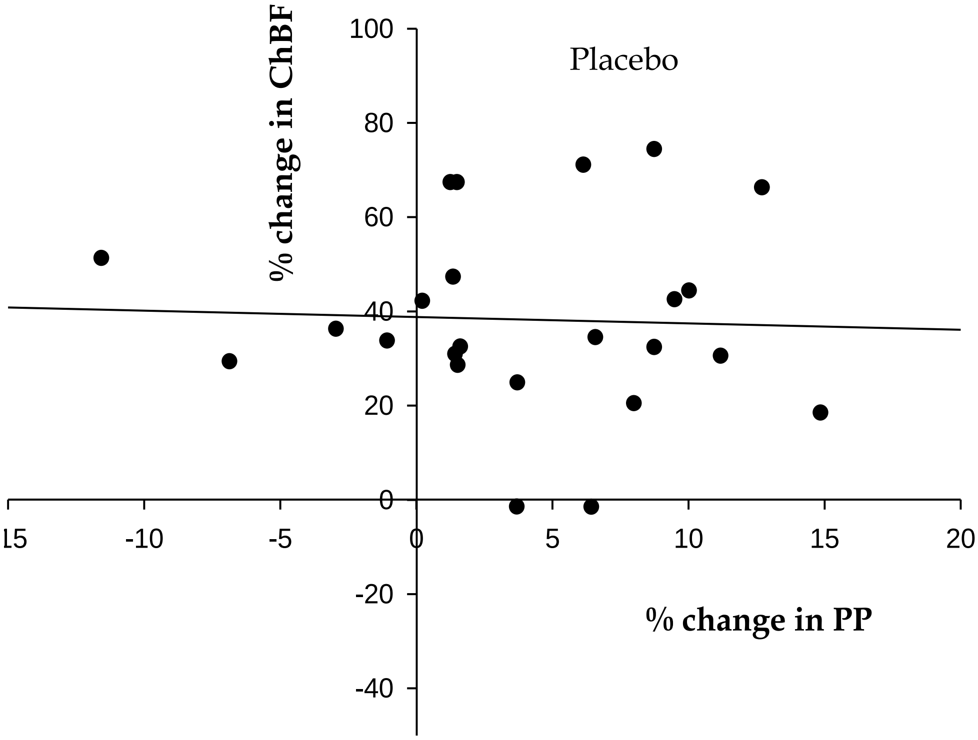

Figure 3.9 Percentage change in ChBF against percentage change in mean ocular perfusion pressure in timolol and placebo-treated eyes

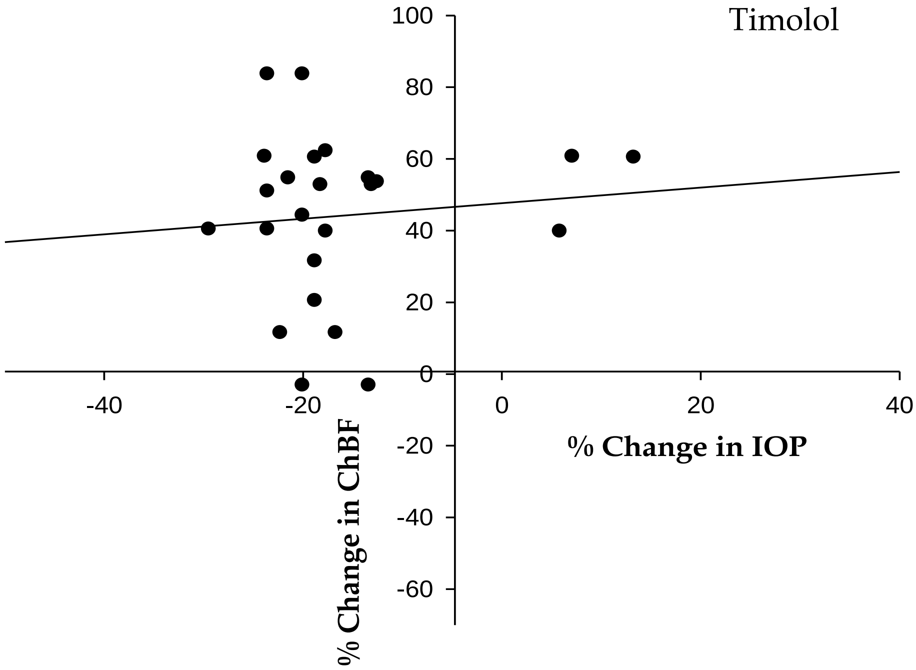

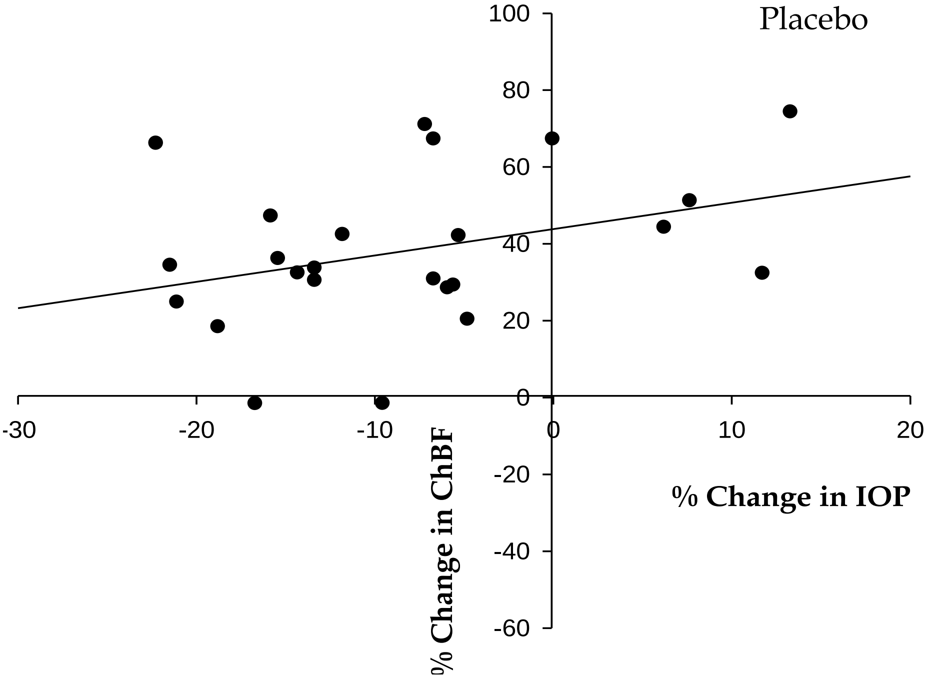

Figure 3.10 Percentage change in ChBF against percentage change in intraocular pressure in timolol and placebo-treated eyes

Our experimental results showed statistically significant decrease in IOP in both timolol-treated and placebo-treated eyes [104]. Due to systemic effect of the timolol drop given in the fellow eye, which may produces a change in ocular perfusion pressure [95] concurrently produces the changes in IOP and artery blood pressure. Our result confirms that the systemic effect of the drug, resulting in decrease in blood pressure or heart rate [95]. Another significant difference between the current study and that of Richard and Webber [105] is the timing of the measurements. Richard and Webber obtained the measurements IOP 30 min after the installation of the drug, whereas we obtained measurements IOP at 120 min after the application of the drop. The full effect of timolol on IOP and perfusion pressure may be reached at this time and also fellow eye also affected by the drug through systemic circulation. Although only a speculation at this time, we would like to present possible mechanisms that could explain our results. First, we would like to stress that, as the LDF measurements do not provide absolute blood flow measurements, because of uncertainty in knowing the sampling volume, this volume could itself be somewhat influenced by the drug. There is no significant correlation between the changes in flow with respect to change in IOP. The average change in blood flow is mainly contributed by the change in blood velocity and blood volume of the tissue and also depends on the Doppler shift power spectrum. However the spectrum is not only depend on the velocity of the red blood cells but also depends on the scattering properties of the tissue [106]. The optical properties of the tissue depend on the depth and penetration of the laser beam and cause some uncertainly in the sampling volume. The variability of the changes in the Doppler data may be due to the variability in the pupil diameter. Also apparent changes in ChBF due to pupil aperture variations are possible [107]. In conclusion, this study shows that, one drop of timolol 0.5% or one drop of placebo produce similar effects on ChBF.

CHAPTER 4

Effect of tropicamide on scattering geometry

The study of hemodynamics in ocular fundus is of scientific as well as clinical interest. The application of laser Doppler techniques for the investigation of blood flow in the posterior segment of the human eye provided much information on the physiology of ocular blood flow in the retinal, optic nerve and choroidal regions. The importance these measurements are used to gaining the physiology of deeper vascular beds under the control of local and central nervous system. The evaluation of the effect of treatment on the disturbed flows also represents an important area of application of laser Doppler flowmetry (LDF). LDF is a non-invasive technique, which allows the relative measurement of mean average velocity, volume and the flux of moving red blood cells (RBCs) in the blood vessels and capillaries of the human eye [108]. Laser radiation upon a tissue undergoes scattering and absorption. Both processes influence the penetration pattern of the laser light. Penetration may vary from one region of a tissue to another, depending on the optical properties of the ocular tissue [6]. The spatial or temporal variations in tissue structure will affect the LDF measurements. Direct comparisons of LDF values from different tissues are not valid, because of variations in optical properties of tissue structure and composition. The LDF parameters are expressed in relative units, the potential of LDF is realized mainly in the assessment of the responses of these parameters to changes in blood flow induced by physiological stimuli or by pathologies that do not alter the optical properties of the tissue. The property of the LDF parameters to provide changes of flow that are proportional to the real changes of tissue blood flow makes this technique particularly suitable for investigating the regulation of F_{onh} (optic nerve head blood flow) and F_{ch} (choroidal blood flow) in response to various physiological stimuli. However the changes in blood flow depends on the size of the pupil and the direction of the incident and scattering beams, and the scattering properties of the tissue. The small pupil having precise scattering geometry and leads to smaller Doppler shifts. In this study, we report effect of pupil dilatation with one drop of 1% tropicamide on LDF parameters and the scattering geometry of the ocular tissue in the choroidal region of human fundus.

4.1 Materials and Methods

Subjects

The measurements were performed in 18 healthy volunteers (6 males and 12 females) ranging in age from 20 to 25 years [mean 22.4 ± 1.6 standard deviation (SD)]. The study protocol was approved by the Ethics Committee of University of Bologna and followed the guidelines of the Declaration of Helsinki. Informed consent was obtained from all subjects after the nature of the study was explained. Each participant passed a screening examination including medical history and physical examination. The fundus examinations in all subjects were normal. In all subjects measurements were performed in one eye during pupil dilatation with one drop of 1% tropicamide. In 12 subjects, the measurements were performed with a 4 mm artificial pupil was placed directly 4mm (± 1 mm SD) in front of the eye (Figure 4.1). The study protocol required, abstinence from coffee, alcohol drinking and smoking during the day of examination.

Experimental design

LDF measurements were performed with the subjects seated in front of the camera before and after application of one drop of 1% tropicamide in one eye selected in random. All the LDF parameters were recorded in every 3 min upto 30 min after application of the drop and they last approximately 1 min duration. Video recording of the pupil size for 1 min was obtained using a digital video camera (Nikon Coolpix P300, Tokyo, Japan) for every 3 upto 30 min. The LDF parameters were recorded in two sets and in one set by placing a 4 mm artificial directly in front of eye and in the other set without any pupil.

The software for determining these LDF parameters allows rejection of the blinks or other spurious signals due to eye motion, which cause gaps in the continuous display of the data. Furthermore, LDF data corresponding to DC-values differing arbitrarily by more than 15% from the mean value were also excluded. Before every recording of a 30 min series, the LDF instrument was realigned with the subject's eye. Special attention was given to start the recording with a DC value close to that of the first recording of the series.

Methods

Sub-foveal choroidal blood flow was measured by LDF (Model 4000, Oculix). The detailed description of the instrument was presented in the previous chapter. The tissue was illuminated by coherent laser light (λ = 670 nm, 40 µW at the cornea). The laser power delivered by the instrument was measured using PC-controlled optical power meter (SH-TO-USB, Ophir Optronics, Israel) equipped with an optical head (PD300-IR-SH, Ophir Optronics, Israel). The laser intensity provided by the LDF instrument was kept constant below 40 µw throughout the measurement to compare the LDF parameters obtained over a period of time. The intensity of the room light was kept at normal condition (28 ± 2 lx) during the study and measured using a light meter (Delta Ohm HD9221, Italy). The variability in the assessment of LDF parameters limits their use in clinical practice. For choroidal blood flow (ChBF) measurement the subjects were asked to look directly at the probing beam. The diameter of the illuminated spot at the fundus is about 150 µm [6]. The scattered light is collected by an optical fibre with the image of its aperture focused onto the illuminated site (also approximately 150 µm in diameter). This fibre guides the scattered light to a photodetector. The fundus is illuminated in red-free light (30° angle) for observation and positioning of the laser beam. The moving red blood cells (RBC) induce some scattering leads to frequency shift. Most of the light emerging from the tissue can be scattered by the static structural components of the tissue is acts as a reference signal [109]. The light diffusion in ocular tissue leads to broadening of Doppler shift power spectrum (DSPS) of scattering light. From this spectrum, the average velocity and volume of the red blood cells (RBCs) within the scattering volume of the illuminated tissue is calculated in relative units. The product of velocity and volume is the flow and is proportional to flux of RBCs [5]. The picture of the measuring system was shown in Figure 4.1.

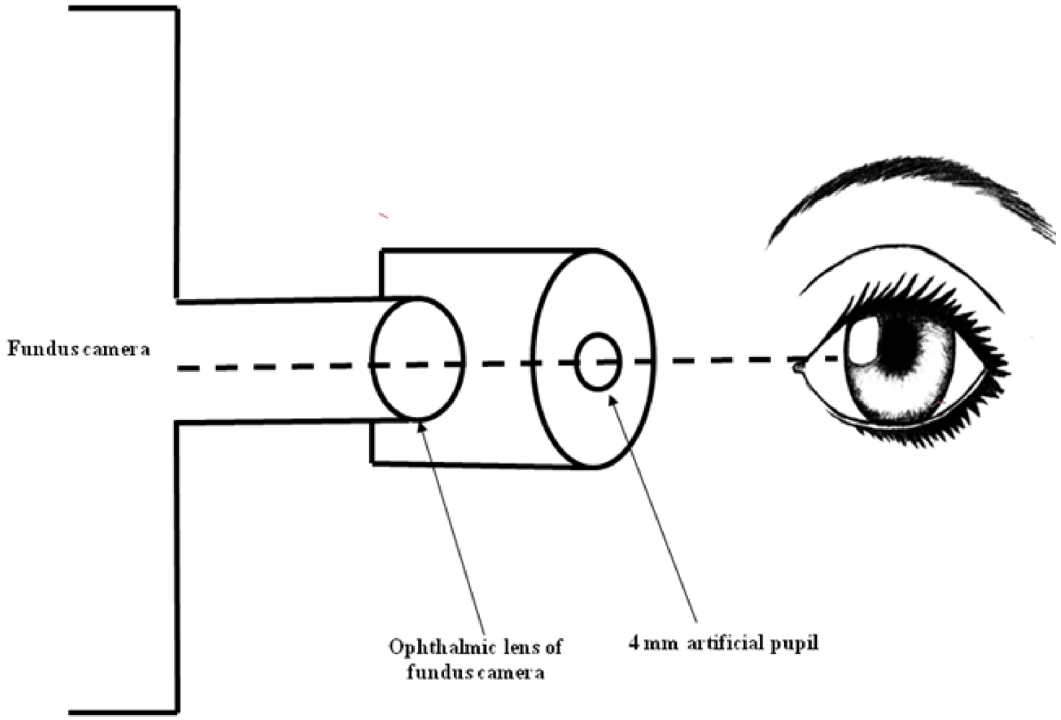

Figure 4.1 Picture of the experimental setup. (A) Picture of the measuring instrument (B) Optical scheme of modified fundus camera based laser Doppler flowmetry

Data analysis

Data are presented as mean ± standard deviation (SD). Treatment effects on LDF parameters were expressed as percentage change from baseline. The P-value was calculated from the two-tailed paired t-test analysis. P-value less than 0.05 were considered the level of significance. In addition, the coefficient of variation (CV) was calculated for each eleven consecutive measurements. Sample size calculations for clinical studies are obtained based on CV. These sample-size calculations are based on a double-sided α-error of 0.05 and a β-error of 0.20.

4.2 Experimental results

All the measurements were performed under resting conditions. Accordingly, the variability of measurements in the present study is more likely to arise from method related statistical errors. Care was taken to minimize this variability by using only individuals who had been included in studies with these techniques previously. The performances of clinical trials are experimented with a feasible number of study participants.

The pupil diameter was captured in every 3 min upto 30 min along with LDF measurements for duration of 1 min using a digital video camera. The video images are converted into still images using AVI to image converter software. The best still image among the sequence was superimposed on a ruler image before calculating of pupil diameter. The pupil diameter variation with time was estimated using a ruler with precision ± 0.5 mm (Figure 4.2). The mean pupil diameter of all subjects increases from 3.29 ± 0.44 (mean ± standard deviation (SD)) to 8.25 ± 0.44 ($p<0.001$, paired t-test; Figure. 4.3) after the application of one drop of 1% tropicamide. The percentage increase in pupil diameter is about 152% compared to the baseline value. The pupil dilatation was completed in all subjects, 20 min after the application of the one drop of 1% tropicamide.

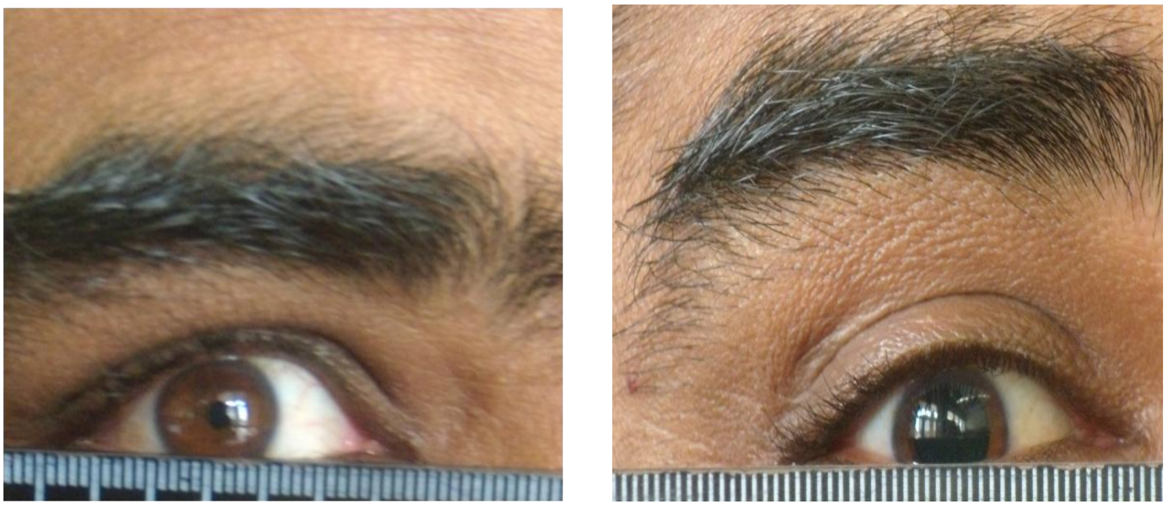
(a) (b)

Figure 4.2 Pupil diameter variations with tropicamide (a) un-dilated pupil and (b) fully dilated pupil

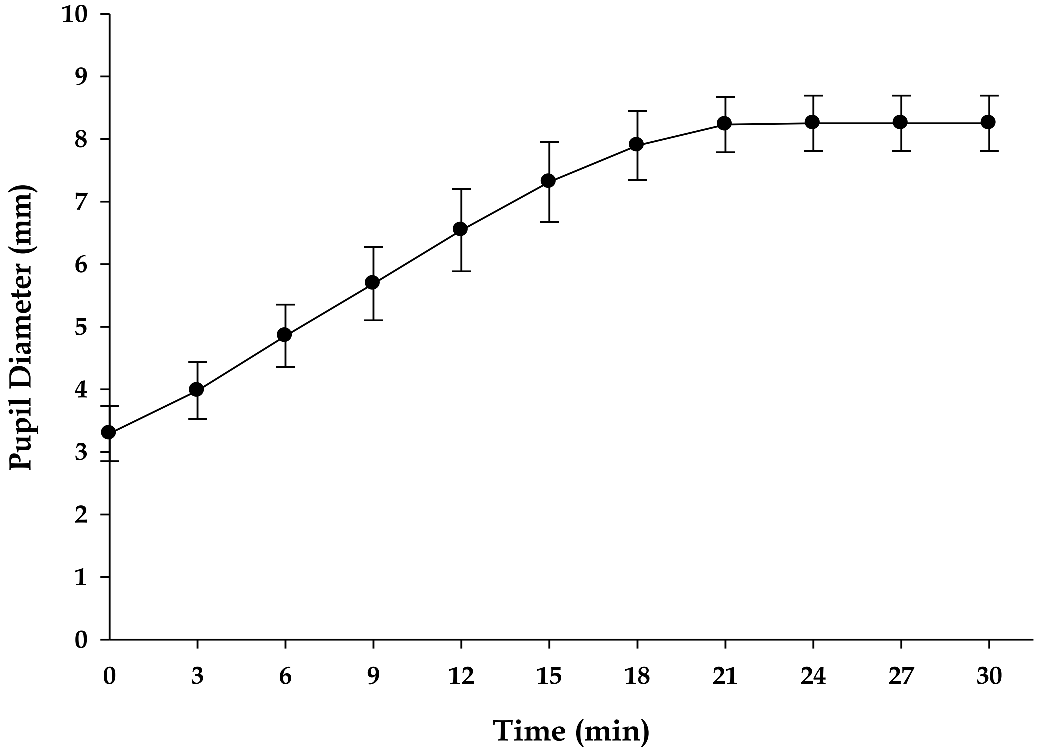

Figure 4.3 Pupil diameter variations with time after application tropicamide drop. Error bars represent ± 1 SD

The mean average changes in LDF parameters before and 30 min after the application of tropicamide with 4mm artificial pupil was presented in Table 4.1 and without artificial pupil was presented in Table 4.2. All CVs (coefficient of variation) of LDF flow parameters with 4 mm artificial pupil were between 3.2% and 9.6% and without artificial pupil were between 5.3% and 19.2%. Variability of Volume was higher than that of Velocity and it was mostly responsible for the variability in ChBF. The maximum changes (MD) from the baseline in individuals are shown in Table 4.1 and Table 4.2. The minimum sample size required to detect the significant changes in the variation in LDF parameters with 95% confidence level are 12.

Table.4.1 Velocity, Volume and Flow before and 30 min after application of one drop of 1% tropicamide with 4 mm artificial pupil. Coefficient of variation (CV) and maximum deviation from baseline value in a single individual (MD) of the LDF parameters as calculated from the 11 measurements. Data are presented as mean (over all 12 subjects) ± standard deviation

	Before	After 30 min	CV	MD	R Value	Significance#
Velocity(Hz)	1.166±0.27	1.163±0.28	3.2±2.0%	8.6%	0.18	P=0.59
Volume a.u)	0.235±0.18	0.235±0.18	9.6±4.7%	16.5%	0.37	P=0.26
Flow (a.u)	0.241±0.17	0.243±0.16	7.3±3.7%	21.8%	0.23	P=0.49
DC (V)	0.307±0.12	0.327±0.13	4.8±2.0%	9.3%	0.51	P=0.11

Two tailed parried student t-test

Table.4.2 Velocity, Volume and Flow before and 30 min after application of one drop of 1% tropicamide without artificial pupil. Coefficient of variation (CV) and maximum deviation from baseline value in a single individual (MD) of the LDF parameters as calculated from the 11 measurements. Data are presented as mean (over all 12 subjects) ± standard deviation

	Before	After 30 min	CV	MD	R Value	Significance#
Velocity(Hz)	1.569±0.39	1.727±0.39	5.3±3.0%	12.2%	0.79	P=0.01*
Volume a.u)	0.481±0.38	0.544±0.38	19.2±11.4%	37.6%	0.72	P<0.02*
Flow (a.u)	0.897±0.97	1.012±1.05	18.3±10.1%	36.2%	0.81	P<0.01*
DC (V)	0.360±0.19	0.397±0.14	17.3±9.5%	21.5%	0.43	P=0.19

Two tailed parried student t-test * Significant change

Experiment 1. Does Tropicamide affect subfoveal choroidal blood flow?

In order to determine whether Tropicamide has an effect on the LDF parameters, independently from the pupil dilatation, measurements were performed through a 4-mm artificial pupil placed just in front of the eye. This diameter was the smallest allowed by the measuring scheme of the Topcon based LDF device in which the laser beam is delivered along the fundus illumination system of the camera and separated from the detected scattered light, in conformity with the Gullstrand principle for reflection free fundus imaging.

In a darkened room, the LDF parameters were recorded during approximately 1 min, every 3 min for up to 30 min following the application of a drop of Tropicamide 1% at time 0 sec. The eye measured was selected randomly. LDF recordings were obtained from 12 subjects (4 males and 8 females). Figure 4.4 shows plot of the mean values of these parameters as a function of time. Velocity, Volume and ChBF demonstrated a non significant change of 0.7% ($p>0.05$), 2.8% ($p>0.05$), and 1.1% ($p>0.05$) respectively during the 30 min of pupil dilatation. These increases did not correlate significantly with the percentage increase of the DC (4.3%, $p>0.05$).

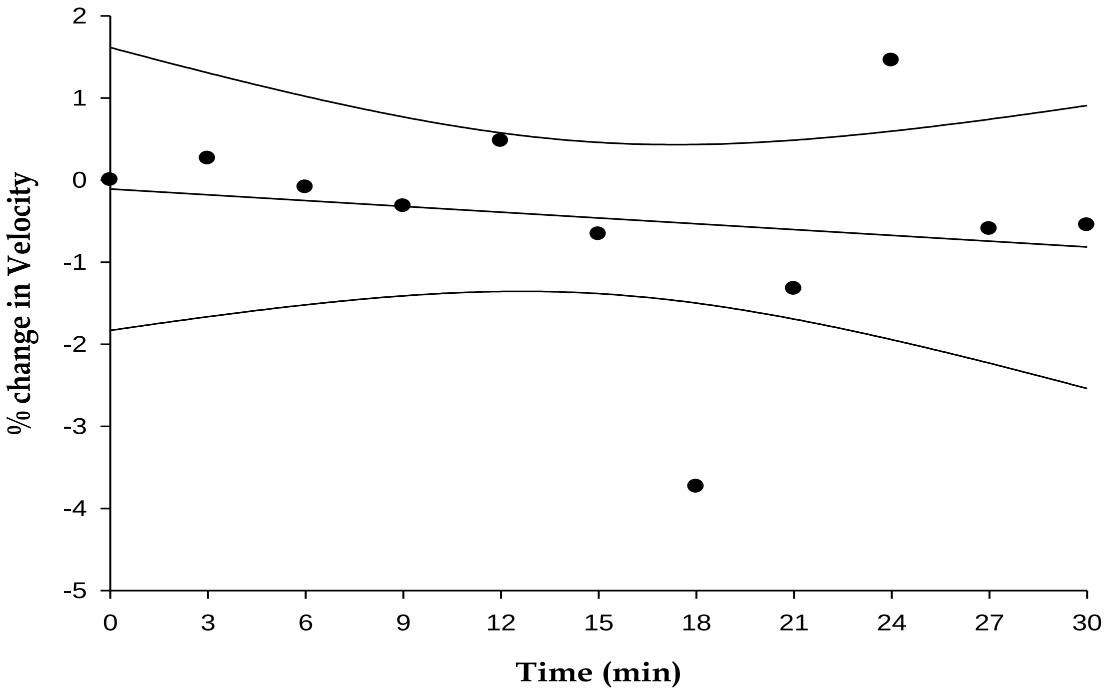

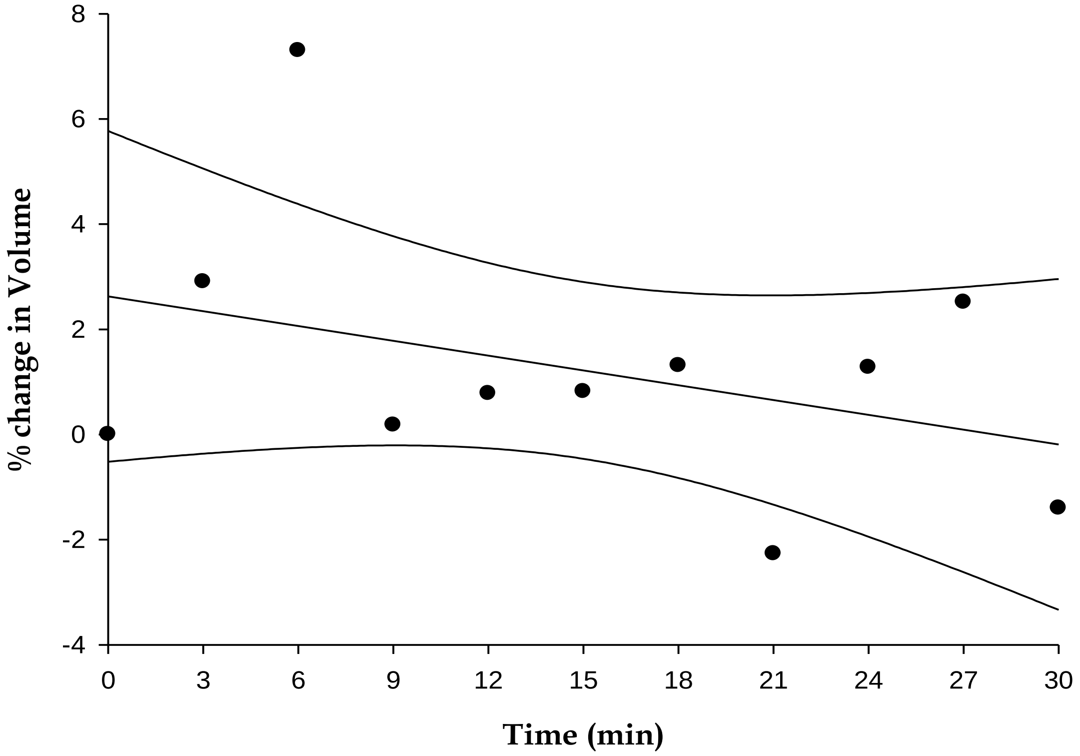
8
6
4
2
0
-2
-4
% change in Volume
0
3
6
9
12
15
18
21
24
27
30
Time (min)

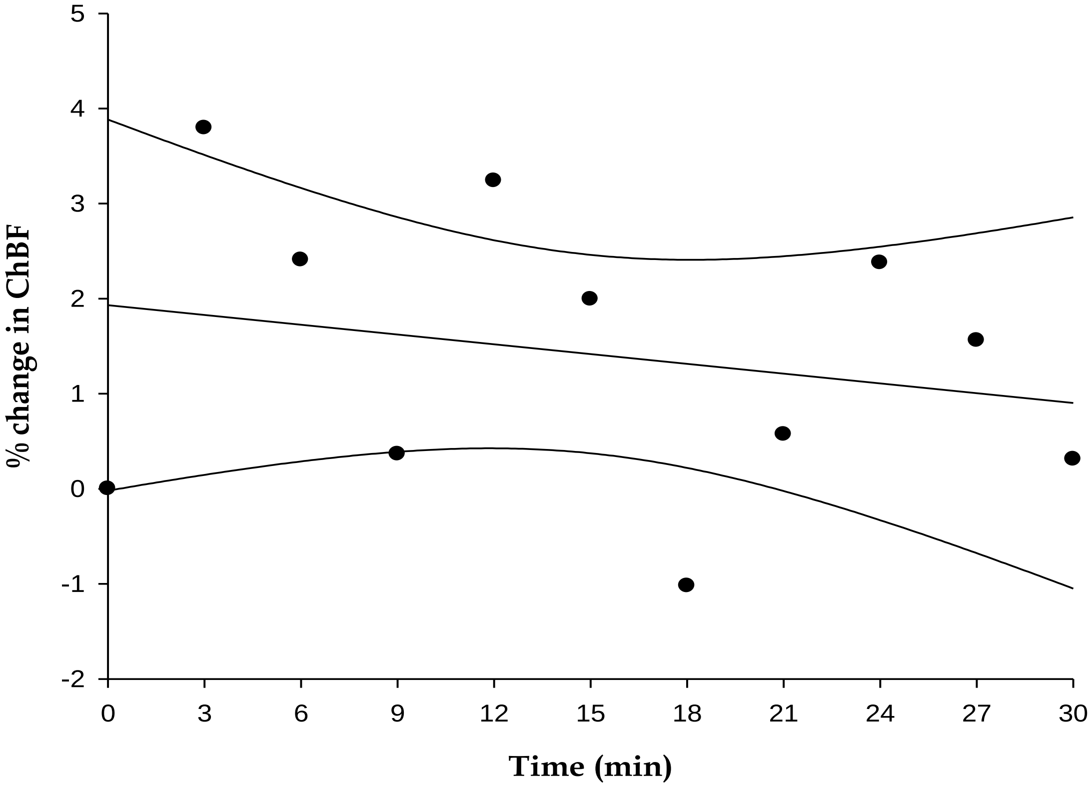
5
4
3
2
1
0
-1
-2
% change in ChBF
0
3
6
9
12
15
18
21
24
27
30
Time (min)

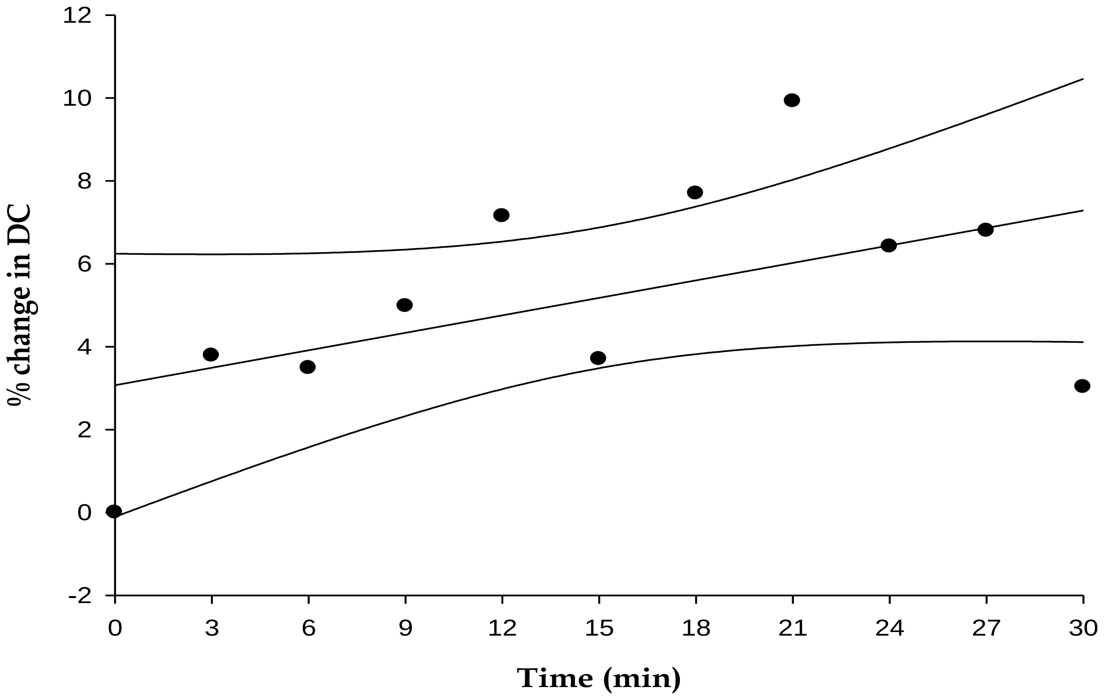

Figure 4.4 Percentage change in LDF parameters as function of time with 4 mm artificial pupil

Experiment 2. Does the size of the pupil influence the measurement of subfoveal choroidal blood flow?

In a second series of measurements in 12 subjects (3 males and 9 females), among them were 6 who had participated in the first experiment and 6 new subjects, similar measurements were performed without artificial pupil.

Figure 4.5 shows plot of the mean values of these parameters as a function of time. All LDF demonstrate a significant increase of 9.0% ($p=0.01$) for Velocity, 15% ($p<0.02$) for Volume, 17% ($p<0.01$) for ChBF. None of the changes in the LDF parameters correlated with the changes in DC (6.7%, $p>0.05$).

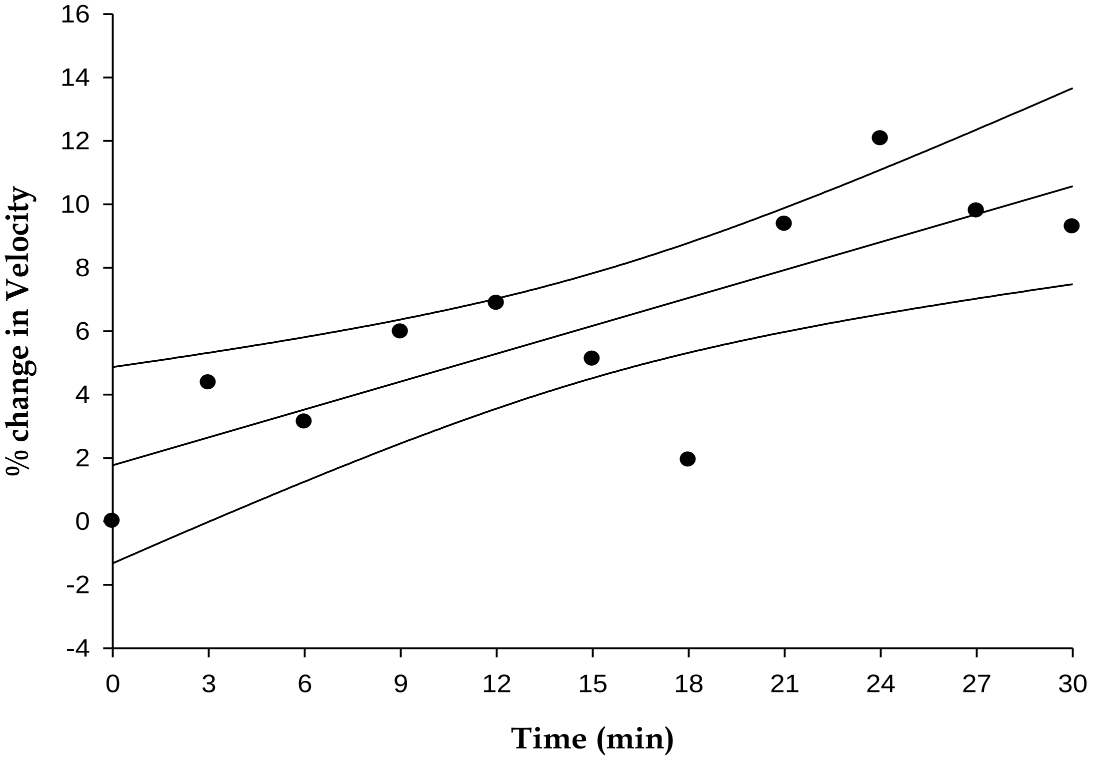
% change in Velocity
16
14
12
10
8
6
4
2
0
-2
-4
0
3
6
9
12
15
18
21
24
27
30
Time (min)

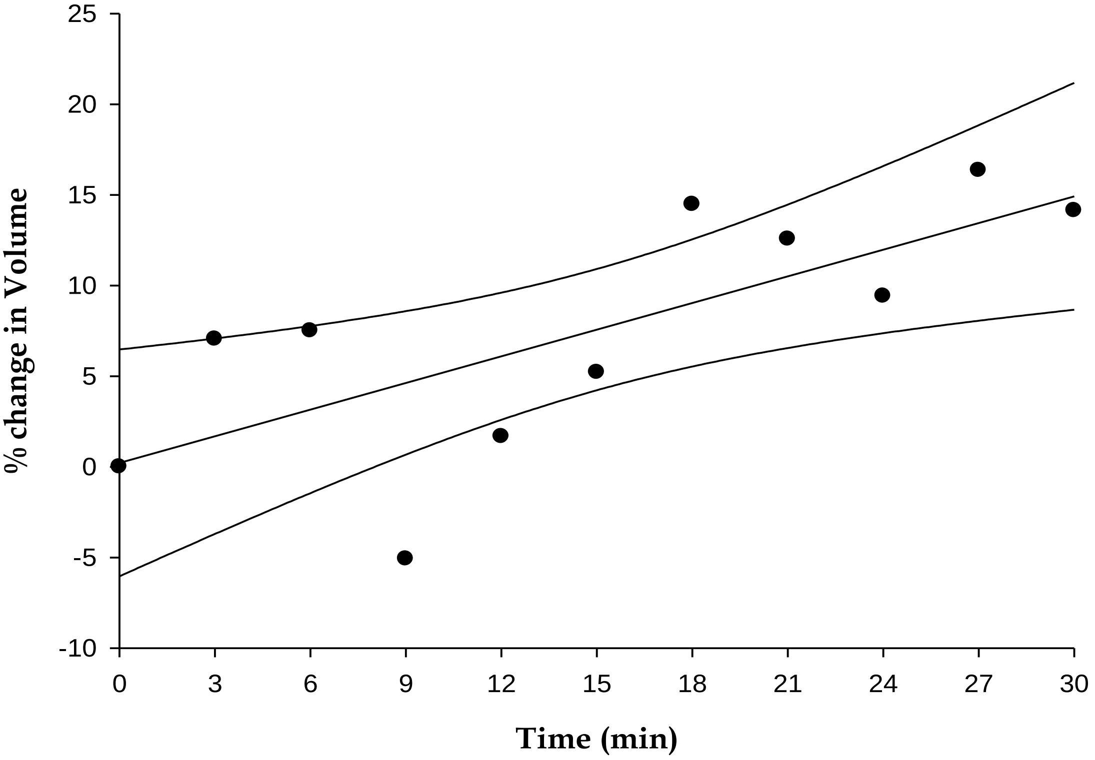
% change in Volume
25
20
15
10
5
0
-5
-10
0
3
6
9
12
15
18
21
24
27
30
Time (min)

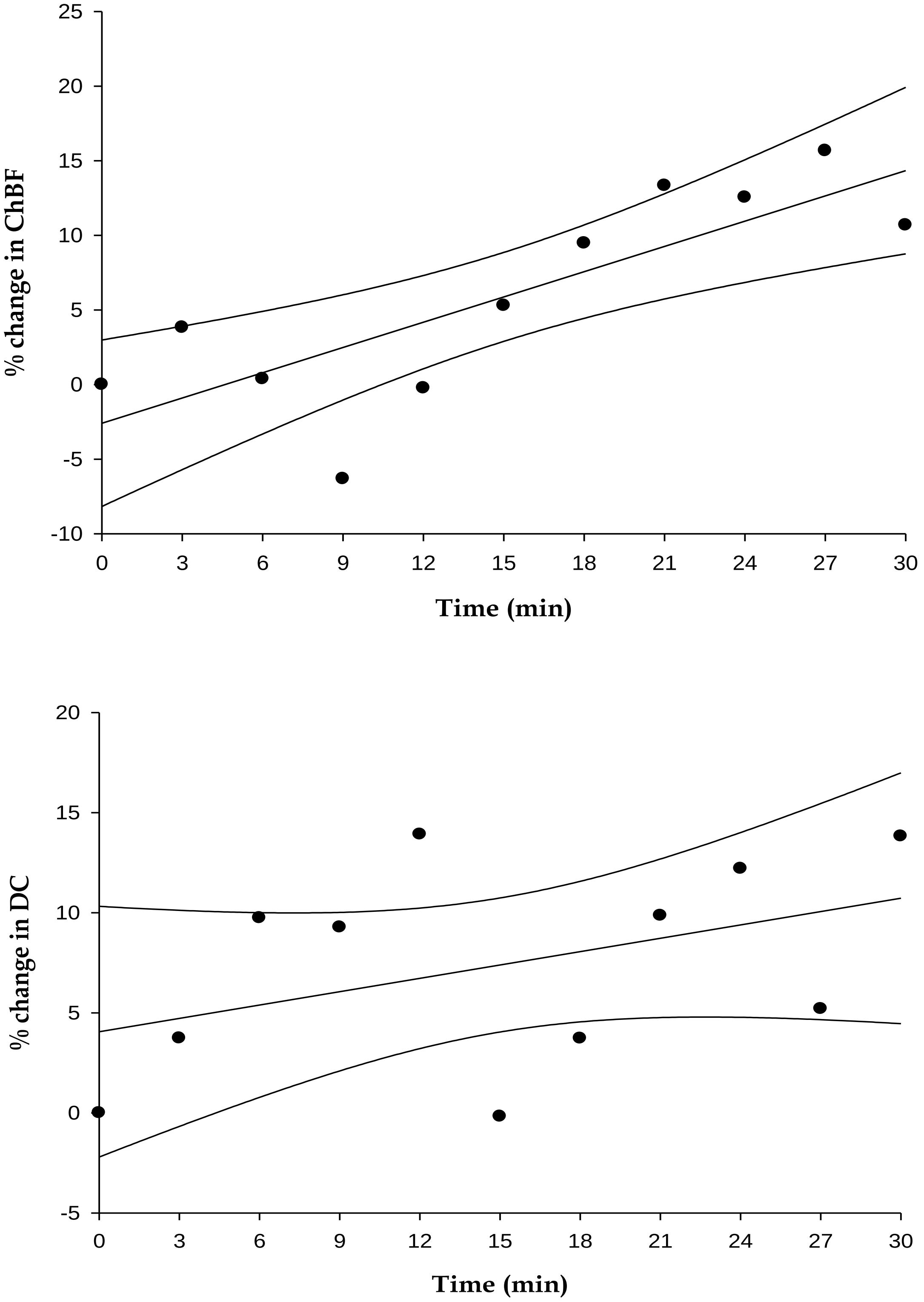

Figure 4.5 Percentage change in LDF parameters as function of time without artificial pupil

All the LDF parameters (Velocity, Volume and ChBF) in the subgroup of 6 subjects participated in both experiments were demonstrated a non significant change of 0.8% (p>0.05), 6.7% (p>0.05), and 7.2% (p>0.05) respectively during the 30 min of pupil dilatation with 4 mm artificial pupil placed directly in front of the cornea. These increases did not correlate significantly with the percentage increase of the DC (4.7%, p>0.05). However, statistically significant increases of 8.2% (p<0.01) for Velocity, and 21% (p<0.05) for ChBF were observed in the measurement performed without the 4mm artificial pupil. None of the changes in the LDF parameters correlated with the changes in DC (7.2%, p>0.05).

Figure 4.6 shows plot of the mean values of percentage change in LDF parameters as a function of mean values of percentage change in pupil diameter with a 4 mm artificial pupil directly placed in front of the eye. All the LDF demonstrated a non significant change of 2.4% (p>0.05) for Velocity, 3.1% (p>0.05) for Volume, 1.3% (p>0.05) for ChBF, and 5.1% (p>0.05) for DC. These increases did not correlate significantly with the increases of pupil diameter.

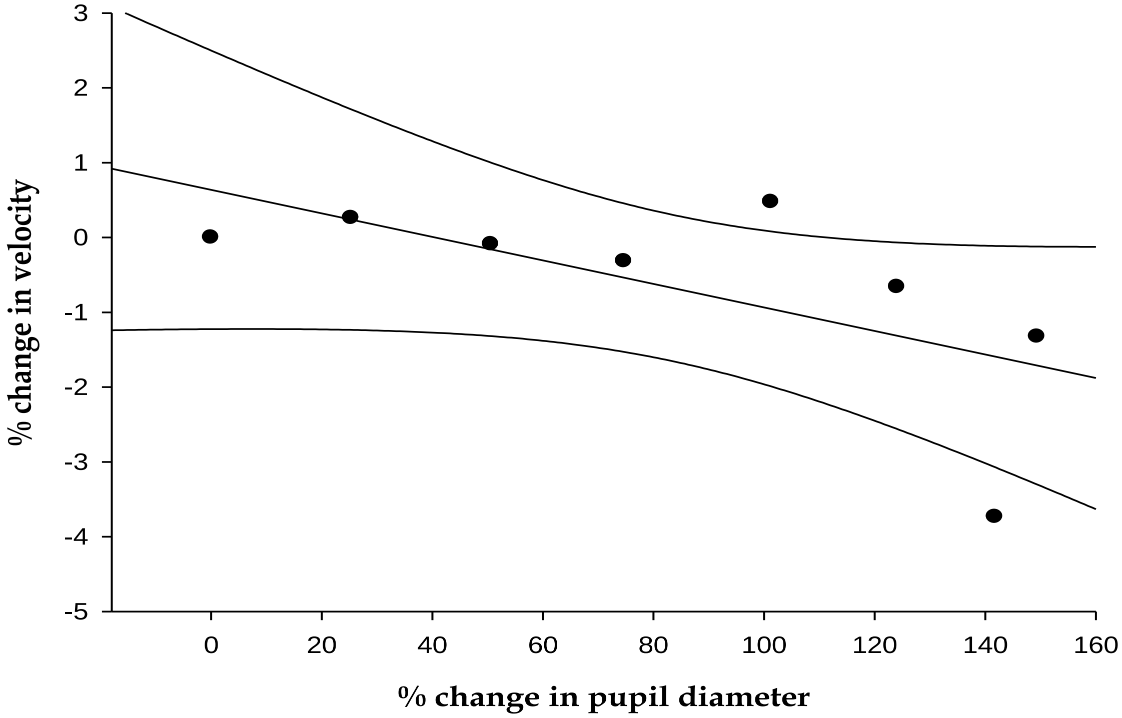

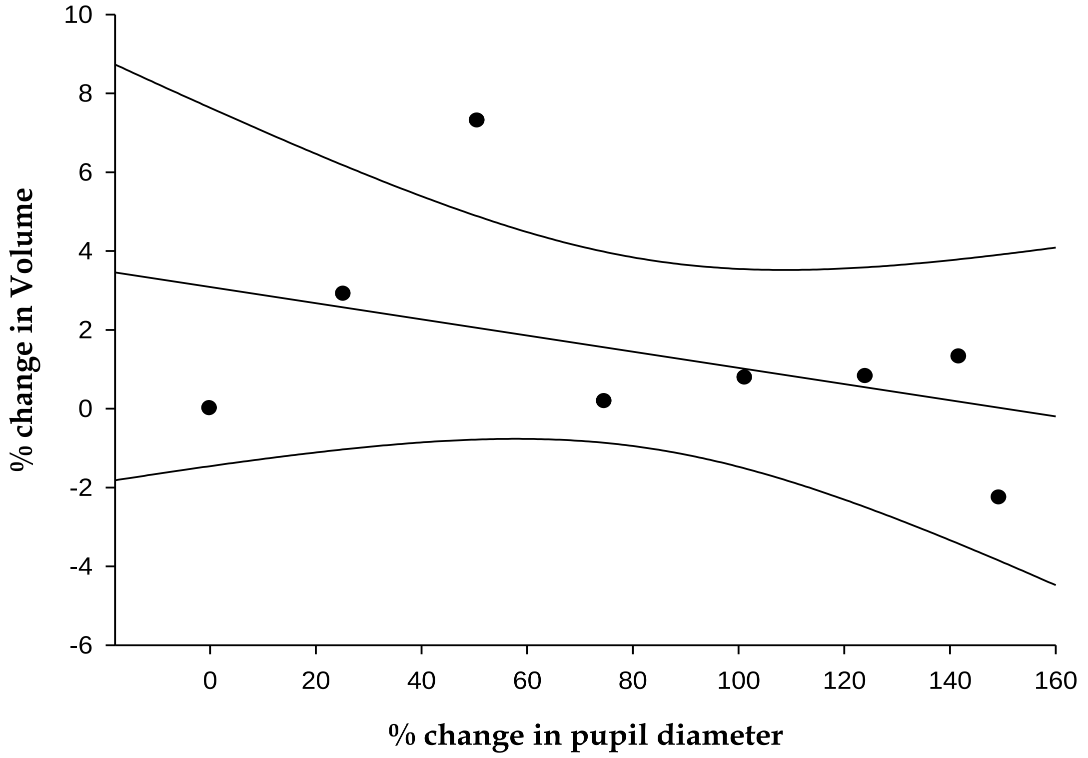

10
8
6
4
2
0
-2
-4
-6
0
20
40
60
80
100
120
140
160
% change in Volume
% change in pupil diameter

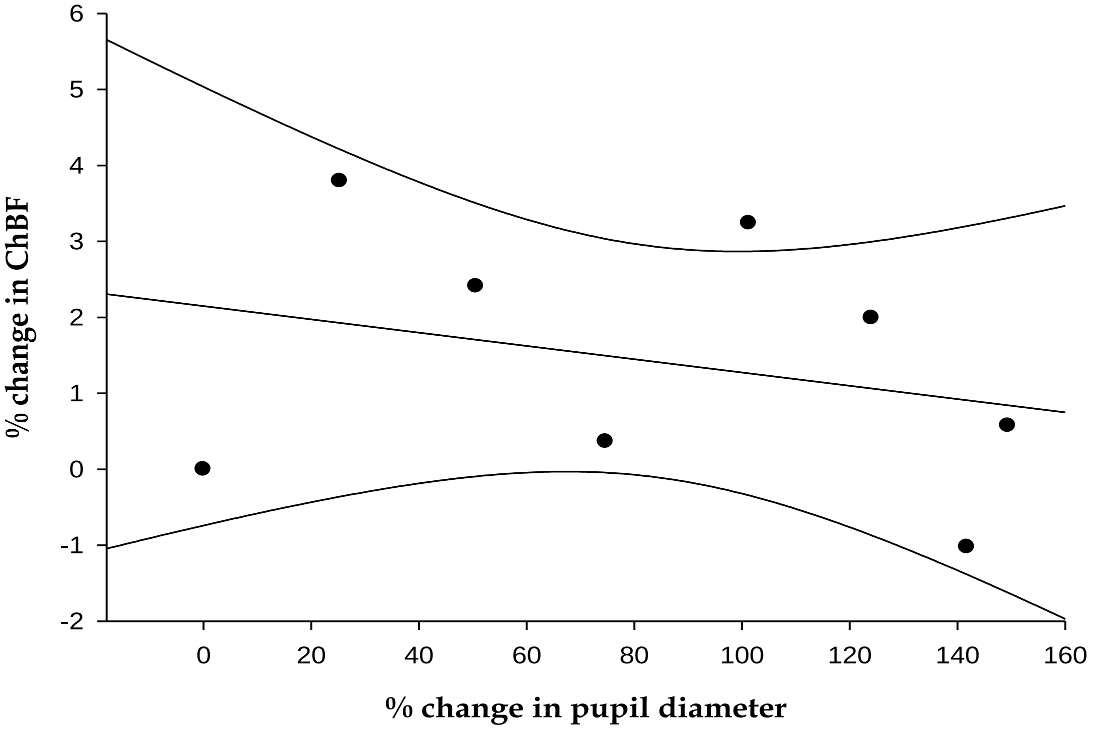

6
5
4
3
2
1
0
-1
-2
0
20
40
60
80
100
120
140
160
% change in ChBF
% change in pupil diameter

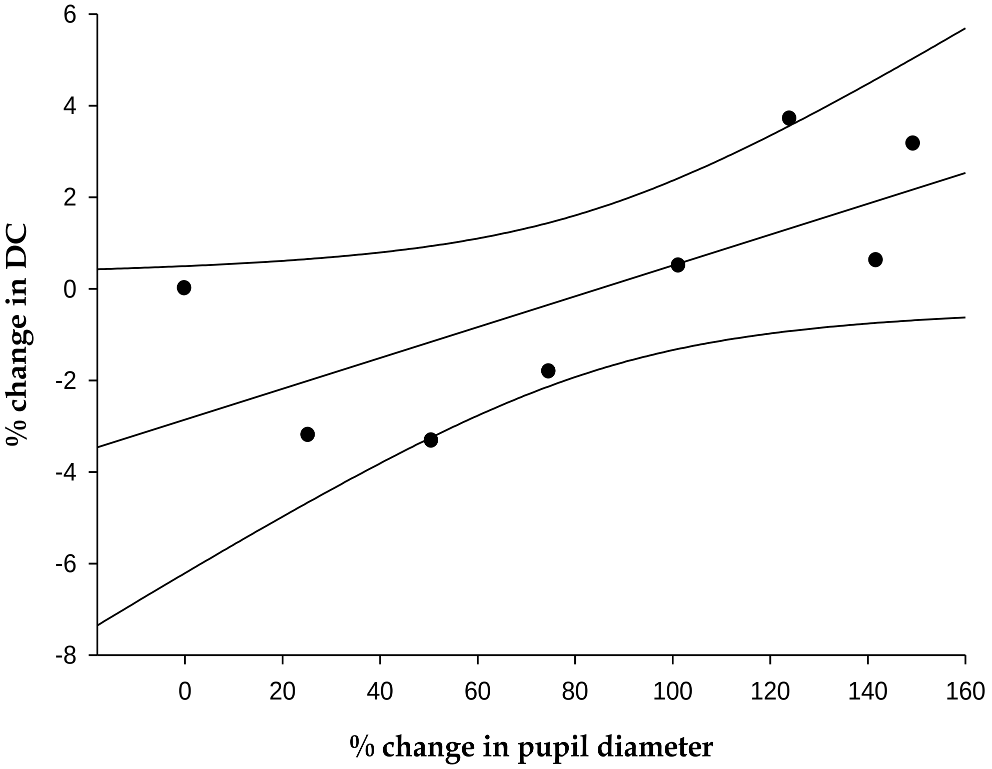

Figure 4.6 Percentage change in LDF parameters as function of percentage change in pupil diameter with 4 mm artificial pupil

Figure 4.7 shows plot of the mean values of percentage change in LDF parameters as a function of mean values of percentage change in pupil diameter without 4 mm artificial pupil in front of the eye. All the LDF demonstrate a significant increase of 5.4% ($p<0.05$) for Velocity, 9.0% ($p =0.03$) for Volume and 10% ($p<0.01$) for ChBF. None of the changes in LDF parameters correlated with the changes in DC (3.3%, $p>0.05$). These increases in LDF flow parameters shows significant correlation with the increases of pupil diameter.

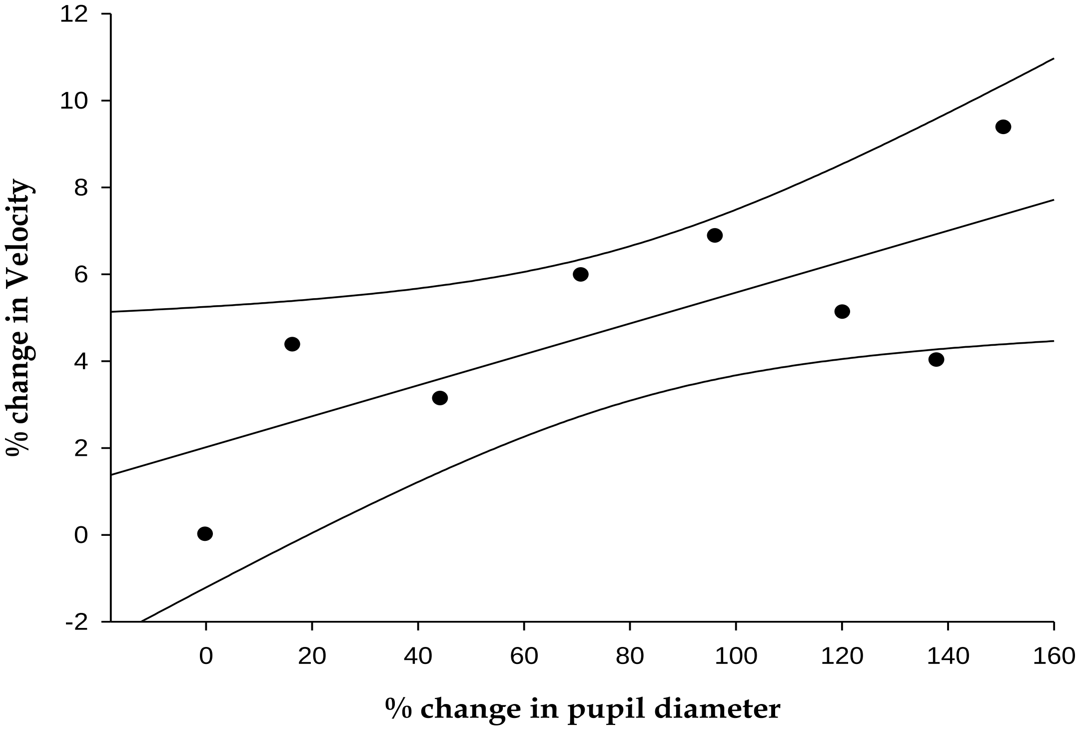
12
10
8
6
4
2
0
-2
% change in Velocity
0
20
40
60
80
100
120
140
160
% change in pupil diameter

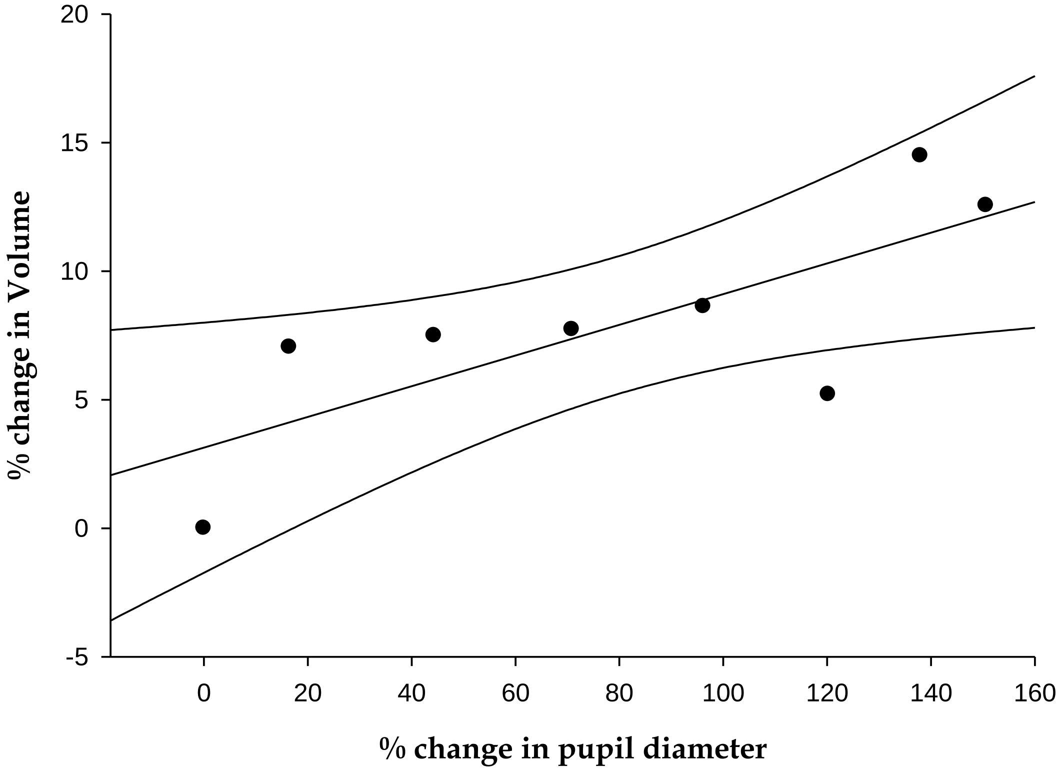
20
15
10
5
0
-5
% change in Volume
0
20
40
60
80
100
120
140
160
% change in pupil diameter

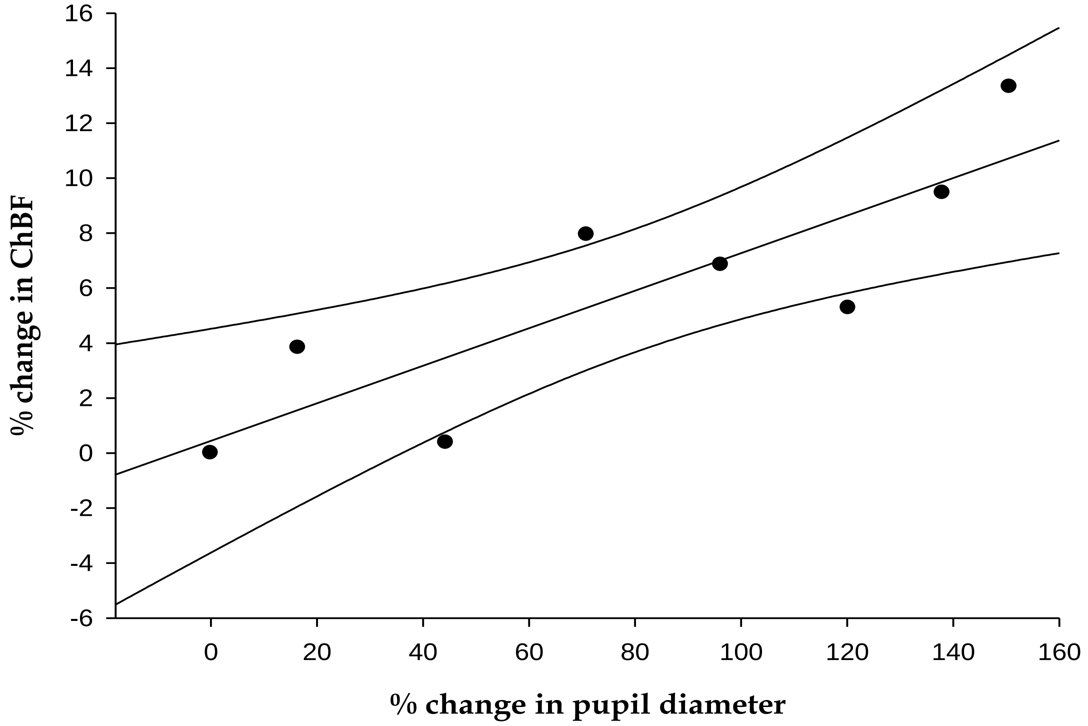

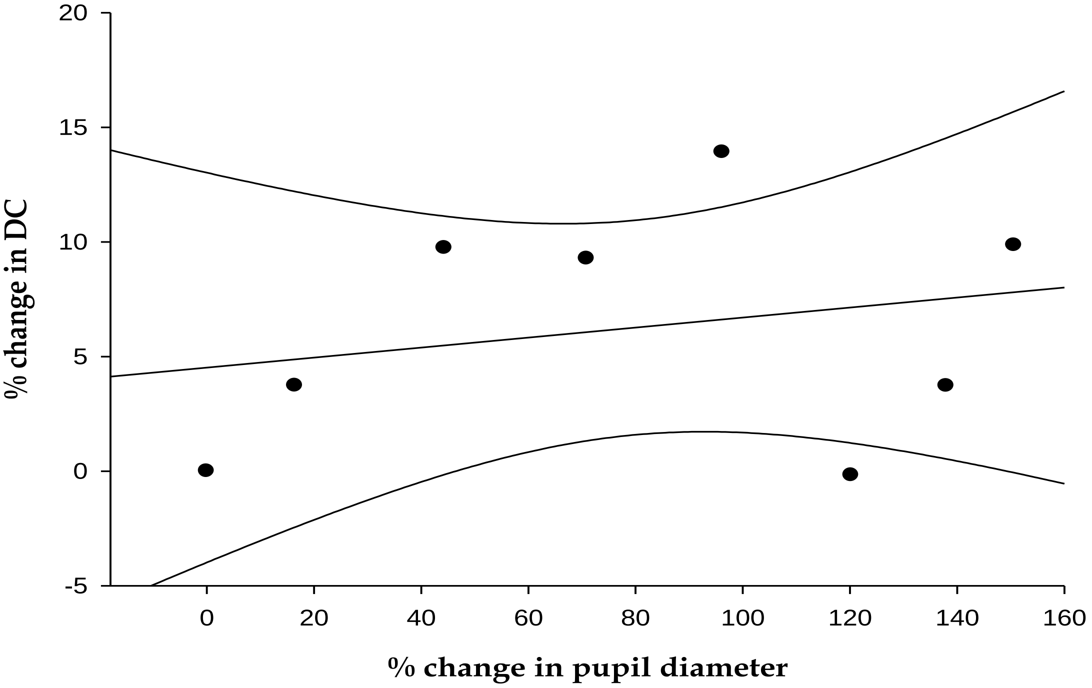

Figure 4.7 Percentage change in LDF parameters as function of percentage change in pupil diameter without artificial pupil

4.3 Discussion

In the present study, we investigated the variation in LDF parameters in choroidal region of human fundus with and without 4mm artificial pupil placed directly in front of the human eye. One experienced operator performed each measurement during the study to avoid the variation in inter-observer differences. The variability in LDF parameters are analysed by employing required number of participants in this study. The pervious study on the effect of two drops of 1% tropicamide on ocular blood flow in the rabbits shows no significant difference in blood flow [110]. Similar studies on macular blood flow [111] using blue field simulation technique, and optical nerve head circulation using scanning laser Doppler flowmeter [112] were found no significant changes blood flow. The LDF provides only relative measurements of flow parameters [15]. The flow parameters depend upon the scattering and absorption of the tissues, when the tissue is illuminated by a coherent- laser the moving red blood cells scattered the light in all direction leads to Doppler shifts with different frequencies. The frequency shift is not only depending on the velocity of the red blood cells and also depends on the incident and scattering angles of the laser beam on the tissue surface [105]. The average velocity, volume and flow of the red blood cells are determined based on a theory of light scattering in tissue in relative units [113]. The increases in pupil diameter during both experimental activities are very similar. The artificial pupil placed in front of the eye to keep the scattering geometry as same for the entire duration of the measurement. In conclusion, the present study, we investigated the variation in LDF parameters from the subfoveal choroidal region of human fundus with and without a 4 mm artificial pupil placed directly in front of the human eye. The use of an artificial pupil resulted in Velocity, Volume and ChBF data which were not affected by the pupil dilatation process. This was not the case when there was no artificial pupil in front of the cornea. Most probably, changes in pupil diameter in this case resulted in larger scattering angles for the beam emerging out of the pupil and also bigger variations of the location of the incident beam at the pupil. Both presumably affect the LDF values and their variability. Our result show that, as found for the retinal [6] and central retinal artery [114], tropicamide and the resulting pupil dilatation do not affect significantly the subfoveal choroidal LDF parameters. We suggest that when measuring the effect of various pharmacological agents on ChBF by LDF, the introduction of an artificial pupil may be recommended [115] in order to decrease the variability of the data and, as a consequence, the sensitivity of the LDF technique to detect changes in ChBF.

CHAPTER 5

Ocular fundus reflectometry

The fundus reflectometry is a technique to estimate the intensity of the optical light backscattered from the back of the eye. This technique is based on the properties of absorption and scattering of the tissues of interest. The study of reflectance at wavelengths in near infrared (NIR: 700-1000 nm) have considerable effect on neurovascular coupling (NC) at the optic nerve or the physiological mechanism that controls the blood perfusion in microcirculation [116] of the optic nerve support the neural activity evoked by the stimulus on human fundus [117]. Recently, changes in reflectance in the papillary region of the fundus under visual stimulation in humans have been detected [118] and the same was studied in monkeys in flash [119]. The aim of the study was to detect the changes in the fundus reflectance in near infrared under visual stimulation to understand the correlation between neural activity and physiological changes induced by the light [120]. The tissues to be investigated are illuminated by a non-harmful low power optical source. This technique has an advantage of study the mechanisms of changes in the activity of central nervous system. Ocular fundus reflectometry was useful for the study of pathogenesis and early diagnosis of eye diseases, such as glaucoma and diabetic neuropathy [67].

5.1 Basic Principle

An optical beam at wavelength λ with intensity $I_i(\lambda)$ was focused on the tissue at back of the eye and backscattered by the tissue itself was collected by the measuring system. The intensity of the light backscattered from eye was $I_b(\lambda)$. The general equation of reflectance $R(\lambda)$ was defined as

$$R(\lambda) = \frac{I_b(\lambda)}{I_i(\lambda)} \tag{5.1}$$

The cross sectional view of the human eye fundus was shown in Figure 5.1. The photoreceptors are specialized type of neuron found in eye retina able to convert the light into signals that can stimulate biological process. The photosensitive ganglion cells of the retina involved in various reflexive responses of the brain and body to the presence of light, such as the regulation of circadian rhythms, pupillary reflex and other non-visual responses to light, is called melanopsin. When light activates the melanopsin signalling system, the melanopsin containing ganglion cells discharge nerve impulses that are conducted through their axons to specific brain targets.

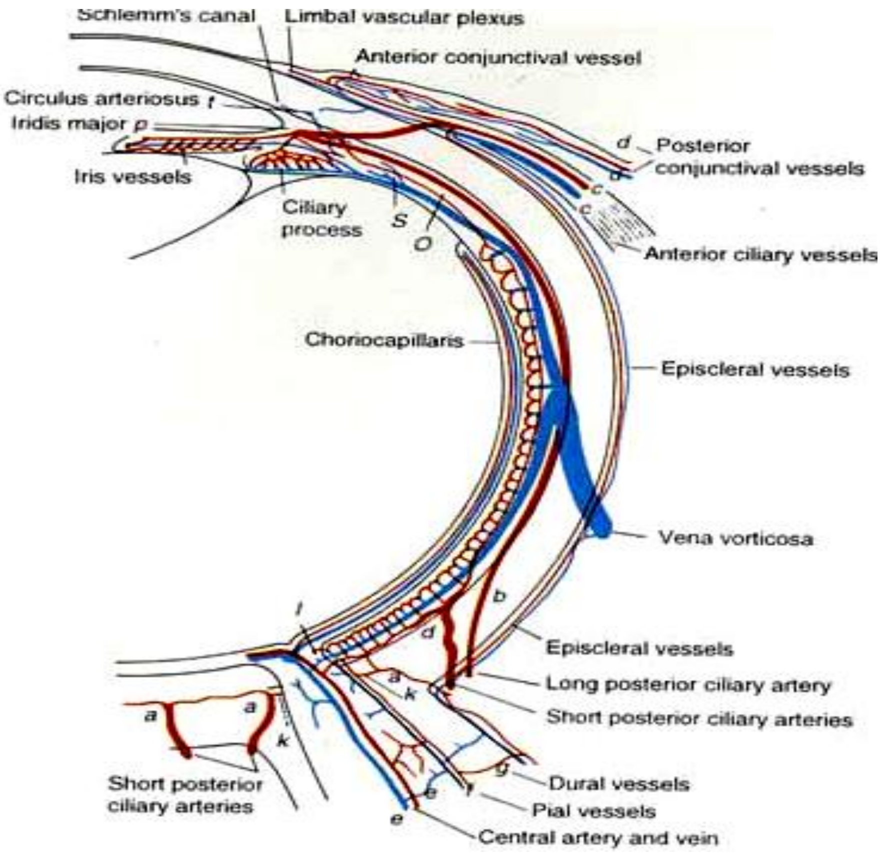

Figure 5.1 Cross section of optic nerve

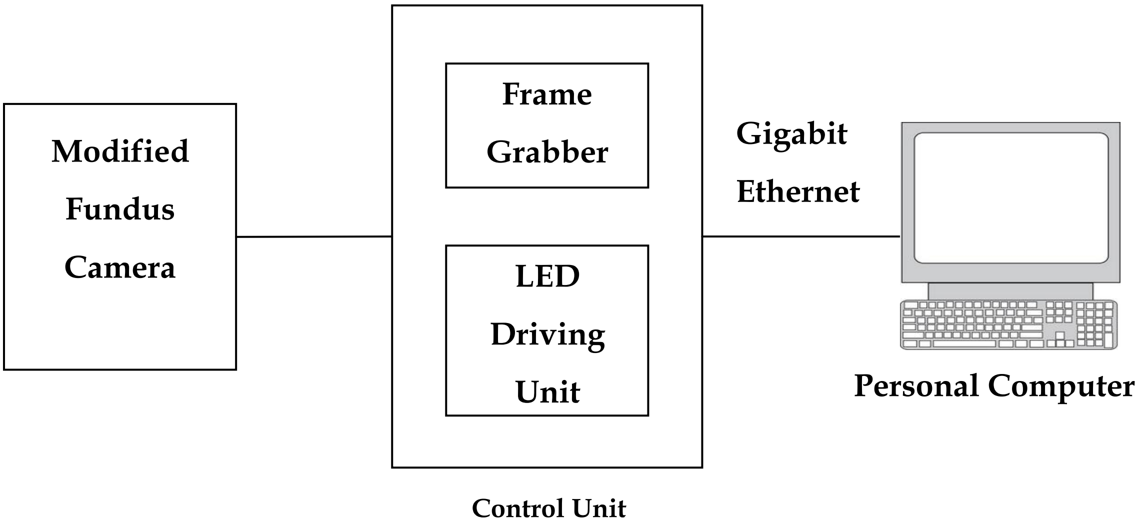

Figure 5.2 Block diagram of fundus camera based reflectometry

5.2 Description of the Instrument

The newly developed system is based on a modified commercial fundus camera (TRC-WT, Topcon, Japan) [121]. The block diagram of the modified fundus camera based reflectometry was shown in Figure 5.2.

The optical layout modified fundus camera was shown in Figure 5.3. The standard fundus illumination lamp was removed and replaced by a NIR LED L1 (LED770-03AU, Roithner Lasertechnik, Austria). A LED L2 with Green, Blue and Yellowish green was introduced in the camera for flicker stimulation. The arrangement of the LED L2 was shown in Figure 5.9. The light from the LED L2 was diffused by a diffuser D and made to follow the same optical path as that of the Near Infrared beam emitted by L1. The light reflected by the fundus was focused onto two CCD video cameras VC (LDH0702/50, Philips, Holland and KPC-E20B11, KT&C, South Korea). A filter F was placed in front of VC. It transmitted only the NIR light to VC.

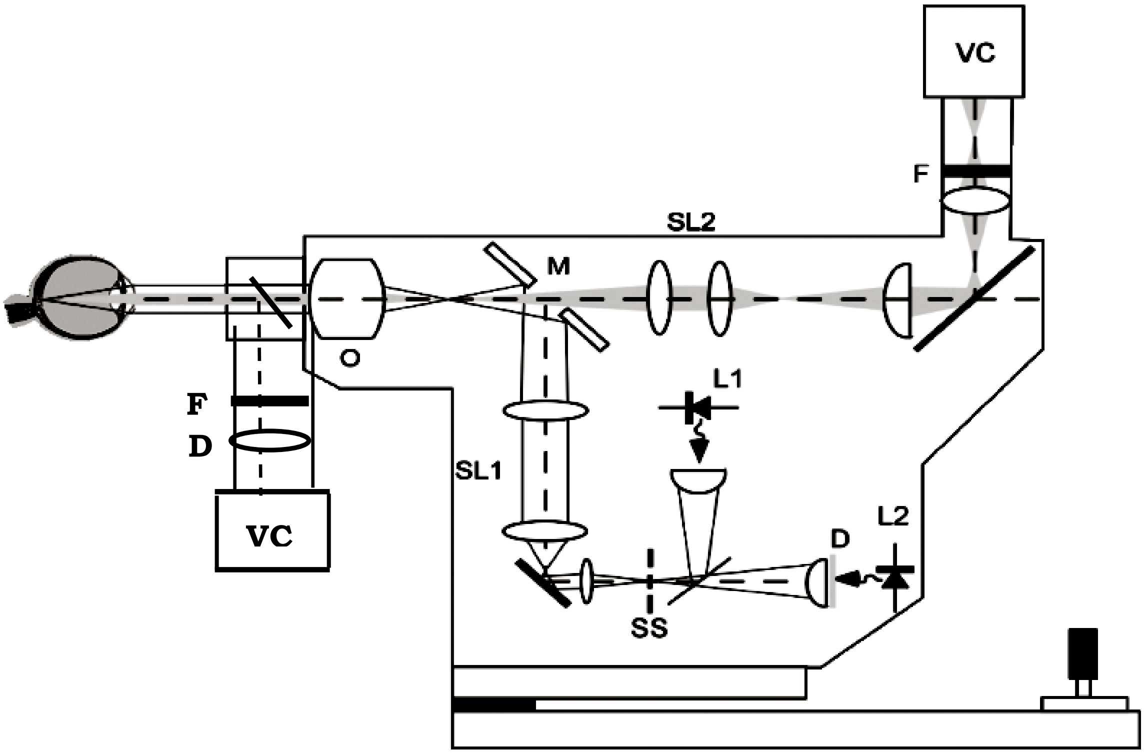

Figure 5.3 Optical layout of the modified fundus camera

Figure 5.4 Picture of the modified fundus camera

The LEDs L1 and L2 are controlled by a personal computer through USB port as shown in Figure 5.5. The LEDs are controlled by a software developed using Visual Basic. The LEDs L1 and L2 are driven by the adjustable current sources. The currents I1 and I2 are proportional to the voltages V1 and V2 provided by a digital to analog converter (DAC). The optical power of NIR LED can be adjusted by varying the currents between 0 to 100mA. The variable current to L1 varies the brightness of the image acquired by the CCD camera VC.

The flicker effect can be varied with the help of LED L2 in the range between 0 to 100mA. The driver allows adjusting the duty cycle between 0 to 100%, modulation frequency from 1 to 20 Hz and modulation depth between 0 to 100%. These calibration values are stored in a non volatile memory M.

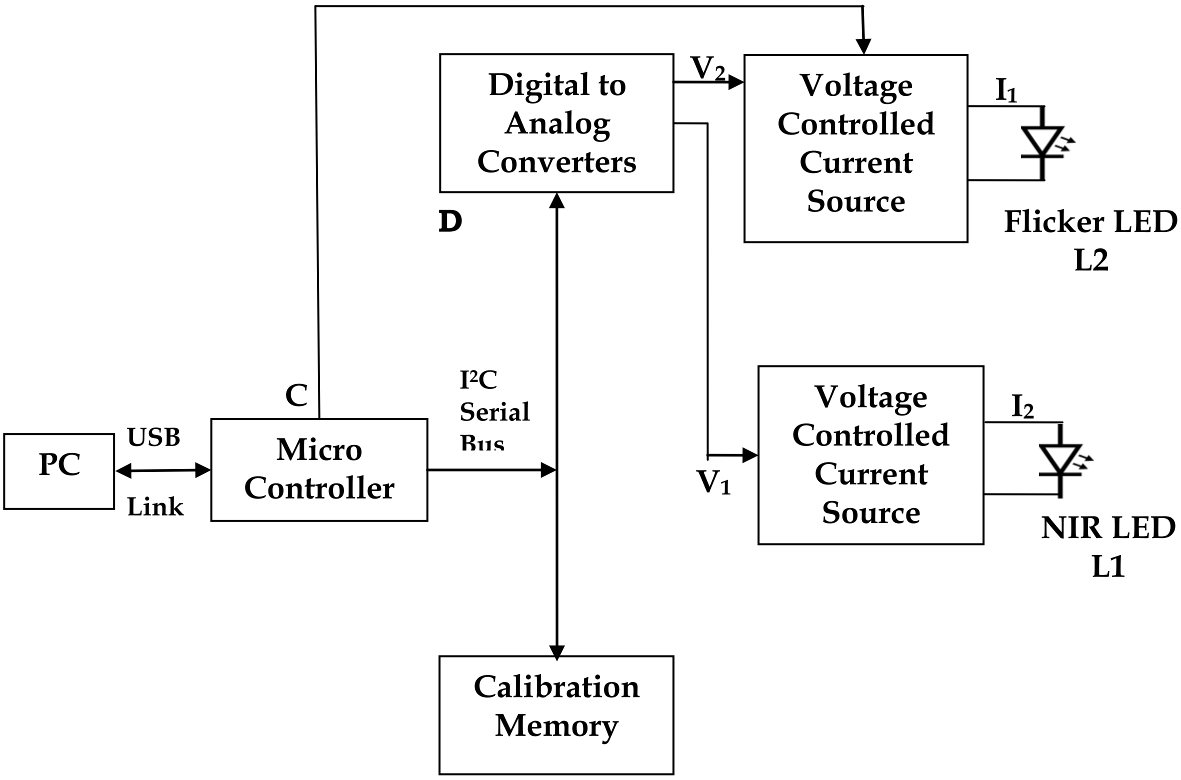

Figure.5.5. Block diagram of LED driving circuit

5.3 Characterization of LED sources

The brightness of the NIR LED controlled through a voltage controlled current source. The reflectance measurement depends on the wavelength and emission spectrum of the light source. The emission spectrum of the LED measured using a photonic multichannel analyzer (C5966, Hamamatsu Photonic K.K., Japan). The current supplied to the diode is adjusted digitally in steps upto 256 by a software control. The digital code generated by the microcontroller is converted into analog using a D/A converters. The analog output of the D/A converter is equal to the voltage across the diode. The current through the diode was controlled using a voltage to current source. The actual power emitted by the LED was determined using a linearity test by varying the current injected into the LED. Optical power measurements were taken at the reflectometer's output on the plane of the target cornea using a PC-controlled optical power meter (SH-TO-USB, Ophir Optronics, Israel) equipped with an optical head (PD300-UV-SH, Optronics, Israel). The calibration characteristic of the near infrared LED was shown in Figure 5.7. The linear regression coefficient of the calibration curve is R=1.

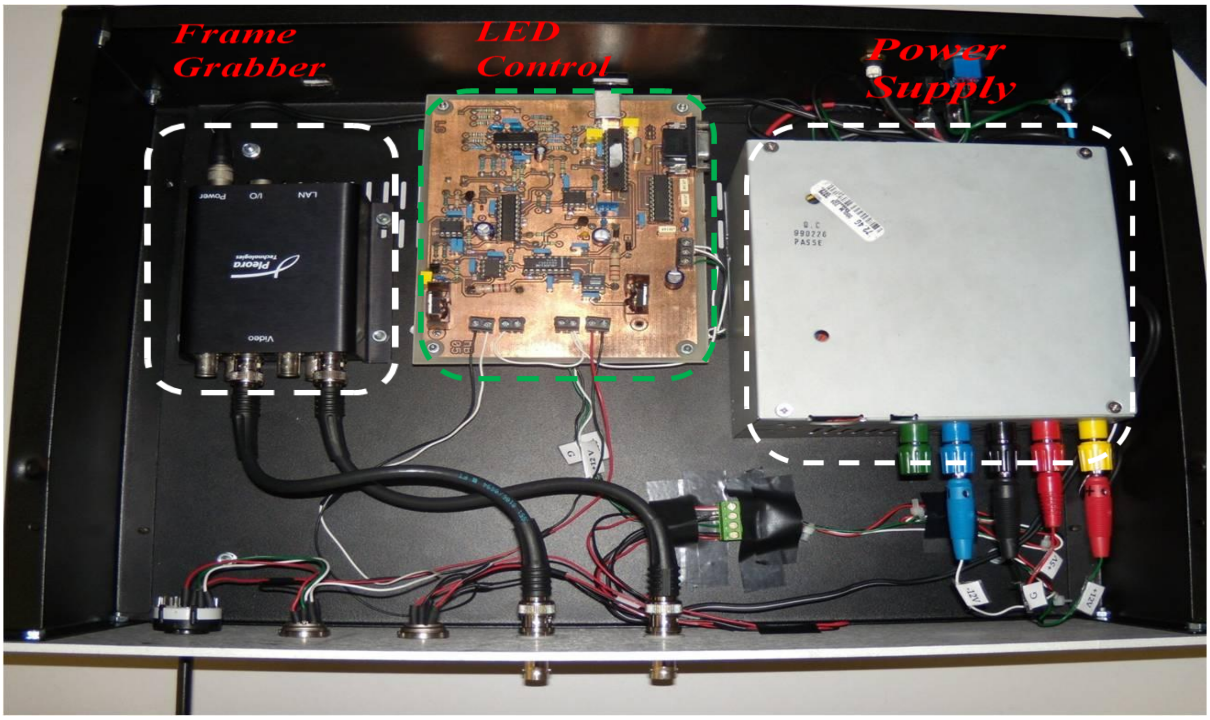

Figure 5.6 Picture of control unit

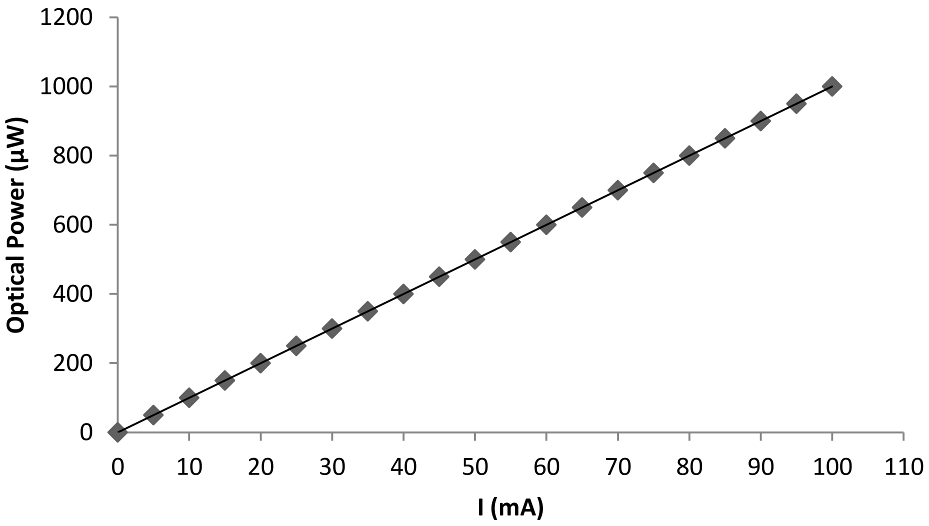

Figure 5.7 Calibration characteristics of NIR LED

The colour of the incident light changes the psychological and physiological response of the human eye. The rods on the retina are sensitive to the intensity of the light; they cannot differentiate between lights of different wavelengths. On the other hand, the cones contain colour sensitive cells. When light of a given wavelength enters the eye and strikes the cones of the retina, a chemical reaction is activated that results in an electrical impulse being sent along nerves to the brain.

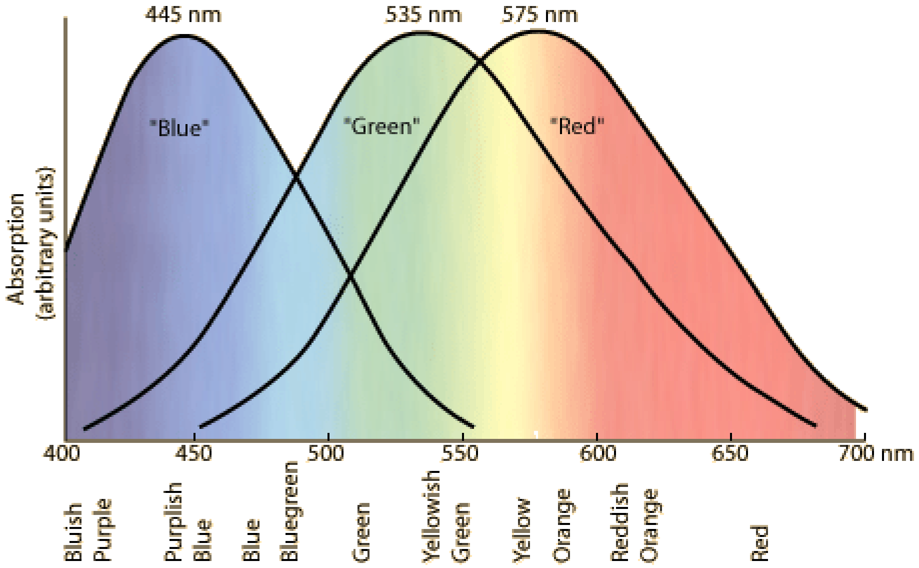

Figure 5.8 Cone sensitivity curve

There are three types of cones are present in human eye responsive to three different wavelengths of light. The cone response of the human eye for the different colour lights are shown in Figure 5.8.

Since the red cone is sensitive to a range of wavelengths, it is not only activated by wavelengths of red light, but also by wavelengths of orange light, yellow light and even green light. In the same manner, the green cone is most sensitive to wavelengths of light associated with the color green. The green cone can also be activated by wavelengths of light associated with the colors yellow and blue. The flicker stimulation LEDs are selected based on the peak wavelength of the cone response as mentioned in the cone sensitivity curve.

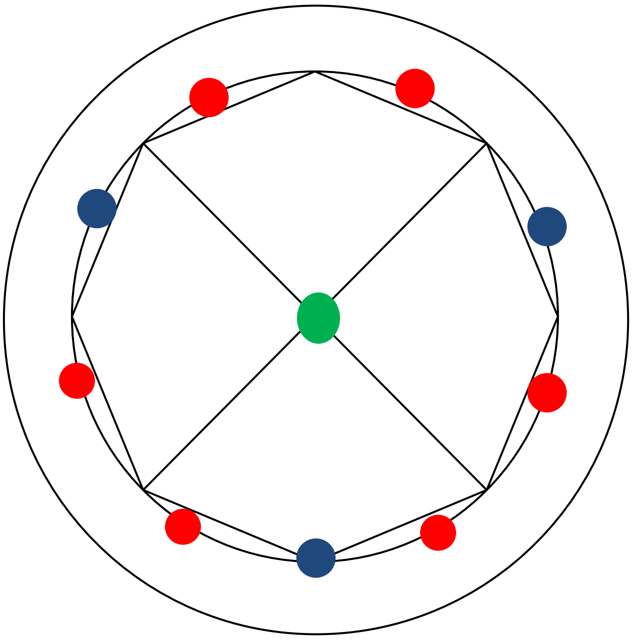

Figure 5.9 Flicker stimulation LEDs arrangement

Green LED (HLMP-CM34-X1000, Avago Technologies, USA) with peak wavelength 523 nm, Blue LED (L-53MBC, Kingbright, Taiwan) with peak wavelength 430 nm and Red LED (YPY3863X, Stanley, Japan) with peak wavelength 572 nm are arranged in a pattern shown in Figure 5.9. The flicker stimulation LEDs are calibrated similar to NIR LED by varying the current injected into the LED. The calibration curves of the flicker stimulation LEDs are shown in Figure 5.10.

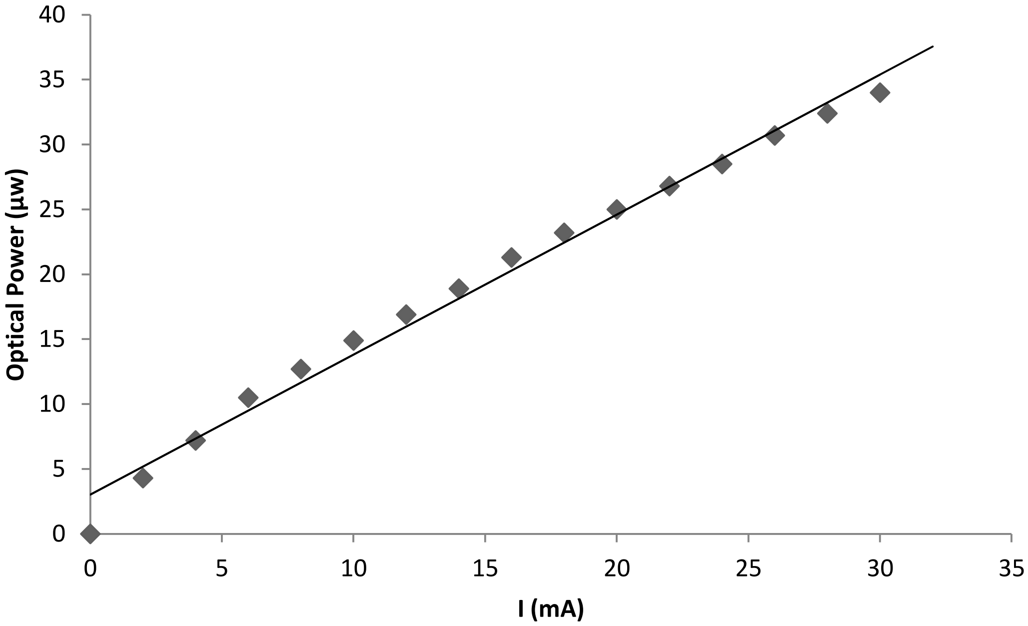
Optical Power (µw)
40
35
30
25
20
15
10
5
0
0
5
10
15
20
25
30
35
I (mA)

(a)

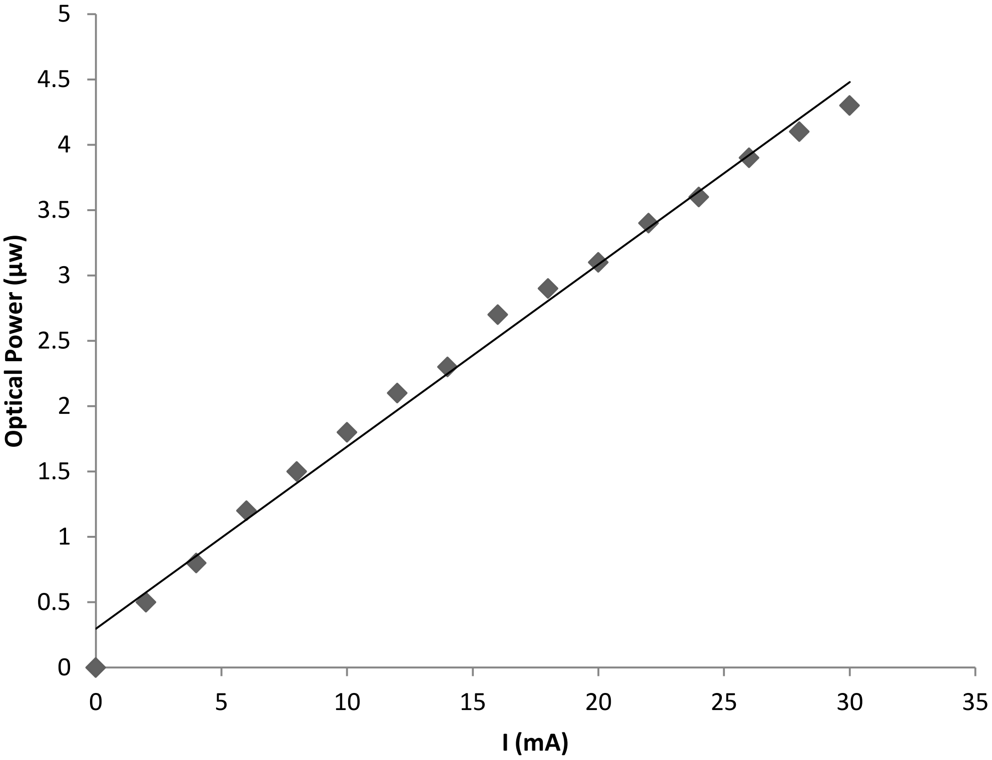
Optical Power (µw)
5
4.5
4
3.5
3
2.5
2
1.5
1
0.5
0
0
5
10
15
20
25
30
35
I (mA)

(b)

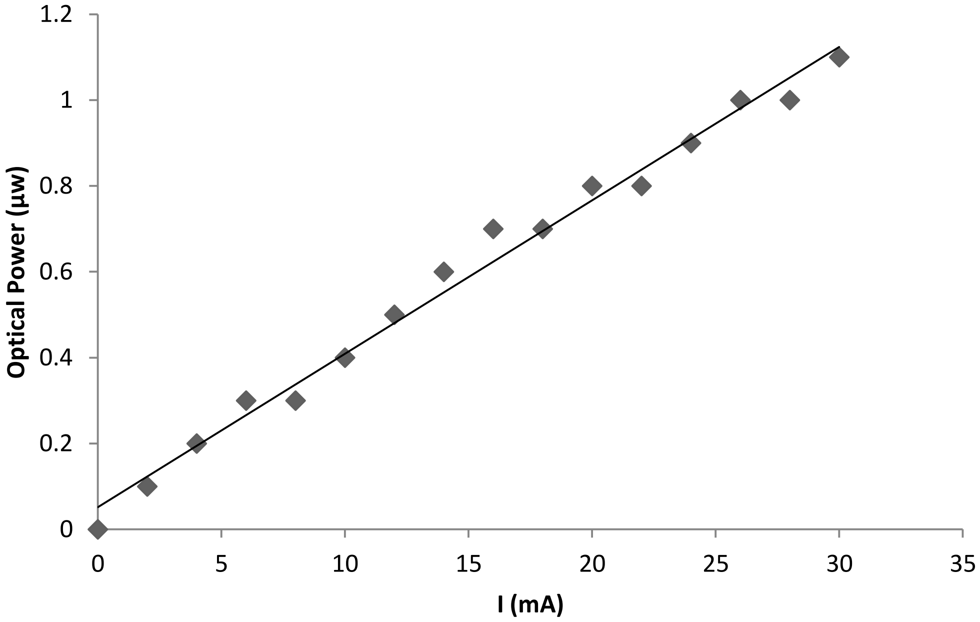

(c)

Figure 5.10 Calibration curves of flicker stimulation LEDs. (a) Green (b) Blue and (c) Red

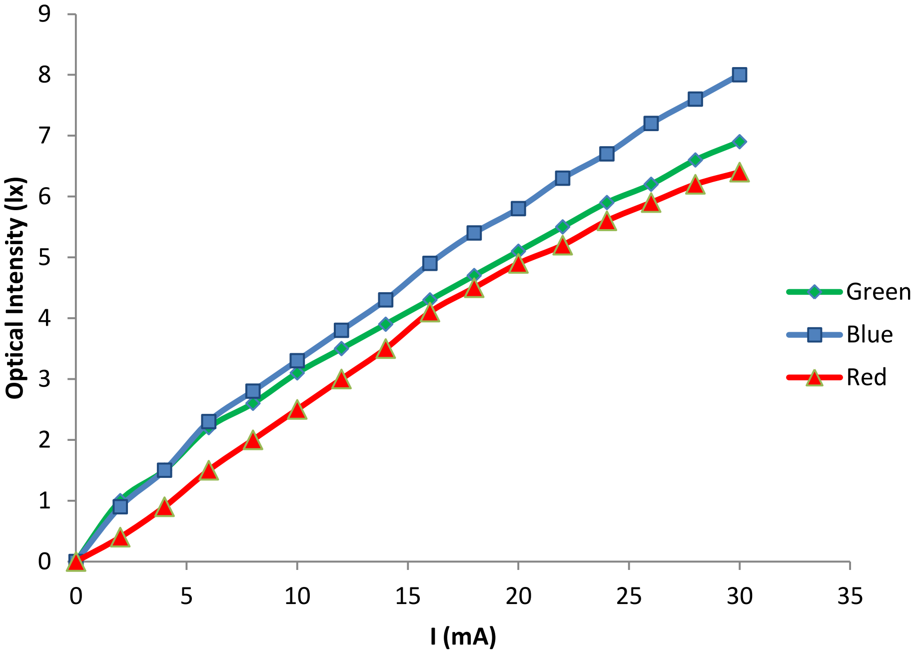

Figure 5.11 Calibration curve of flicker LED

The linear regression coefficients of the variation of optical power with the variation in injected current for all three LEDs are at 0.9. We are interested to study the response of the reflectance changes induced by visual stimulations of three different wavelengths at same intensity on human fundus. The LEDs arranged are as shown in Figure 5.9 to make the optical intensity impinging light on the human eye for all three wavelengths are equal. The optical intensity of the light sources is measured using a light meter (Delta Ohm HD9221, Italy). The calibration curve of light intensity with injected current is shown in Figure 5.11.

The stability of the optical sources are characterised using the optical power meter (SH-TO-USB, Ophir Optronics, Israel) equipped with an optical head (PD300-UV-SH, Optronics, Israel). The optical power emitted was measured separately for all LED continuously for 2 hours after a warm up period of 30 min. The NIR LED was set at an optical power output of 600 µw with an equivalent current of 59.82 mA measured using a high resolution digital multimeter (34401A, Hewlett-Packard, USA). The flicker Green LED was set at 1.7 µw, Blue at 1.2 µw and Red at 1 µw and the optical power emitted by the LEDs are measured over a period of 2 hours. The time courses of the stability of the optical output of all LEDs are shown in Figure 5.12.

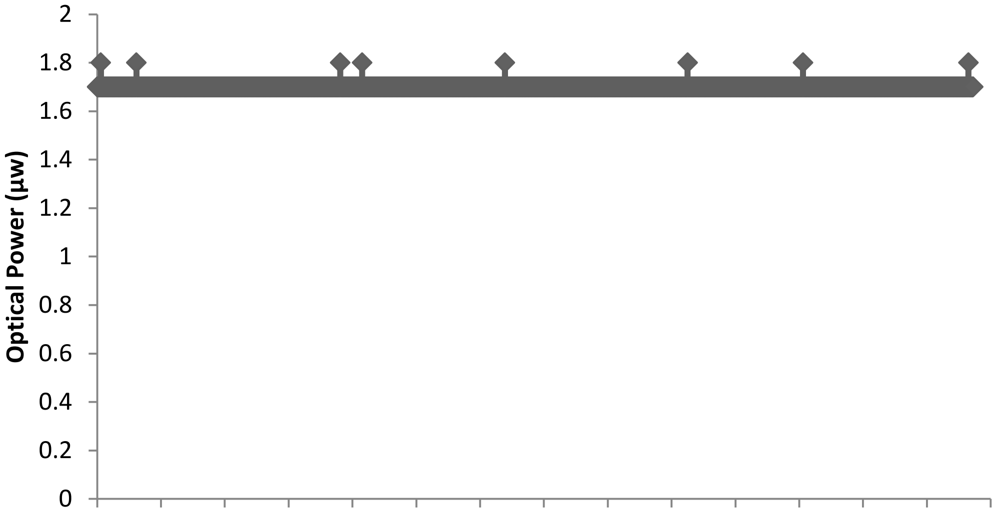

(a)

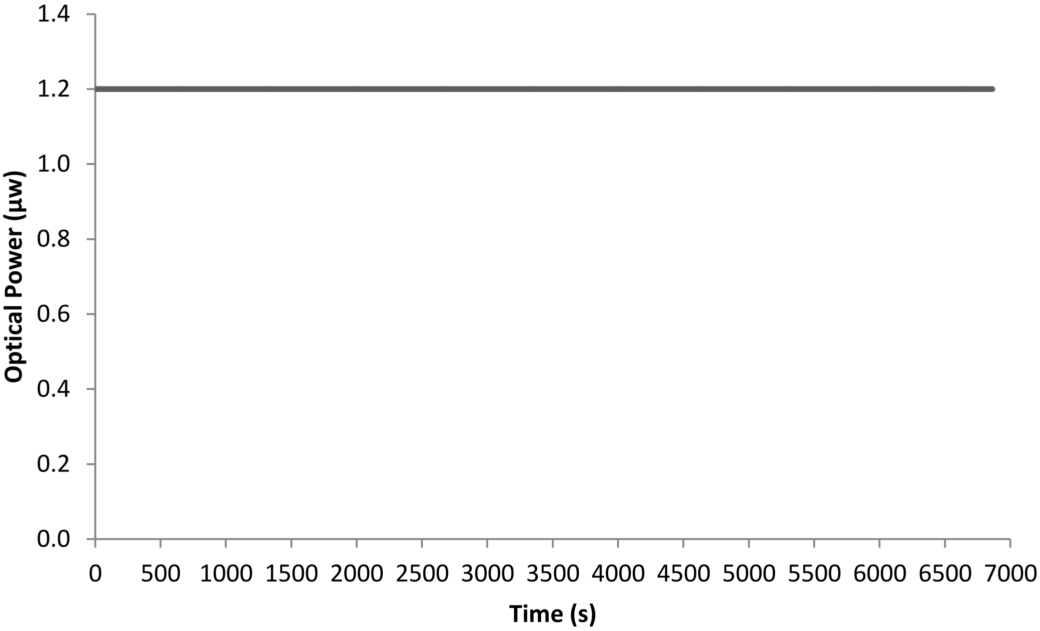
Optical Power (µw)
1.4
1.2
1.0
0.8
0.6
0.4
0.2
0.0
0
500
1000
1500
2000
2500
3000
3500
4000
4500
5000
5500
6000
6500
7000
Time (s)

(b)

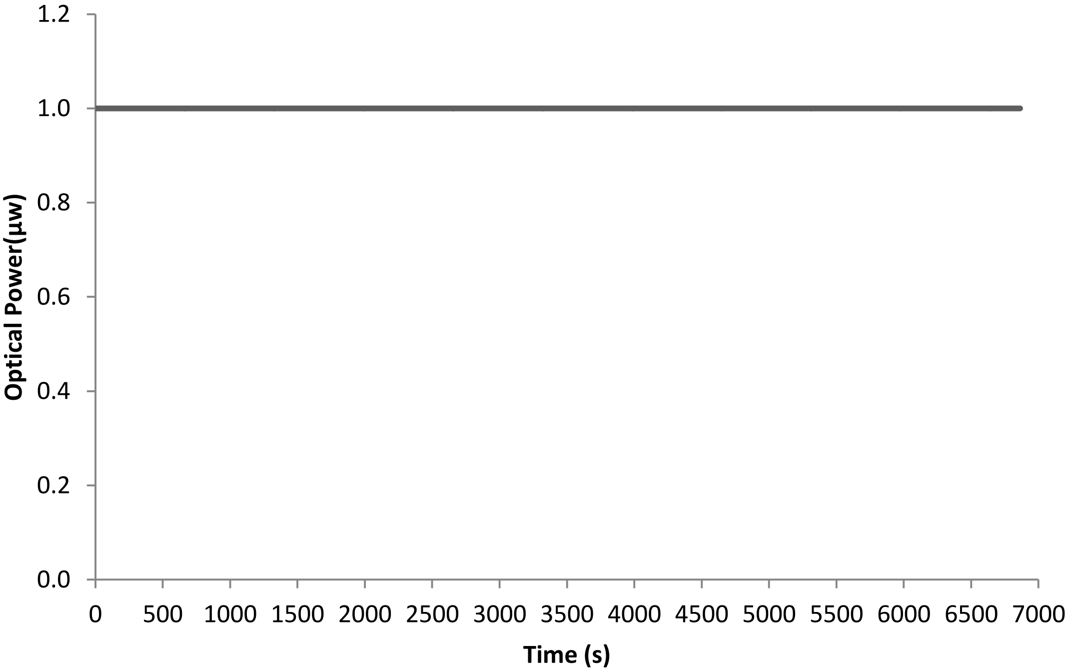
Optical Power(µw)
1.2
1.0
0.8
0.6
0.4
0.2
0.0
0
500
1000
1500
2000
2500
3000
3500
4000
4500
5000
5500
6000
6500
7000
Time (s)

(c)

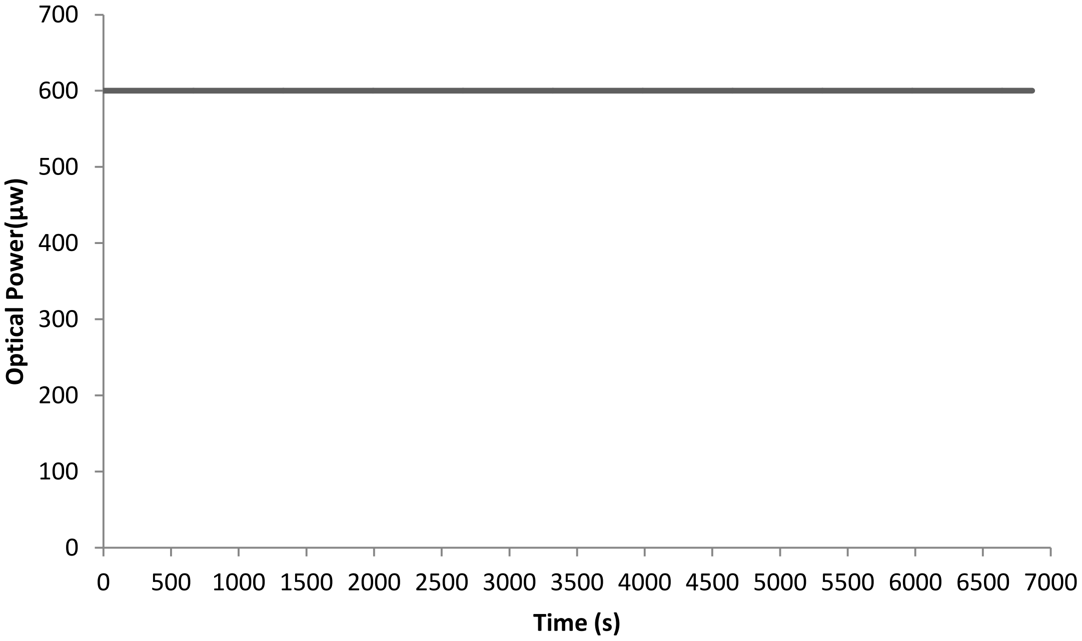

(d)

Figure 5.12 Time course of emitted optical power. (a) Green (b) Blue (c) Red and (d) Near Infrared

LED control software

The LED used for illuminating the fundus and the LEDs used for flicker the stimulation was controlled with software developed in Visual Basic. The block diagram of LED driving circuit is shown in Figure 5.5. Programmable microcontroller (PIC18F452, Microchip, USA) was used for timing and power control of the LEDs controlled by a personal computer. The circuit has been developed based on the specifications required by an ophthalmic reflectometer. The system was able to drive two LEDs with independent channels. The intensity of the optical power emitted by one of two LEDs modulated with square wave with frequency from 1 to 20 Hz, duty cycle and modulation depth between 0% and 100% and a variable current between 0 mA and 120 mA. The circuit was connected to the personal computer by a USB 2.0. The simplified layout of LED control unit was shown in Figure. 5.13.

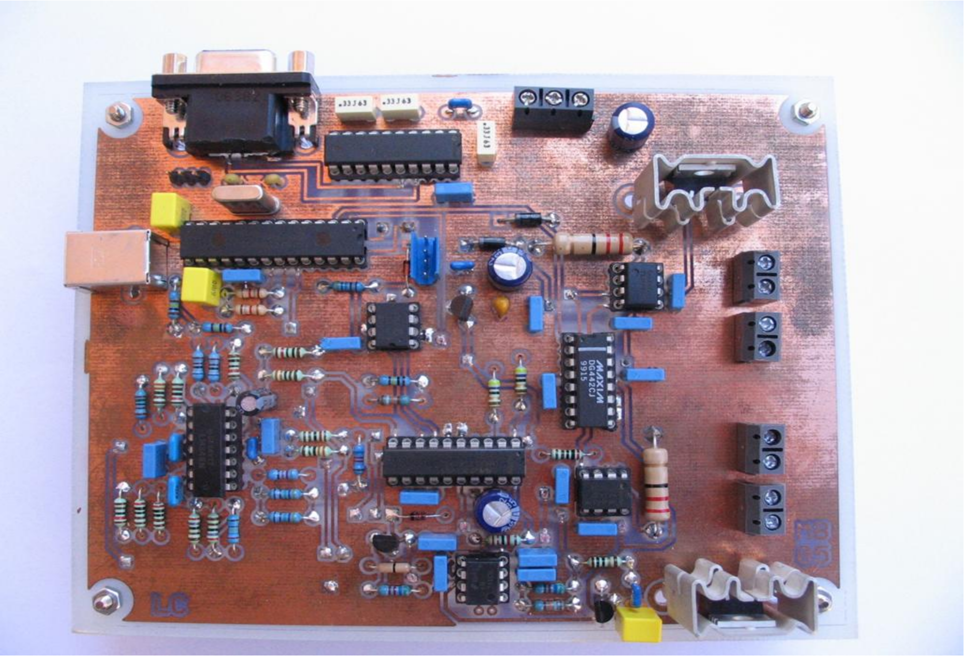

Figure 5.13 Board of the LED driving circuit

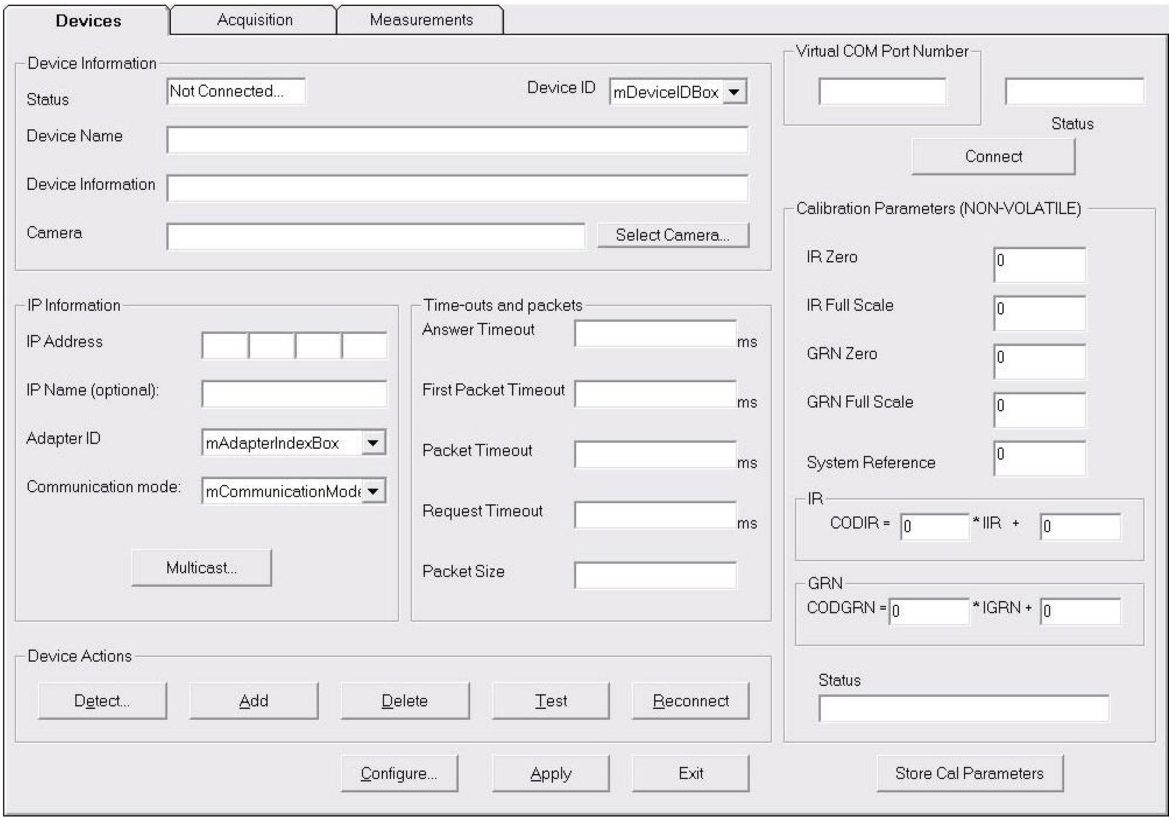

Status: Not Connected...

Device ID: mDeviceIDBox

Adapter ID: mAdapterIndexBox

Communication mode: mCommunicationMode

IR Zero: 0

IR Full Scale: 0

GRN Zero: 0

GRN Full Scale: 0

System Reference: 0

IR: CODIR = 0 * IIR + 0

GRN: CODGRN = 0 * IGRN + 0

Figure 5.14 Panel for setting the device parameters

Circuit description

The circuit is designed for biomedical applications, in particular for ophthalmology. In order to achieve high reliability, D/A converters are used to generate current for LED driver using reference voltages. The circuit is composed of a microcontroller with USB interface generates reference voltages for the entire circuit. A personal computer with USB interface is able to set the calibration parameters and operation of the circuit. The software interface of LED driving circuit and the personal computer is shown in Figure. 5.14.

Current Generators

As mentioned previously, the circuit is able to generate two independent currents in the range [0 mA, 120 mA]. In addition, one of two currents is modulated with a square wave and the frequency is set by the user through software. The basic circuit used for the current source is shown in Figure 5.15.

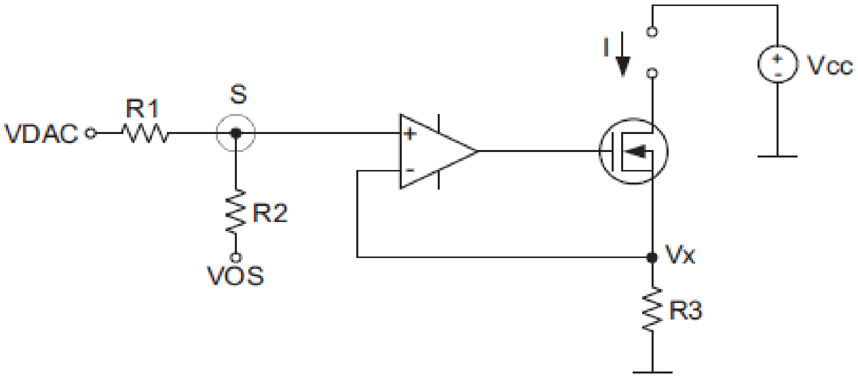

Figure 5.15 Basic current generator circuit

The constant current generator circuit uses an operational amplifier with an N-MOS transistor and the generated drain current is given by the equation 5.2.

$$I = \frac{Vx}{R_3} \tag{5.2}$$

The current gain of the BJT depends on the temperature and the performance of BJT's affected at high operating temperatures. However, the N-MOS having better temperature stability compared to BJT [122]. Infinite open loop gain of the operational amplifier the voltage at V_x is equal to the sum of voltage at point S. The voltage across the resistor R_3 is expressed as

$$Vx = VDAC\ \frac{R_2}{R_1+R_2} + VOS\frac{R_1}{R_1+R_2} \tag{5.3}$$

V_{OS} is the overall offset voltage of the circuit, which includes the offset voltage of the D/A converter and the operational amplifier and to set the null current at the output of the N-MOS drain when the applied voltage V_{DAC} is 0V.

$$I = \frac{Vx}{R_3} = \frac{1}{R_3}(VDAC\ \frac{R_2}{R_1+R_2} + VOS\frac{R_1}{R_1+R_2}) \tag{5.4}$$

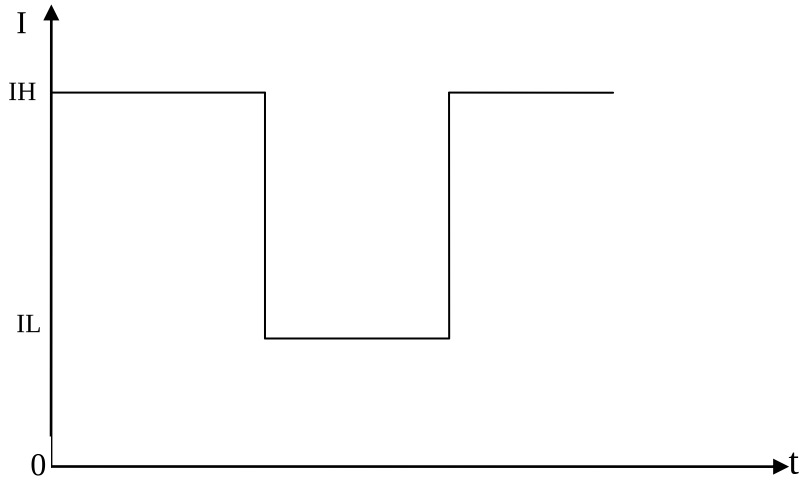

Figure 5.16 Modulation Depth

The circuit is designed to produce a maximum current of 120 mA. The devices selected for this circuit are IRF540 N-channel MOS (International Rectifier, USA) and an operational amplifier with high open loop gain in the order of 140dB (MAX427, Maxim, USA). However the channel 2 is able to produce a square wave output at a frequency between 1 to 20 Hz with a modulation depth between 0 and 100%. The modulation depth expressed as per equation 5.5 based on the Figure 5.16.

$$PMOD\ \% = 100\ \frac{I_H - I_L}{I_H} \tag{5.5}$$

The two level of the current for the channel 2 is generated using the circuit shown in Figure 5.17.

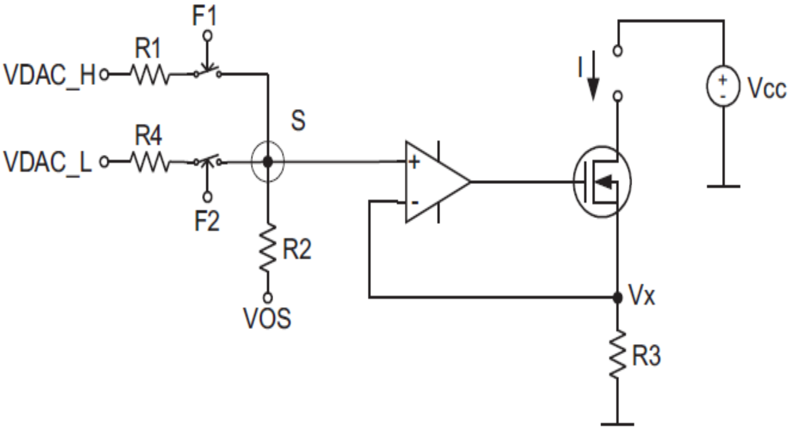

Figure 5.17 Current generator circuit for channel 2

The outputs from two D/A converters V_{DAC_H} and V_{DAC-L} are used to set the currents I_H and I_L respectively. V_{OS} allowed setting the effect of inaccuracies of D/A converters and operational amplifier. Two switches are used to select the input applied to the operational amplifier. Switching timing of the switches determine the duty cycle and frequency of channel 2. The duty cycle and the frequency of the channel 2 were controlled with software panel shown in Figure 5.18.

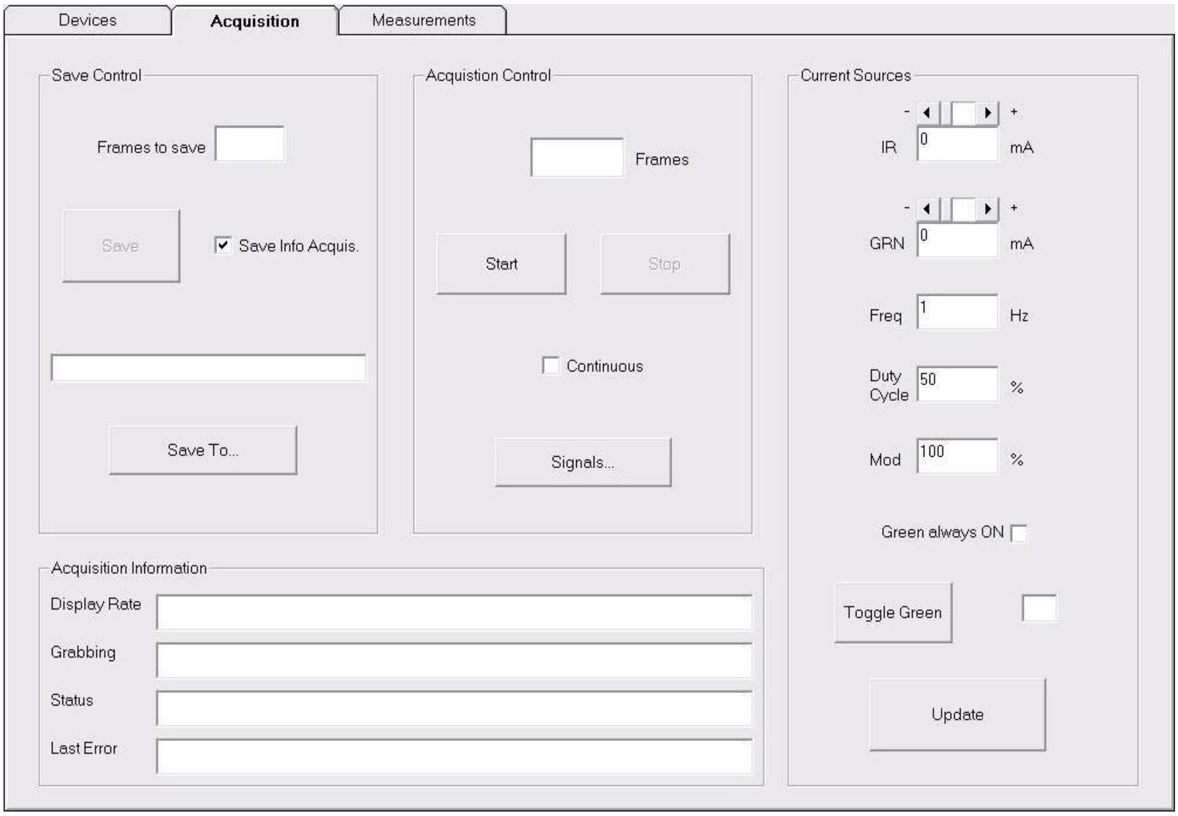

Frames to save
☑ Save Info Acquis.
Frames
☐ Continuous
IR 0 mA
GRN 0 mA
Freq 1 Hz
Duty Cycle 50 %
Mod 100 %
Green always ON ☐

Figure 5.18 LED controlled panel

Table 5.1 Frequency of the square wave generated by the channel 2

Theoretical frequency (Hz)	Measured frequency (Hz)
1	1.0
2	1.9
3	3.1
4	4.1
5	4.9
6	6.1
7	7.0
8	8.0
9	9.2
10	10.1
11	10.8
12	12.2

The frequency of the generated square wave from channel 2 using the software controlled setting was verified with a trans impedance photodiode amplifier (S1223, Hamamatsu, Japan) placed directly in front of the front lens of fundus camera connected to a Digital storage oscilloscope (DSO3102A, Agilent technologies, USA). The sample waveform acquired at 12 Hz was shown in Figure 5.19.

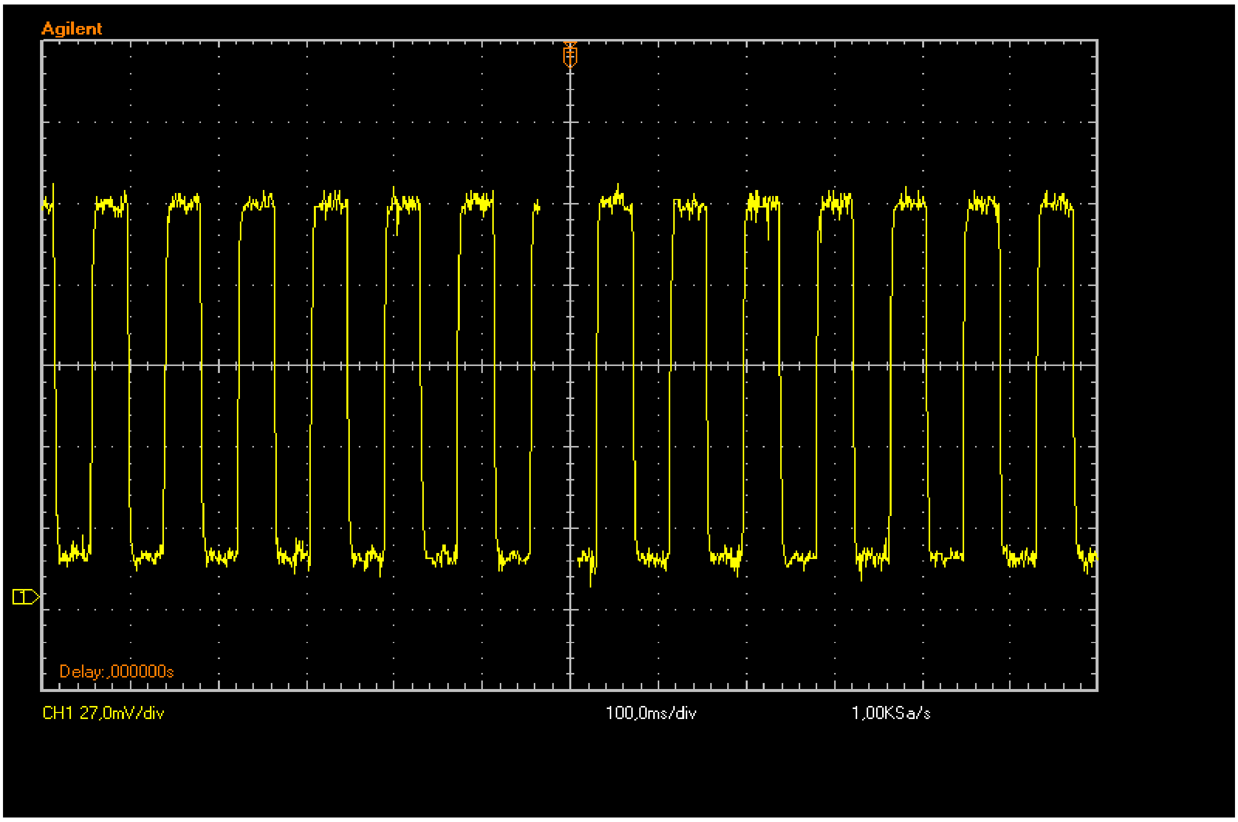

Figure 5.19 Sample square wave generated at 12 Hz

5.4 Image acquition system

The images are acquired with a help of standard frame grabber (iPORT-PT1000-ANL-2/6, Pleora technologies Inc, Canada). This device able to acquire images from multiple channels and sends images to the PC through a Gigabit Ethernet cable.

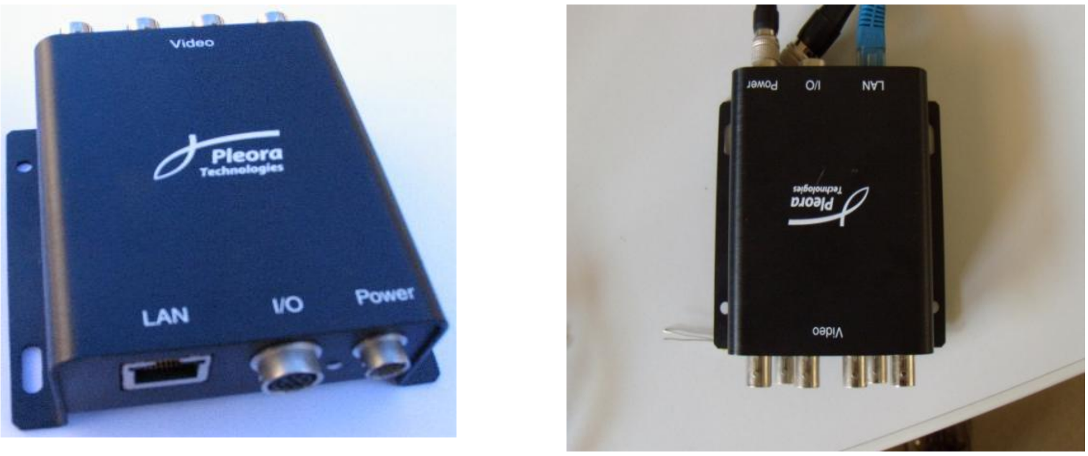

Figure 5.20 Picture of iPORT PT-1000 ANL-2/6 device

The frame grabber and the PC were connected through a Network Interface Card (NIC) mounted on the PCI slot of the PC. The iPORT High-Performance IP Device Driver runs on all Intel PRO/1000 network interface cards/chips (NICs), including those for PCI Express. Sometimes, the chip versions are called LANs-on-motherboard (LOMs). The driver streams IP image data directly into PC memory, allowing applications to grab image packets at rates upto 1 GB/s with minimal CPU utilization. The frame grabber is controlled thorough the software using PC. The iPORT IP engine is connected to a host PC either directly or through a network switch with an assigned IP address.

The iPORT device allowed inputting upto 6 video devices, however the ANL-2/6 only allowed 3 video inputs per channel. The device is able to grab 25 fps from each channel. When multiple video signals are present to the channel, the video output of the grabber is set through the application software running on the PC.

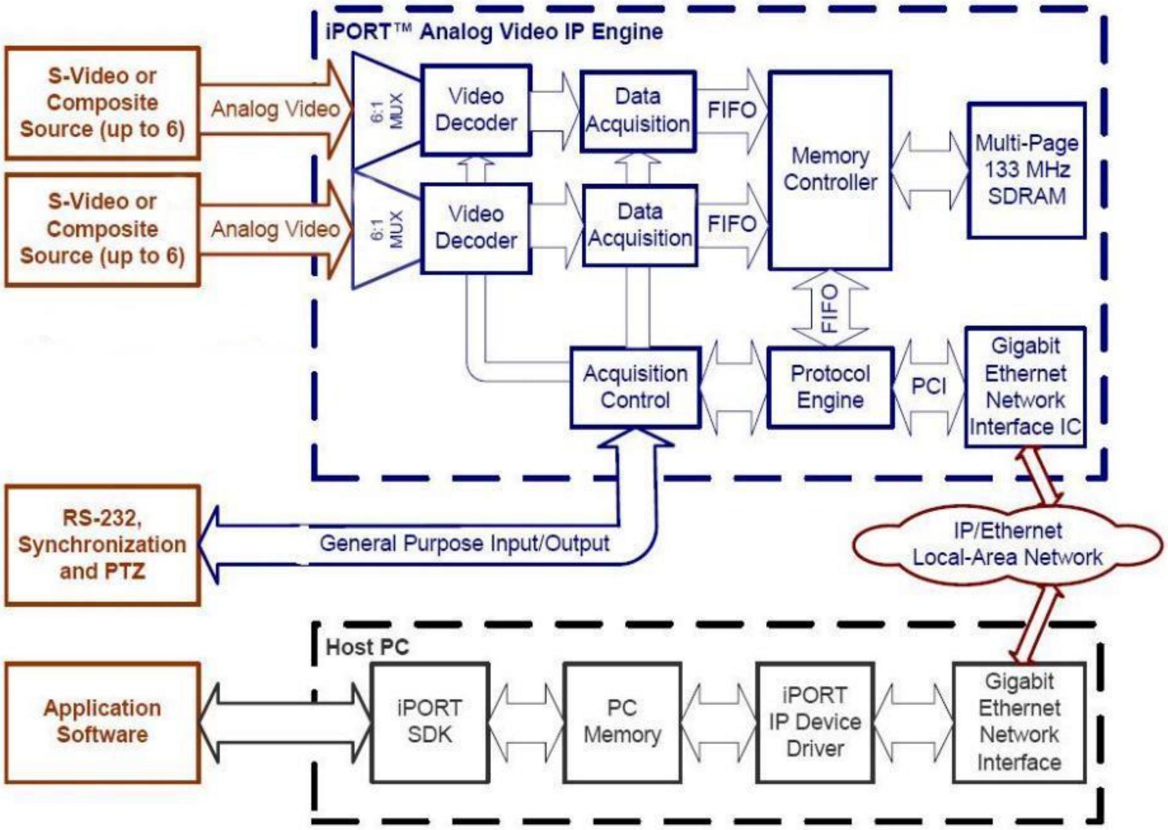

Figure 5.21 Block diagram of image acquisition system

The general purpose Input/Output connecter used to control the external devices connected to the iPORT device. The LED driving circuit was connected to the iPORT device through an RS232 connection and this circuit is controlled through software developed in Visual Basic.

The device is connected to the PC with help of modified software developed iPORT software development kit. The simple connect panel of the modified software is shown in Figure 5.22.

During the connection process an IP address was assigned to the IP engine. This IP address establishes the connection between the PC and IP engine over the gigabit Ethernet cable.

The PT1000 ANL-2/6 engine offers two channels. Each channel can grab simultaneously with independent settings. Application software allowed to grabbing and displaying images from both channels simultaneously. By selecting the Data Channel #0 and Data Channel #1, the images from both channels will be displayed in the same window as two sub-displays side by side. Figure 5.24 is a screen capture of the multiple channel display in one window.

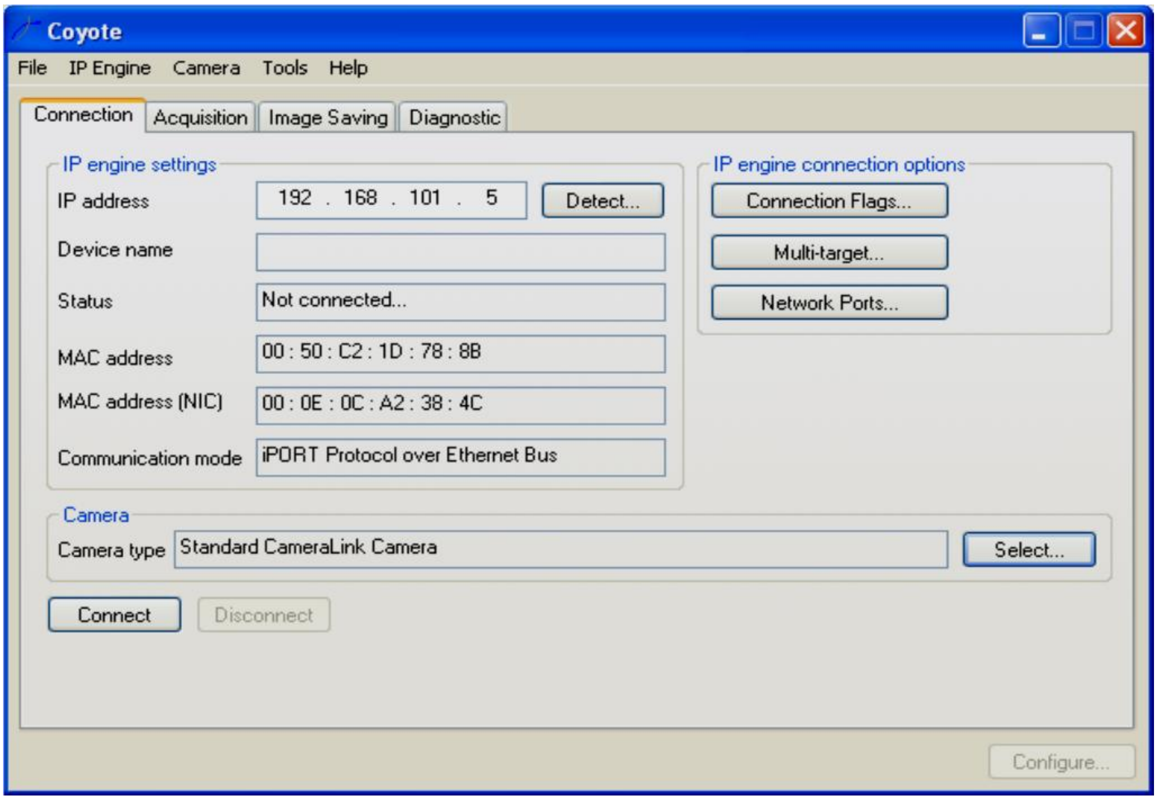

IP address 192 . 168 . 101 . 5

Device name

Status Not connected...

MAC address 00 : 50 : C2 : 1D : 78 : 8B

MAC address (NIC) 00 : 0E : 0C : A2 : 38 : 4C

Communication mode iPORT Protocol over Ethernet Bus

Camera type Standard CameraLink Camera

Figure 5.22 Connect panel of the frame grabber

Mode Grab - Continuous

Current channel Data Channel #0

Number of frames 1

Figure 5.23 Channel selection

The images captured from two channels at the same time and sent to the PC, stored in two different databases specified by the user during the image saving process. The images contain both the blurred and good images. The blurred images are removed before processing.

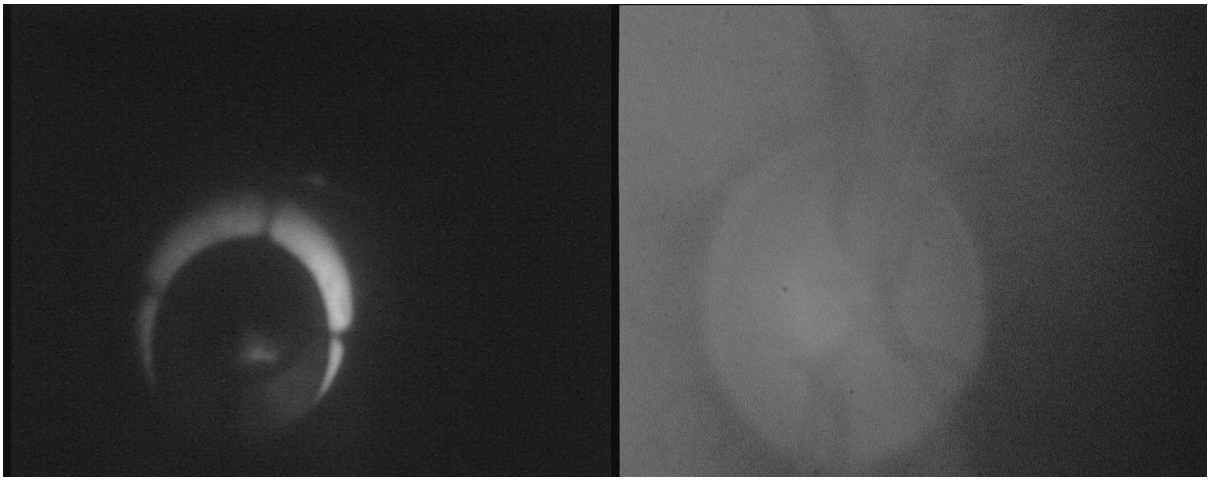

Figure 5.24 Images from two channels displayed in one window

5.5 Image processing algorithms

An image (Latin: imago) is two dimensional (photograph) or three dimensional (hologram) in nature to represent appearance of objects. The images can be captured by some optical devices like video camera, microscopes, lenses etc. These images may be classified as word images (graph, map), volatile images (CRT), still images (photographs) and moving images (film). Eye is the more sensitive part in human body. The interior part of the eye contains retina, optic disc, macula, fovea, capillaries, and vessels. These interior parts can be viewed through some specialist devices like fundus camera.

Functional imaging is a method of detecting or measuring the changes in blood flow, metabolism and absorption using probes to trace them within the human body. Ocular fundus reflectometry is a non-invasive technique to image the fundus and used to diagnose and document various eye diseases and their progression over time [123]. Ophthalmologist compares the retinal images of same eye by overlapping the fundus photography taken at different times. However these images are misaligned due to changes in optics between optics and fundus. This can occur within a time frame of microseconds. It is very difficult to compare manually all the images taken at different times. The computer based techniques produces more accurate information about the misalignment between images by superimposing two images.

Image registration aligns two or more images of similar objects taken at different times, from different viewpoints, and/or by different sensors. Previous investigators use several methods for analysing the fundus images. They are broadly classified into either interactive or automotive method based on the processing. Image registration is a very important task in all image analysis techniques. The registration of medical images is geometrically transforming them into their close similarity. An image similarity measurement quantifies the degree of similarity between intensity patterns in two images. The choice of an image similarity measurement depends on the nature of the images to be registered. Common examples of image similarity measurements include cross-correlation, mutual information, sum of squared intensity differences, and ratio image uniformity. Registration is intended to correct the relative translational shifts between the two images.

Image registration algorithms can be mainly classified into two types namely, intensity-based and feature-based [124]. One of the images is referred as reference or source and the other is referred as target or sensed. Image registration involves spatially transforming the target image to align with the reference image. Intensity-based methods compare intensity patterns in images through correlation metrics, while feature-based methods find correspondence between image features like points, lines, and contours. Intensity-based methods register entire images or sub-images. If sub-images are registered, centers of corresponding sub-images are treated as corresponding feature points. Feature-based method established correspondence between a numbers of points in images. After knowing the correspondence between a numbers of points in images, a transformation is determined to map the target image to the reference images, thereby establishing point-by point correspondence between images. Image registration algorithms can also be classified according to the transformation models used to relate the target image into the reference image. A spatial method mainly operates in image domain, matching intensity patterns or features in the images. Some of the feature matching algorithms are most similar in nature, based on performing manual image registration compared with traditional techniques. The corresponding control points (CPs) in the images are selected by an operator manually. When the number of control points exceeds the minimum requirement to define the appropriate transformation model, an iterative algorithm can be used to robustly estimate the parameters of a particular transformation type (e.g. affine) for registering the images [125]. When several source images are to be registered in the same target image, fundamental techniques need to be used repeatedly, once for each target image. The automatic subpixel registration algorithm minimizes the mean square intensity difference between source and target images [126].

5.5.1 Basic theory of image registration

The image registration is the process to estimate the transformation between two or more images and brought them to their close similarity. Registration algorithms compute set of image transformations between points or regions within images, or between physical space and images.

The registration problem can be mathematically represented as follows:

The main objective of the registration is to find the correspondence or mapping function C(.), which takes every pixel in the target image (Y_t) and return a pixel in the source (Y_S).

$$Y_s = C(Y_t) \tag{5.6}$$

Let the points in the source image, Y_S, be denoted by {Ysi|i = 1, . . . , m}, and the points in the target image, $Y_{t,}$, be denoted by {Ytj| j =1, . . . , n}. We want to find a transformation matrix C such that when applied to Y_S, the distance from each point on the resulting image and its corresponding point on the model image Y_t is zero in the noise free case.

Let us consider rigid registration without scaling, the transformation matrix C consists of two components: a rotation matrix R, and a translation vector T. The objective of registration is to determine R and T to minimize the following criteria

$$Y_s(R,T) = RY_t + T \tag{5.7}$$

When we add scaling factor the transformation matrix T is called the similarity transformation matrix. The new image will be similar to the original image but in a different scale. The minimization of the equation 5.7 is more difficult and highly nonlinear. The transformation matrix plays a vital role in image registration, when we know the transformation approximately, the registration process become more difficult. In most of the registration methods, an initial transformation is used in iterative process to obtain local minimum. The registration time also plays a role in most of the applications.

The image registration process used to obtain an optimum transformation matrix between source and target images. Rigid transformation is most commonly used method involves rotation and translation. In affine transformation parallel lines maps into parallel lines, however in projective transformation a line is mapped into a line. Elastic transformation maps a line into a curve. All the transformations are combinations of two or more transformations. The transformation is a global, if it is applied to entire image and when the transformation is local, if it will be applied to subsections of images. Rigid and affine transformations are global and elastic is local.

The mapping process may be interactive, automatic or semi-automatic. In interactive method a user will do all the operation with the help of software and in semi-automatic method some of the operations are performed in computer and in automatic method all the operations are performed automatically without any assistance of user.

5.5.2 Registration with image templates

Template matching method is based on cross correlation used in many applications of image processing. The template is sub-image from the reference image and considered as sensed image. The objective is to establish correspondence transformation mapping between sensed image and reference image. For high level accurate matching, the template should represent highly detailed and unique regions. The selection of best template is based on overlapping of templates produces less than 60% equal areas between two templates.

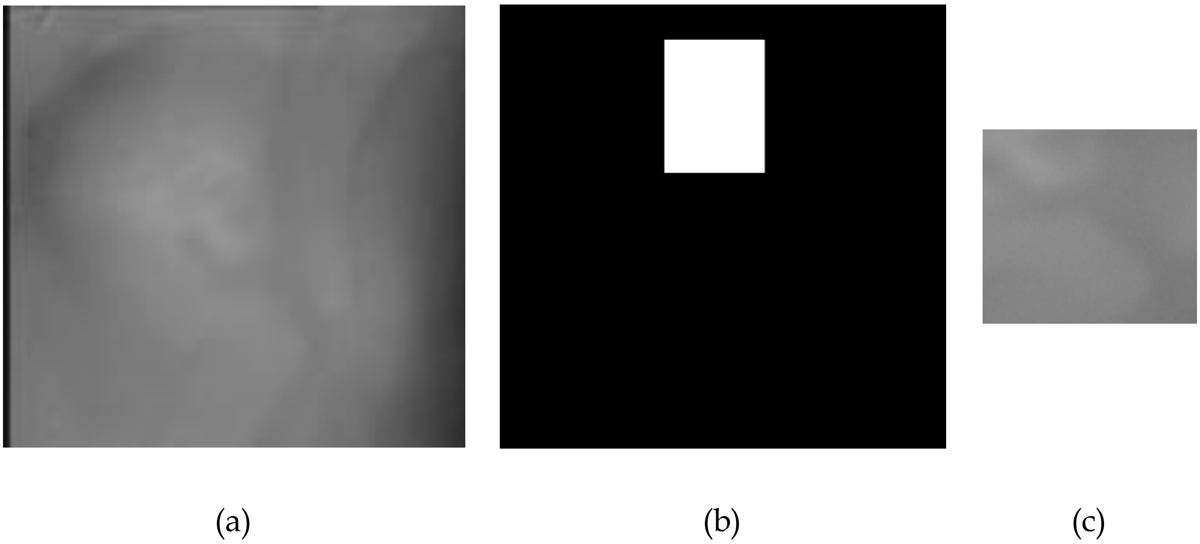
(a) (b) (c)

Fig. 5.25 Template matching method (a) target image (b) binary mask and(c) sub-image

The first step in template matching method is extraction of the sub-image. The sub-image is created using a 25 x 25 matrix based binary mask. The binary mask having the same size of the reference image containing only 0(zero) except the area of sub-image location. The location of the binary mask adjusted through a Matlab programme. This process is repeated by placing the mask on different places in the image. The templates are stored in a directory and the best templates are selected based on highest-gradient edges.

The uniqueness of each template is computed with same size window image in the neighbourhood using auto-correlation method [127]. The values of normalized 2D correlation coefficient were lies between -1.0 to +1.0. The template with sharp peak shows the uniqueness among the neighbouring windows. The other method used for testing the uniqueness is the eigan values method. We selected the unique template using first approach.

The second step in the image registration process is template matching. The template matching process used to find the location of the sub-image inside an image. The centers of the each template are used to extract the corresponding control points to determine the registration parameters.

The third step in this process is calculation of similarity measures. The similarity measure is process to compare the template with same size window image on the target to find the most similar image. The accuracy of the template matching method lies on the similarity between the widow and template.

We assumed a template image as T and the window image as S. The size of the template is 25 x 25 (n X n) and the size of window image is 640 x 480 (m X m). We generated the similarity images of size (616 x 456).

The sum of absolute differences in the intensity [128] was defined as

$$Sod(x,y) = \sum_{i=1}^{n} \sum_{j=1}^{n} [T(i.j) - S(x+i-1, y+j-1)] \tag{5.8}$$

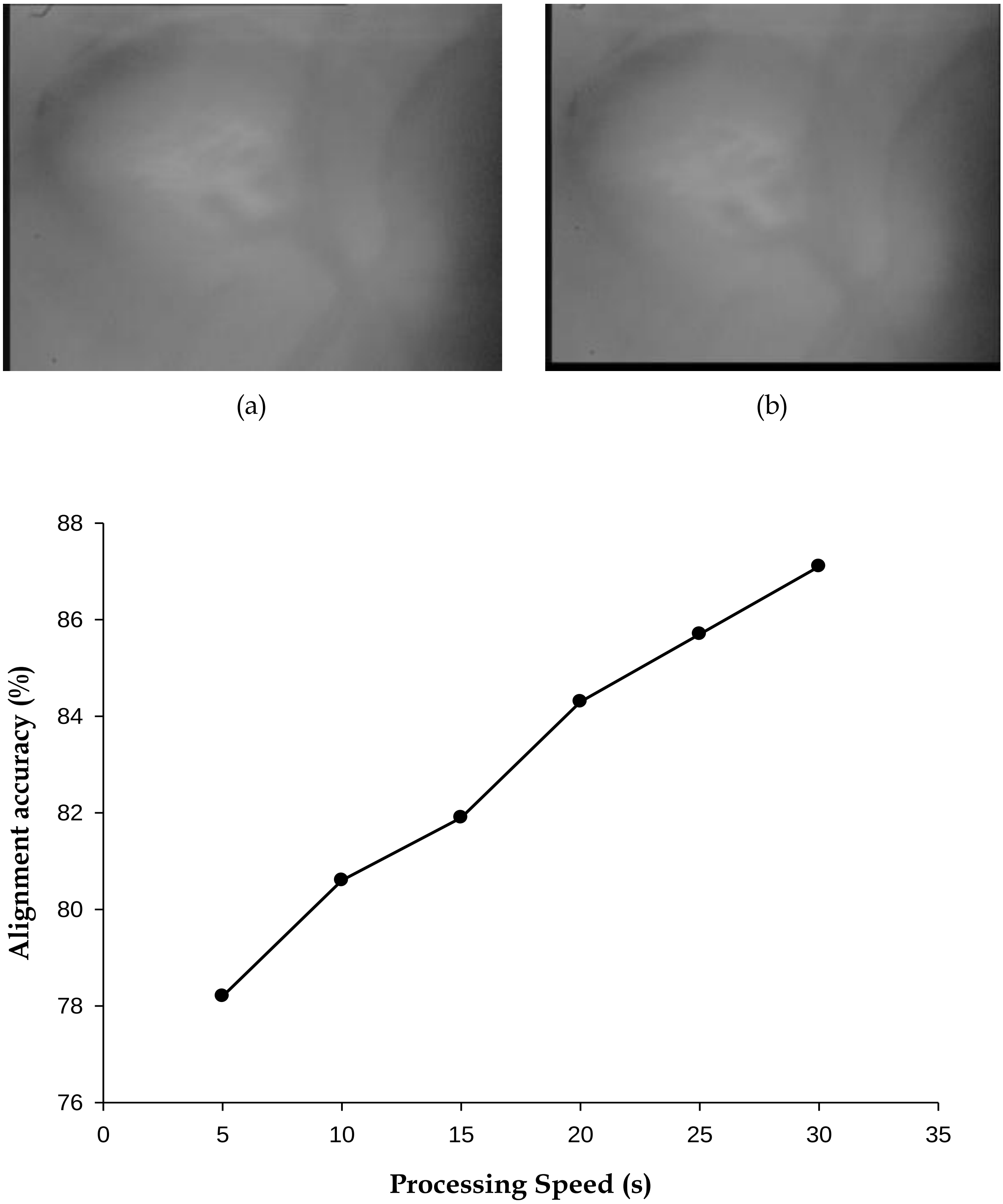

(a)

(b)

(c)

Fig. 5.26 Results of 2D template matching method (a) source image (b) aligned image and (c) alignment accuracy

Coordinates (x,y) represent the front-upper-left corner of a window in image S where the template being matched. Sod shows the dissimilarity between T and the window at location (x,y) in S. The similarity calculation takes large time and some researchers proposed new algorithms to speed up the computation [129].

The cross correlation gives similarity between the template and the window, if both are similar Sod(x,y) will larger and the mean will be zero, if both template and window are normalized. Once the best template and the location in the image identified, the translational shift between the template and the window can be calculated as

$$Trotation = [\cos(u) \quad \sin(u) \quad 0; -\sin(u) \quad \cos(u) \quad 0; \; 0 \quad 0 \quad 1] \tag{5.9}$$

$$Ttranslation = [1 \quad 0 \quad 0; \; 0 \quad 1 \quad 0; \; dx \quad dy \quad 1] \tag{5.10}$$

where u is the angle of rotation between template and the window and dx–translation in x direction, dy-translation in y direction. An affine transformation is applied to create 2D spatial transformation structure. The image S is transformed based on 2D spatial structure. The template matching method had highly complexity and takes larger time for computation.

5.5.3 Multiscale framework based image registration

Our main goal of the new algorithm design is to align the images at a faster rate. Image registration is the process of finding a mapping that aligns one image to another. The mapping functions between two images are defied in Equation 5.6.

We used two methods for establish the mapping function: warped grid and flow. The warped grid method takes a regular grid and uses the mapping C (.) to wrap it. In the flow approach maps a subset of discrete points with a translation vector. Figure 5.27 shows some examples of the grid and flow representations.

There are three main problems affect the registration of images, (i) distortion (ii) images acquired by different devices or same device with different settings (iii) only availability of partial data. Most of the registration algorithms are based on (1) estimation of transformation with some landmarks (2) geometric transformation (3) intensity changes (4) minimization of error metric.

Feature Space

Feature-based method extracts number of corresponding features like contours, edges between the pair of images to be registered [130]. Common futures include corresponding points [131], edges [132] or contours [133] and they are extracted manually or automatically. The advantages of feature-based method are less computational complexity. However, this approach is highly sensitive to extraction of the features. Also features may reduce the sensor noise. Intensity-based method estimate transformation between entire intensity images. This approach avoids the difficulties in the feature extraction stage.

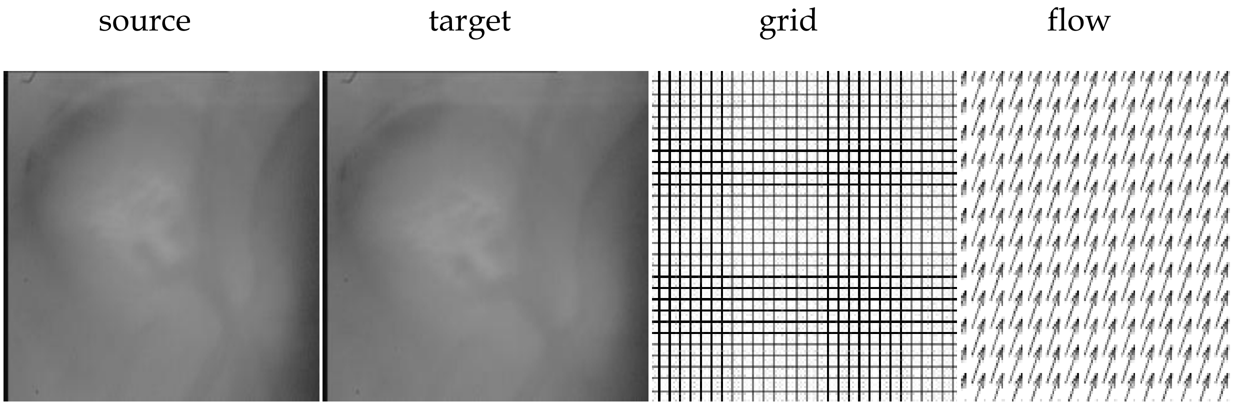
source target grid flow

Figure 5.27 Sample mapping of grid and flow mapping

Geometric transform

The geometric transform is most necessary model required; whether the model is based on feature or intensity based. The estimation of global rotation and translation for images are more difficult. The geometric transformation was defined with polynomials [134]. The major disadvantages of this approach are that estimation of higher-order polynomials leads to unstable transformation and computationally inefficient. The advantages of this method is able to model the highly nonlinear transformations

Intensity changes

The geometric transform is inefficient to estimate the transformation between two images with different intensity levels. Many registration algorithms use a pre-processing method to remove the intensity variations before registering the images. Simultaneous estimation intensity changes and geometric transformation is more difficult.

Estimation of error metric

After the transformation model is selected, the estimation of translation parameter begins. The next step is deriving the error metric estimation function between two images. Most commonly used method is mean square error (MSE), the mean difference in intensity or distance between two images [135]. Error metric calculation sometime uses the fast Fourier transform. The errors can be minimized using simple linear method called least square estimation and sometimes a non-linear estimation is also used.

We selected an intensity based approach to avoid the difficulties in selecting the features. We modelled the geometric transform with local affine. We employed MSE error metric function for the intensity values and minimized through least square estimation [136]. The proposed system stages was shown in Figure 5.28

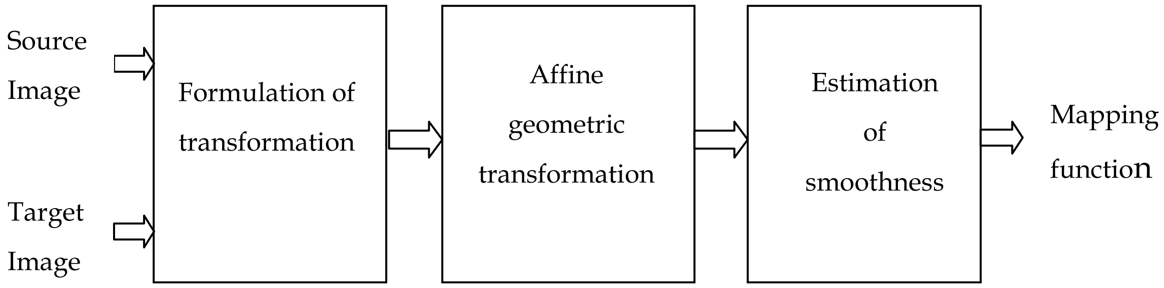

Figure 5.28 Schematic diagrams for differential multiscale framework

Methods

The image registrations between to images are formulated with a non-feature based differential framework. The formulation of motion estimation was obtained based on the descriptions found in [137-139] and modelled as affine transformation. We denote f(x,y,t) and f(x′,y′,t-1) are the source and target images respectively, where t denotes the temporal parameter. We assumed the intensity between two images is constant and the motion as locally affine model.

$$f(x,y,t) = f(m_1\,\mathrm{x} + \mathrm{m}_2\mathrm{y} + \mathrm{m}_5, m_3\,\mathrm{x} + \mathrm{m}_4\mathrm{y} + \mathrm{m}_6\,, \mathrm{t} - 1) \qquad (5.11)$$

where m_1,m_2,m_3,m_4 are the linear affine parameters and m_5, m_6 are translation parameters. In order to estimate these parameters a quadric function to be derived and minimized

$$E(\vec{m}) = \sum_{x,y\varepsilon\Omega}[f(x,y,t) - f(m_1\,\mathrm{x} + \mathrm{m}_2\mathrm{y} + \mathrm{m}_5, m_3\,\mathrm{x} + \mathrm{m}_4\mathrm{y} + \mathrm{m}_6\,, \mathrm{t} - 1)]^2 \qquad (5.12)$$

where $\vec{\mathrm{m}}$ = $(m_1, m_2, \ldots, m_6)^T$ and Ω are the small neighbourhood. Since the error function is a non-linear function, its value cannot be minimized analytically [140]. We assumed that the intensity between the source and the target images is unchanged; however it can be failed in some circumstances. In order to avoid such problem, we also incorporated the intensity variation correction within our developed model. We also assumed that the transformation as local affine within the small spatial regions. We approximate the error function using first order Taylor series expansion.

5.5.4 Proposed Software System Overview

A more accurate estimate of the error function was determined using Newton-Raphson iterative method. On each iteration, the estimated transformation is applied to the source image and the source image is warped to align with target image and a new transformation is estimated between warped image and target image. The final estimate of transformation of source image can be improved within ten iterations.

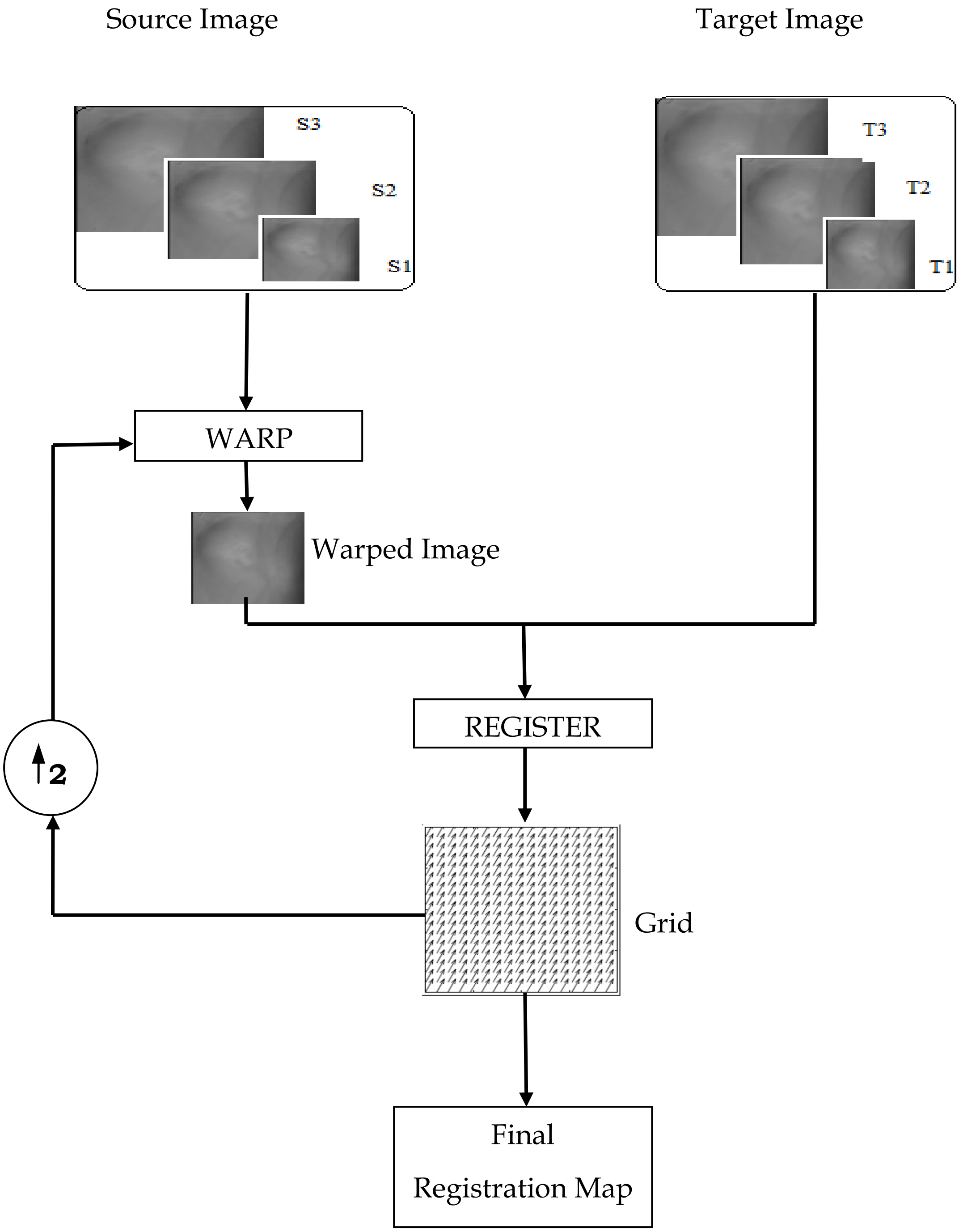

Figure 5.29 Multiscale estimation of the registration map from a coarse to fine scale

A Gaussian pyramid approach [141] is built for both source and target images at coarse level to estimate local affine parameters between the images. The estimated parameters are used at each level to warp the source image in the next level of the pyramid and this process is repeated at each level of pyramid. The estimated values are accumulated to obtain a single final transformation at the end. This estimation is used to warp the source image in the next level scaling. The warped image is registered with the target image. The multiscale estimation is used to recover all type of motions like rotation, translations etc. Within each scale, the registration map is generated in iteration fashion as shown in Figure 5.29

After an initial estimation of registration parameters minimum block size, sigma, edge mask and number of level, the source image is warped with these parameters and registered with the target image. During the computation of each iteration, successive registration maps are accumulated to form a single registration map. The iterations are stopped when the average displacement of motion is below 0.1 pixels.

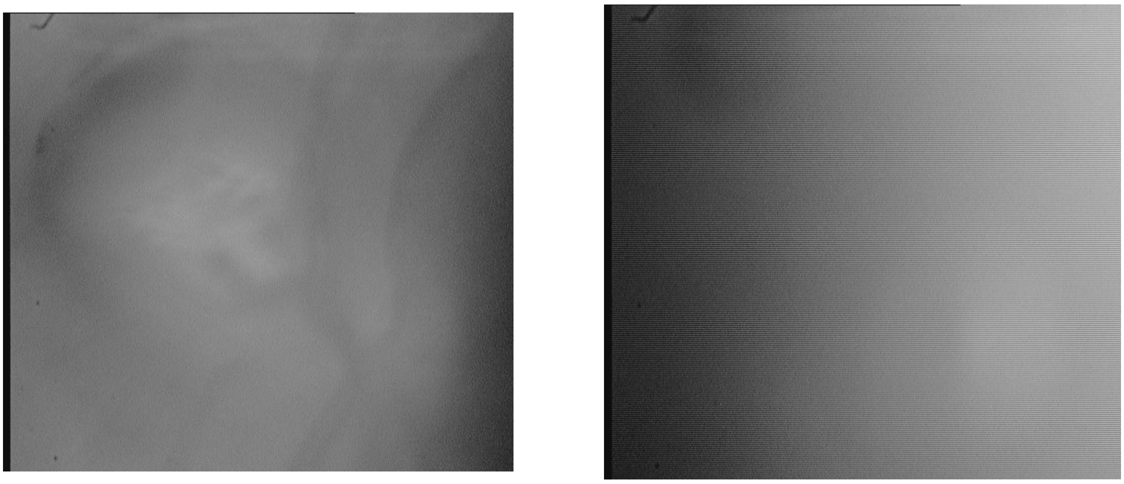

(a) (b)

Figure 5.30 Optic nerve images. (a) Well focused and (b) blurred or eye blinking image

Implementation

The gray scale ocular fundus images of size 640w x 480h-bitmaps (BMP are acquired with a CCD camera (Philips LDH0702, Germany) at a rate of approximately 25 frames-per-second. The images are captured by a frame grabber (iPOPT PT-1000, Pleora technologies, Canada) and send to the PC through a network cable and stored in the directory specified by the user. This data base contains a large amount of images, which also includes both good and out of focus images as shown in Figure 5.30.

Our images are well defined with the optic disk and optical nerves. The out of focus and eye blinking images (blurred) are removed from the data base before aligning the images. The separation of the images was done manually before; it required more computational time and a trained technician. To avoid the time consumption and manual error, the separation of the images is now done with the help of software developed using the maximum count algorithm.

The maximum count of an image is found through the pixel matching method, which maps the pixels (pixel to pixel) of the source and the target image. A critical threshold value is fixed (around 17000 for well focused optic nerve images) to separate the good and bad images. An image giving a count value above the threshold is designated as a good image and all the others are designated as bad images. This algorithm carries out the elimination of the out of focus images at a faster rate. Separation is obtaining by maximum pixel similarities between two images. Once the image is separated from the database, it is stored in a new database containing only the good images.

The translation shifts between the source and target images are corrected with template matching, which involves minimization of a function of the error between the search and reference images. In order to minimize the border effect, each image is padded with zeros to a size of 656 x 496. The computational complexity for the registration is reduced at a great level by the application of template matching techniques. The speed of registration is further increased by creating a small sub-image in the source and target to find the amount of translation and rotation involved between two images. Once these parameters are estimated, their values are applied to the whole image. One of the major difficulties with traditional image registration techniques is that they provide poor discrimination between objects of different shape but of similar size or energy content. Further, even though template-matching methods are effective in the presence of low or moderate additive noise, they perform poorly on images which are highly noisy.

The speed of alignment is further increased using differential multiscale framework. It is assumed that the difference between pair of images is due to motion (translations). A more generic affine model allows shear, rotation, scale and translation. We describe slightly modified version of generic affine model allows only translation. The affine parameters are estimated using differential framework using a Gaussian pyramid. A ten-level Gaussian pyramid is constructed for the source and target images. At each pyramid level, a single global affine and translation parameter is estimated as per Equation (5.11) with Ω, a correspondence mapping window is defined for the entire image as shown in Figure 5.31.

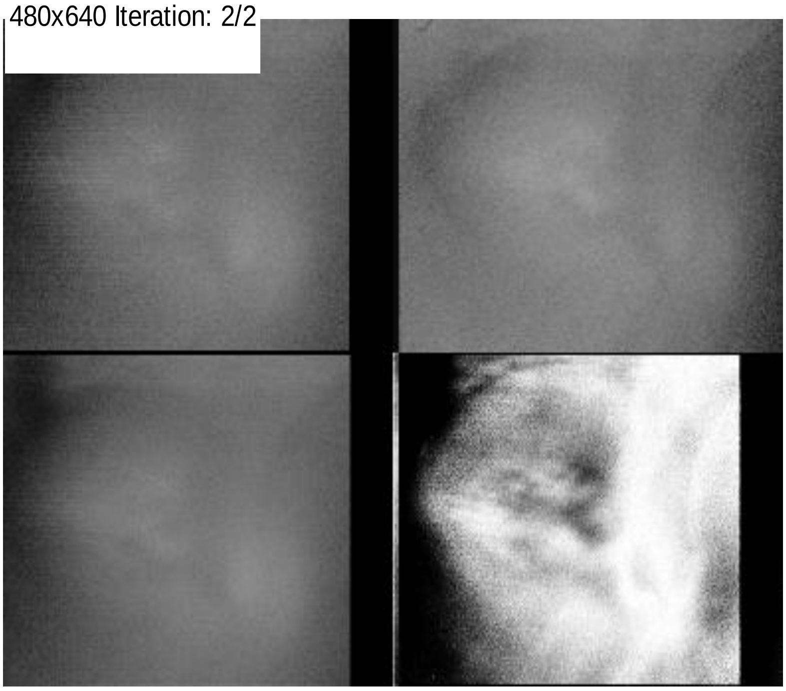

Figure 5.31 Correspondence mapping between source and target images: source image (Top Left), target image (Top Right), aligned image (Bottom Left), and correspondence map (Bottom Right)

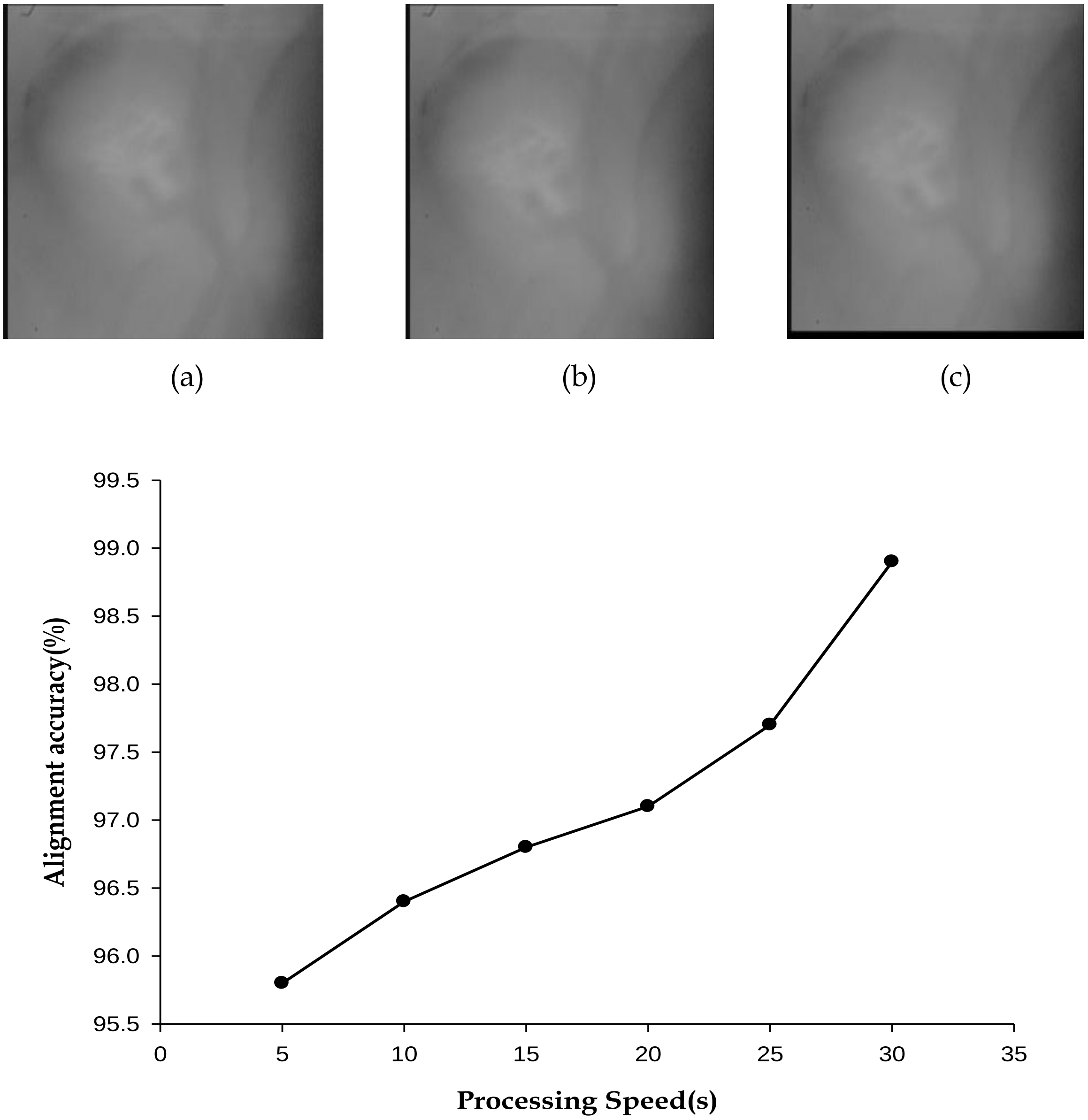

(a) (b) (c)

(d)

Figure 5.32 Results of Differential multiscale framework algorithm: (a) source image (b) target image (c) aligned image and (d) alignment accuracy

A coarse-to-fine method is used in order to contend the large motions. A Gaussian pyramid is built for both source and target images and the local affine parameter were estimated at the coarsest level. New parameter was estimated at each level of pyramid and used to warp the source image in the next level of pyramid. The spatial and temporal derivatives are estimated as follows. The images are first pre-filtered using a two-tap filter with coefficients [0.5 0.5]. The derivative in x is estimated by pre-filtering the result in y using a three tap filter with coefficients [0.2 0.5 0.2], followed by differentiating in x using a derivative filter [-0.4 0 0.4] and the same method was used to estimate the derivative of y. In order to minimize the error function an iterative method used. On each iteration, the estimated transformation is applied to the source image and a new transformation is estimated between the newly warped source image and the target image.

The registration map was estimated in an iterative fashion as shown in Figure 5.29. After an initial estimation of registration parameters, the source image is warped with the estimated parameters and registered again with the target image. During each of these iterations, successive intermediate maps are accumulated to form a single registration map. The iterations are stopped when the average displacement of the estimated motion is less than 0.1 pixels. The estimation of these model parameters is built upon a multiscale differential framework allowing to us capture small and large scale transformations. We have tested the efficiency of the algorithm by applying large number of ocular fundus images. The alignment accuracy of the algorithm is shown in Figure 5.32. Alignment accuracy has been calculated using sum of absolute differences of pixels between the aligned and target image. The time taken by an image for registration is represented as processing speed.

5.5.5 Discussions

We have developed two approaches for registering the fundus images. The template matching method had high computational complexity and less efficient compared to the multiscale differential framework method. The multiscale method is a fully automatic registration algorithm that uses gray levels of the images as features. We have introduced a new pyramidal approach to estimate the translational shift between the images. We have implemented this algorithm, presented with large amount fundus images; it shows a good performance with respect to accuracy and speed. This algorithm has both its strengths and weakness. It is very difficult to use images with large distortions. However, it is very useful in many medical imaging problems.

5.6 Camera movement calibration

CCD Video Cameras

The images are acquired using CCD video camera. One camera used to capture the images from the anterior segment of the human fundus (LDH0702/50, Philips, Holland) and the other camera used to capture images from the eye ball (KPC-E20B11, KT&C, South Korea). The images are formed on the camera based on the reflected light from the human eye. The reflected light contains both the near infrared and visible light from the LEDs. Both the cameras are set to work only on the near infrared light. The visible lights are filtered before the light striking the image sensor of the CCD. The image sensor used both cameras are 1/3" Sony high resolution HDD CCD with the effective pixels size of 752 (H) × 582 (V). However, the frame grabber is able to grab the image of size 640 (H) × 480 (V). The arrangement used for the filtering of the visible light is shown in Figure 5.3. An IR band pass filter F (RT-830, Edmund Optics, Germany) was introduced to filter out all the visible light going to the CCD camera used for acquiring the anterior segment image. Similarly along the path of the camera used to capture the eye ball images a cold mirror F (NT62-633, Edmund Optics, Germany) was introduced to filter out all visible light and followed by the filter an neutral density filter D (NT48-533, Edmund Optics, Germany) was used to reduced the amount of NIR light going to the CCD camera. The backscattered light from the front lens of the fundus camera makes the CCD saturation. We used a neutral density filter D (NT48-533, Edmund Optics, Germany) to reduce the amount of light passing to the CCD. The internal transmission for the filter was estimated using following equation

$$\tau_2(\lambda) = \tau_1(\lambda)^{\frac{t_2}{t_1}} \tag{5.13}$$

Where t_1- filter thickness of curve, t_2 – filter thickness of interest and $\tau_1(\lambda)$ – internal transmittance at t_1 of wavelength λ. The estimated optical density at 770 nm is 2.5 with a transmission of 16%.

Using Ocular eye model

We had developed software to estimate the translation shift and rotation in one camera image to estimate shifts in the other camera images. We estimated the translation shifts between two cameras using an ocular eye model mounted on a translation stage. The translation stage was moved in a known distance of 0.1 cm in X axis and images are acquired from both cameras. This was repeated until the translation shift of 1 cm in both sides from the center (left and right). The same is repeated on Y axis. The images acquired from the fundus camera are also influenced by some rotation. The angle of rotation was estimated using the ocular eye model by mounting the same on an angular rotation stage. The angular stage is rotated by an amount of 1° and the images are acquired similar to the translation in both X and Y directions. The eye ball images and anterior segment images are aligned using the Differential multiscale framework software described in section 5.5, taking the first image as the base image. Two dimensional cross correlations was used to estimate the pixel displacement between the original image and the aligned images. A calibration curve between the distance and the pixel displacement of eye ball images is shown in Figure 5.33.

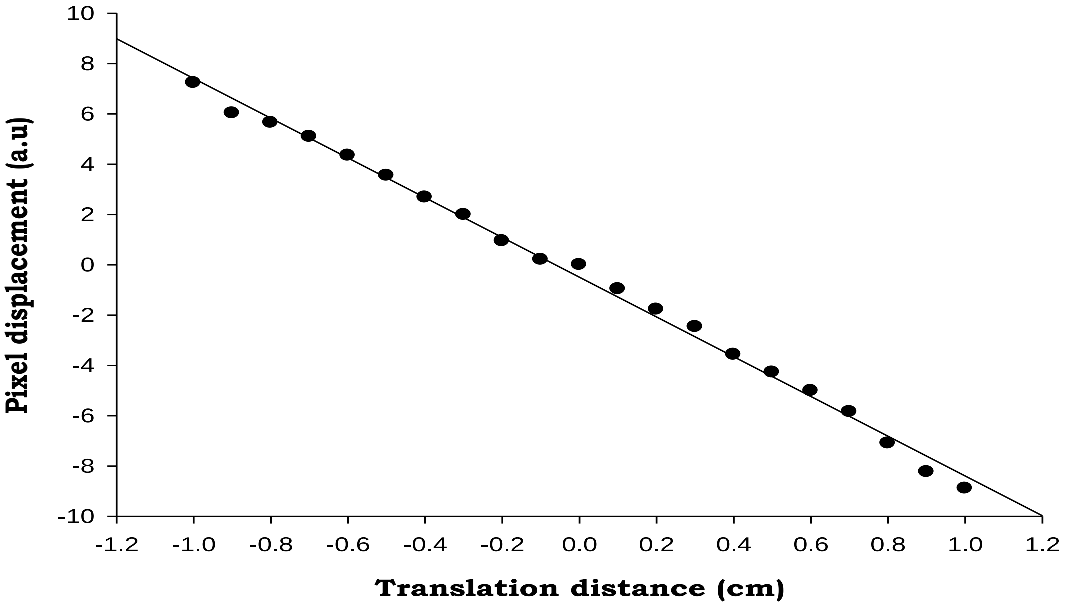

(a)

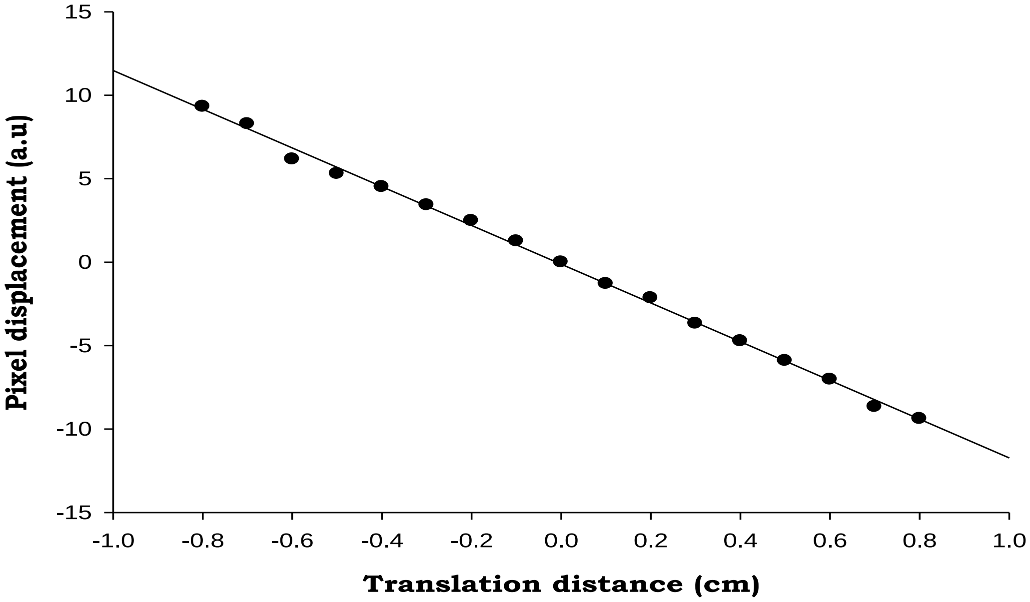
15
10
5
0
-5
-10
-15
-1.0
-0.8
-0.6
-0.4
-0.2
0.0
0.2
0.4
0.6
0.8
1.0
Pixel displacement (a.u)
Translation distance (cm)

(b)

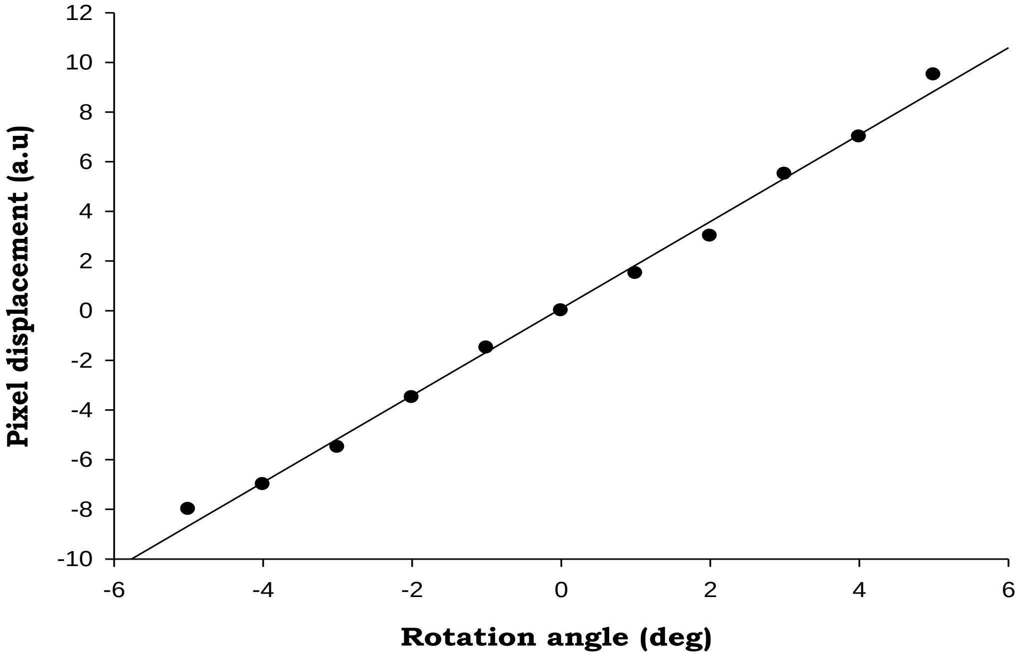
12
10
8
6
4
2
0
-2
-4
-6
-8
-10
-6
-4
-2
0
2
4
6
Pixel displacement (a.u)
Rotation angle (deg)

(c)

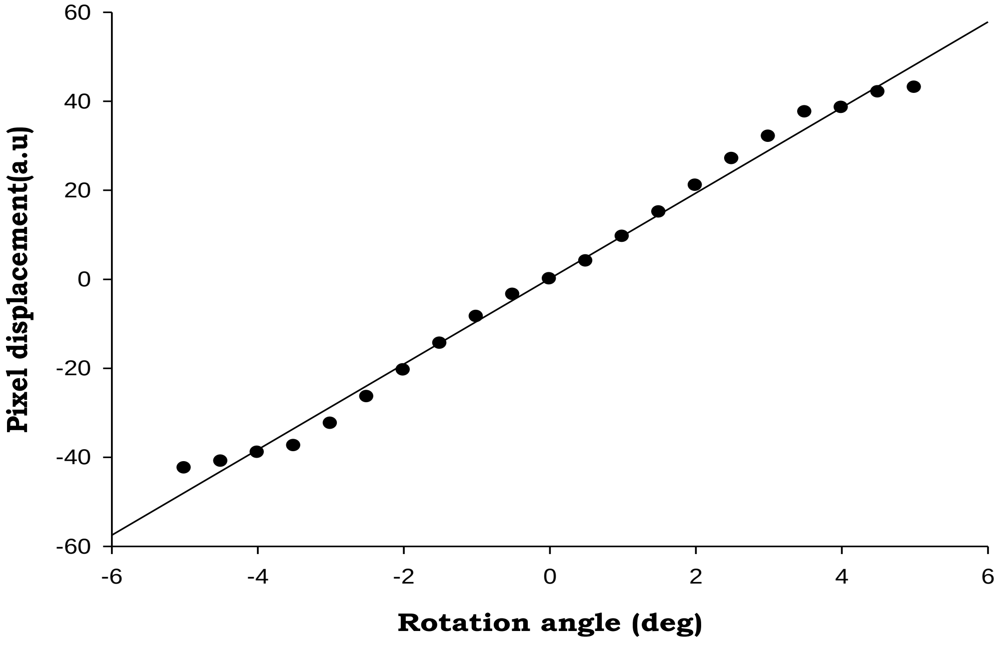

(d)

Figure 5.33 Calibration curves of ocular eye model. (a) Translation along X axis, (b) Translation along Y axis, (c) Rotation along x axis and (d) Rotation along Y axis

A relationship was established between the distance/angle and the estimated pixel displacement with a linear regression plot shown in Figure 5.33. The linear regression equations of translation and rotation are

$$T_x = -7.902\,D_x - 0.496 \tag{5.14}$$

$$T_y = -11.608\,D_y - 0.125 \tag{5.15}$$

$$R_x = 1.751\,R_{\theta x} + 0.091 \tag{5.16}$$

$$R_y = 9.609\,R_{\theta y} + 0.167 \tag{5.17}$$

where T_x, T_y are the estimated translation shifts and R_x, R_y are the estimated angle of rotation in x,y direction. D_x, D_y are the known translation distance and $R_{\theta x}$, $R_{\theta y}$ are the known angle of rotation.

The linear regression equations of anterior segment camera was estimated similar to the eye ball image camera, the linear regression equations of translation and rotation are

$$T_x = 12.097\, D_x - 0.103 \tag{5.18}$$

$$T_y = -9.984\, D_y - 0.489 \tag{5.19}$$

$$R_x = 6.777\, R_{\theta x} + 0.682 \tag{5.20}$$

$$R_y = 10.787\, R_{\theta y} + 0.381 \tag{5.21}$$

The relationships between two cameras are estimated using the equations from 5.14 to 5.21.

Calibration using human eye images

The orientation and the optical properties of human eye are different from the ocular eye model. The alignment based on the calibration curve of the ocular eye model shows much deviation with the software alignment. The camera movement between the anterior segment images and eye ball images are obtained as described below.

The experimental protocol is described about the stimulation of fundus. A steady near infrared light (770 nm, 600 µw at the cornea) was used to illuminate the fundus. The fundus flicker was obtained using Red, Green and Blue LEDs, one colour LED used at a time to flicker the fundus selected using a rotary switch. The intensity of the fundus illumination and flicker stimulation was controlled with the software panel described in the section 5.3.

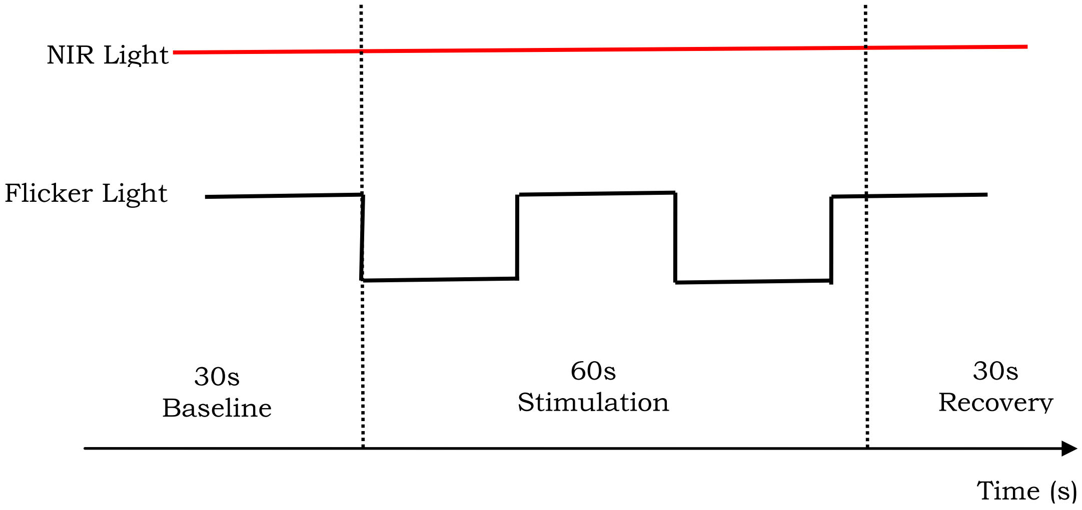

Figure 5.34 Measurement protocol

The measurement protocol shown in Figure 5.34, reflectance registrations at 770 nm, each consisting of 30s baseline followed by 60s stimulation and 30s recovery. Both cameras are synchronized to acquire images at the same time and set to store the images into two different directories specified by the user. The pre-processing of images like the removal of eye blink and blurred images in both directories as described in section 5.5. The images of both cameras are aligned separately taking the first image as target using the differential multiscale framework based image registration software descried in section 5.5. The pixel displacements of all the images are calculated using two dimensional cross correlations. Mean displacement in X and Y directions are estimated, the larger displacement from the mean on both sides are removed (corresponding images in both directories are also removed). Calibration curve obtained by plotting a linear regression line with the displacement of external pupil images Vs the fundus images for both X and Y directions.

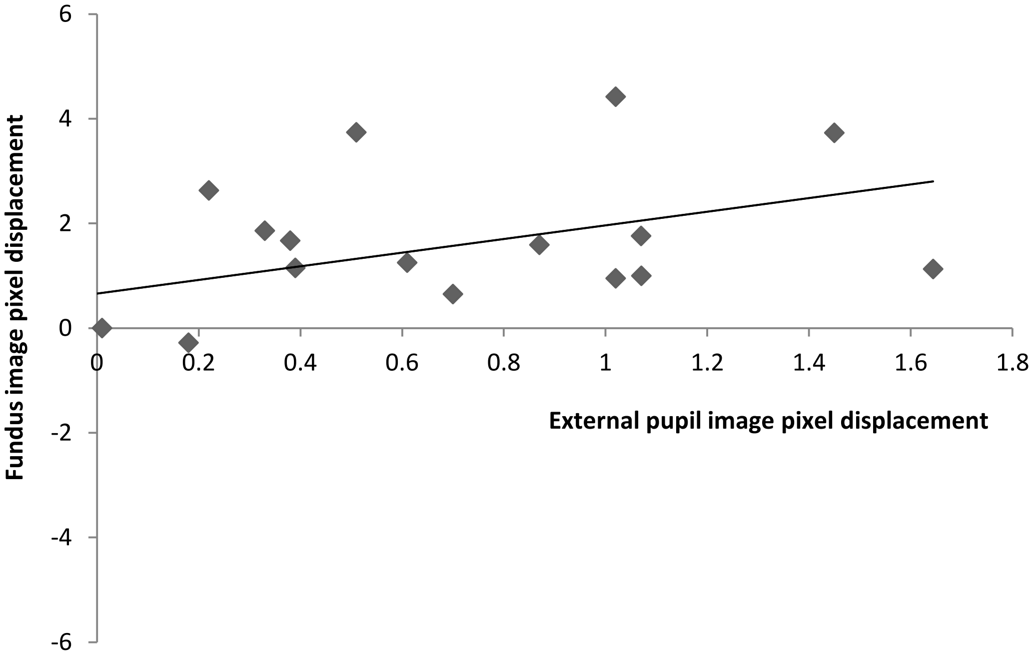

(a)

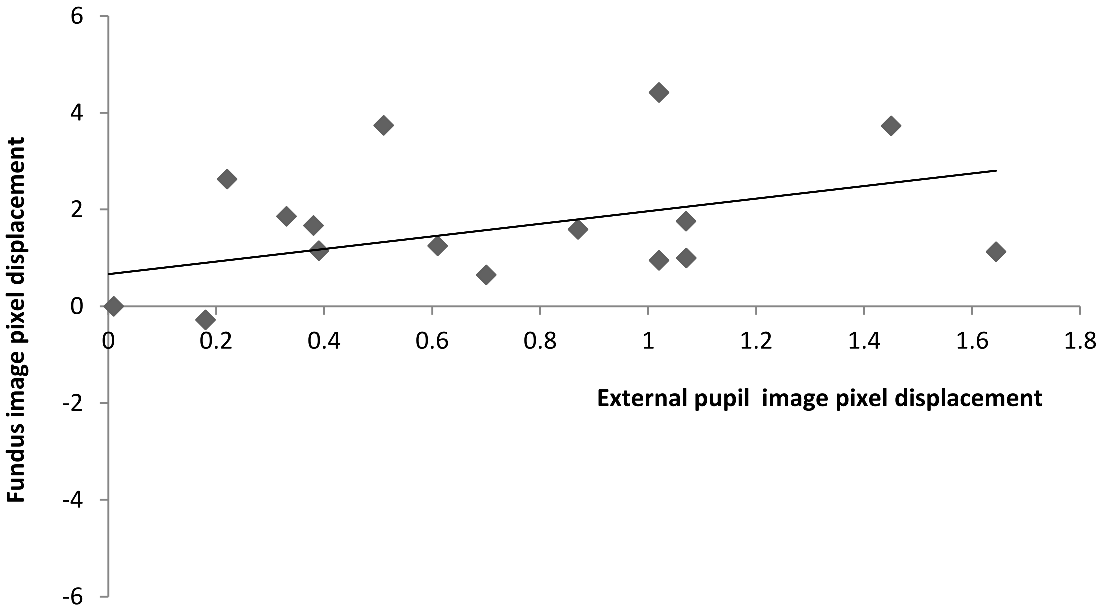

(b)

Figure 5.35 Calibration curves of human eye images. (a) X direction displacement and (b) Y direction displacement

The estimated translation shift between two cameras are given by

$$T_x = 1.301\, D_x + 0.662 \tag{5.22}$$

$$T_y = 1.367\, D_y + 1.008 \tag{5.23}$$

Where T_x, T_y are the estimated pixel displacement of fundus images (X and Y directions) corresponds to the pixel displacement of external eye ball images D_x, D_y respectively. The alignment precision was improved much better compared to the previous approach and the difference between the software based approach and linear regression based approach is below 1%.

5.7 Experimental results

Detailed explanations of all procedures were provided and informed consent was obtained from each subject prior to participation in the study. All the measurement sessions are performed under same condition. In particular the optical powers are kept below limits imposed for ocular safety [29]. The LEDs L1 (770 nm) and L2

(430nm, 523nm and 572nm) are kept the minimum required power to illuminate and stimulus the fundus. The optical power of LED used to illuminate the fundus was kept at 700 μW. The intensity of flicker LEDs (Red, Green and Blue) are kept at 7 lx. The optical power delivered by the LED L1 at the cornea was measured with help of optical power meter (Ophir Optronics, Israel). The optical intensity of the flicker light was measured using a lux meter (Detla ohm, Italy). The measurements were performed according to the measurement protocol. This protocol gives the duration of baseline, flicker and recovery and the modulation frequency of the flicker light. During the baseline a steady lights of LEDs L1 and L2 are applied to the human eye. During the flicker the modulated light of L2 and steady light of L1 was applied and in the recovery period is similar to the baseline condition. A sample measurement protocol of the reflectance measurement was shown in Figure 5.34.

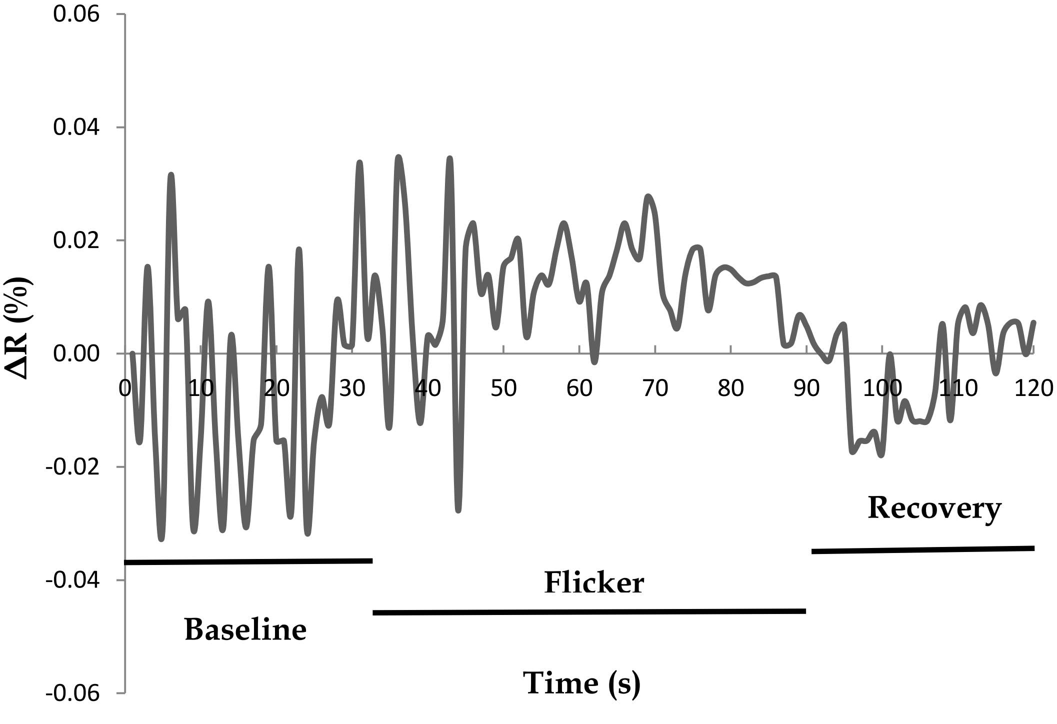

Figure 5.36 Changes in reflectance measured in ocular eye model

An ocular eye model (OEMI-7, Ocular imaging eye model, Ocular instruments, USA) was used to test the reflectance changes induced by the instrument. The percentage changes in reflectance were shown in Figure 5.36. The standard deviation of reflectance variation is 0.015%.

During the in-vivo measurement, the eye was dilated using two drop of 1% Tropicamide. The room was kept under dark condition during the entire measurement. The measurements were performed as per the protocol specified previously by making the visual stimulation frequency in the range between 8 Hz and 24 Hz. The studies performed using laser Doppler flowmetry (LDF) on optic nerve head blood flow (ONH) shows significant response in this frequency range [117]. The changes in reflectance were described interms of variation in the distribution of intensity changes of the pixel in the fundus images. The percentage change in reflectance R was described as

$$\Delta R\ (\%) = \left(\frac{R_{Fi}-R_{Bi}}{R_{Bi}}\right) \times 100 \tag{5.24}$$

Where R_{Bi} is the average response of first frame of baseline at site i and R_{Fi} is the response, averaged over the time slots of 1s, during next frames (baseline, flicker and recovery) at site i.

We performed series of in-vivo measurements to test the functionality of the instrument. The duration of the baseline is been set to a value of 20s, flicker is been set to a value of 60s and recovery is been set to a value of 30s with modulating frequency of 12 Hz at 523 nm. The images are acquired at a rate of 25 frames per second. The images of aligned with the software. The large movement images are removed from the database before calculating the reflectance variation. The pixel displacements of all images are calculated using 2D image correlation method. We estimated the linear regression equation for the displacements between two camera images as described previously. The region of interest was selected in all images acquired during baseline, flicker and recovery with an area of 25 × 25 pixels. The sample image with region of interest is shown in Figure 5.37.

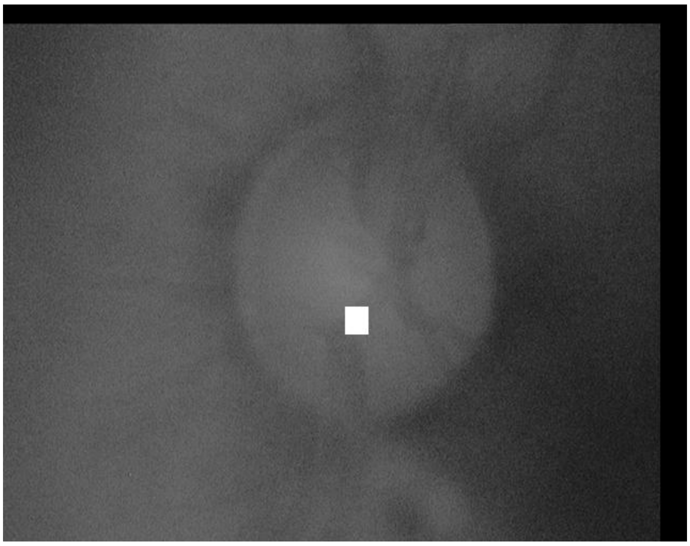

Figure 5.37 Region of interest for the study

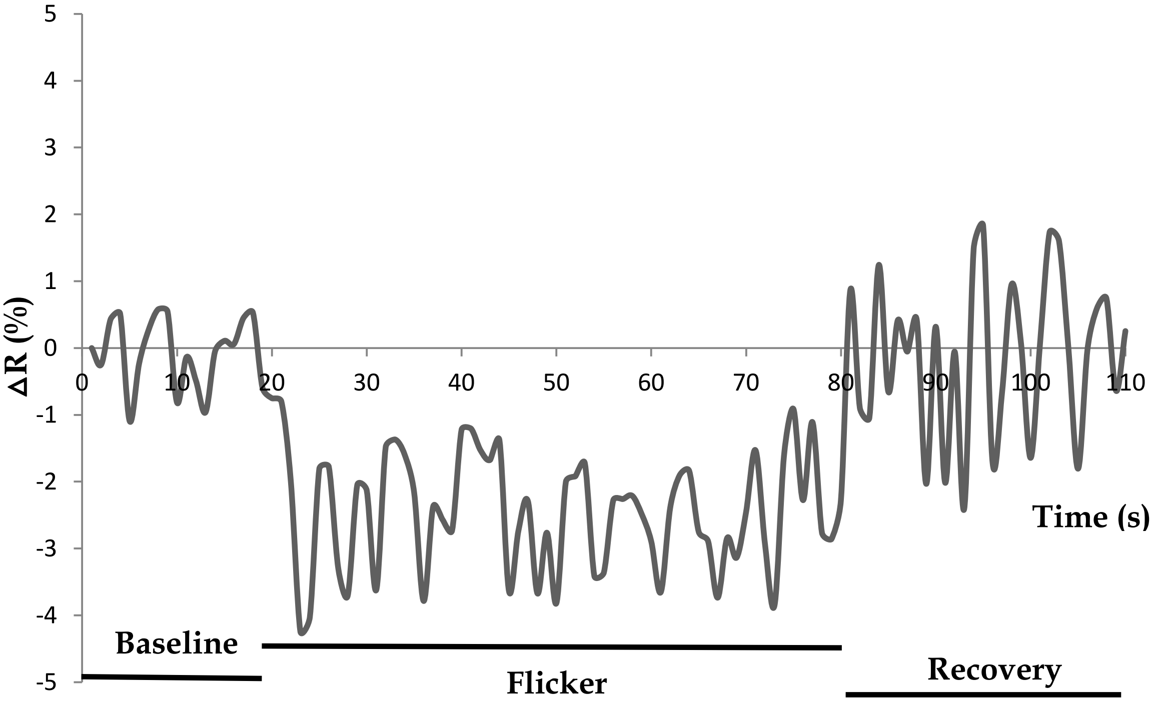

Figure 5.38 Reflectance variation of the region of interest

The mean pixel value in the selected area (region of interest) of all images is estimated. The average intensity variation of each frames are calculated by averaging all the images in that frame. The percentage change in reflectance of the region of interest is calculated using the equation 5.24 taking average intensity of the first frame in baseline image as R_B and R_F is the average intensities of next frame images in the baseline, flicker and in the recovery periods at the given region of interest site. The reflectance variation of the region of interest at 12 Hz with 523 nm was shown in Figure 5.38.

Reflectance measurement with different modulating frequencies

Preliminary in-vivo measurements have been performed on a 25 years old male subject. Informed consent was obtained from the subject. The pupil of the examined eye was fully dilated with help two drops of 1% tropicamide atleast 20 min before the examination. The instrument was placed in a dark environment and separated from the light of the monitor of the personal computer. Images of the ocular fundus and the external eye ball were acquired by setting the NIR power impinging the subject cornea to 600 μW. The intensities of the visual stimulation LEDs are settled at 6 lx by adjusting the current applied to the LEDs. Flicker stimulation was generated by modulating a steady illumination (light at 430, 523 and 572 nm) at frequencies of 4 Hz, 12 Hz and 14 Hz using software controlled driver circuit. The observation angle was approximately 45°. Each set of measurements were performed at different modulating frequencies with same modulating light. The measurement protocol was set as 60s baseline followed by 60s flicker and 60s recovery for all measurements. Both cameras are synchronised with software to acquire the images at the same time. The images are stored directly in the personal computer in different folders as specified by the operator. The blurred and eye blinking images in both camera folders are removed using the software before image alignment. The images are aligned with the software described in section 5.5. The aligned image of anterior segment camera is shown in Figure 5.39. The pixel displacements of all external eye images are estimated using two dimensional cross correlation method. The time sequences of both camera acquisitions are estimated to relate one camera image with the other camera image and the mismatch images are removed in both databases.

The pixel displacement of the eye ball images are used to estimate the movement of the anterior segment images using the calibration characteristics of human eye described in section 5.6.

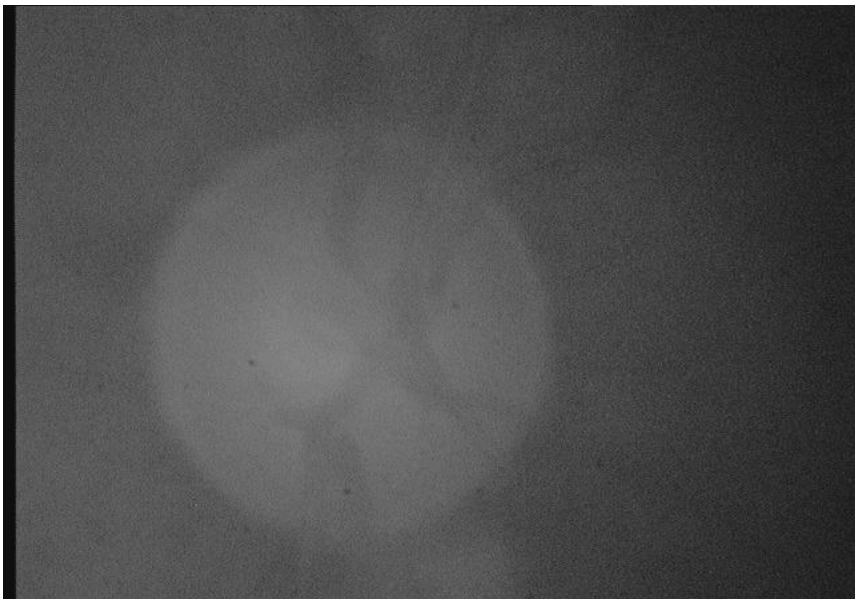

(a)

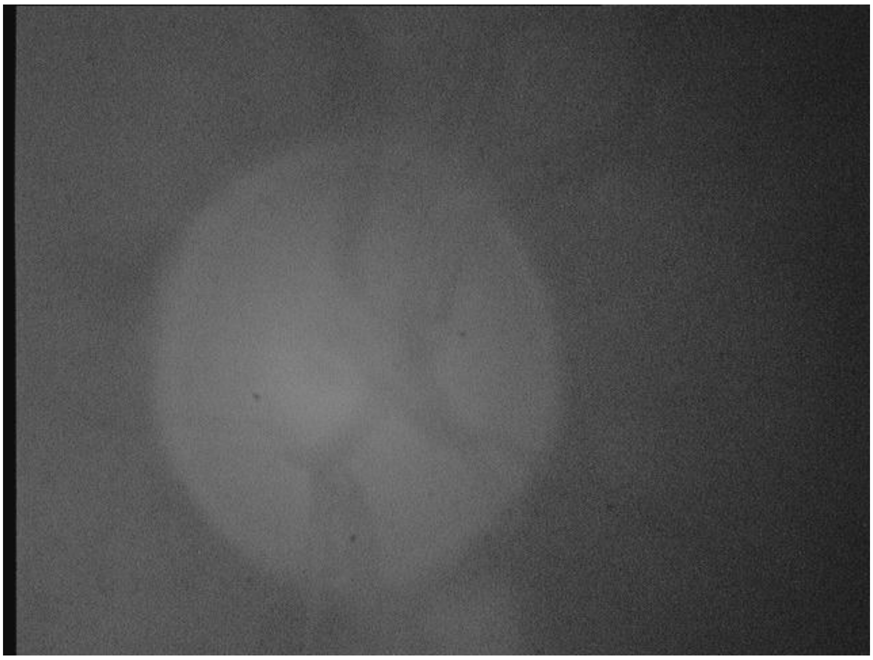

(b)

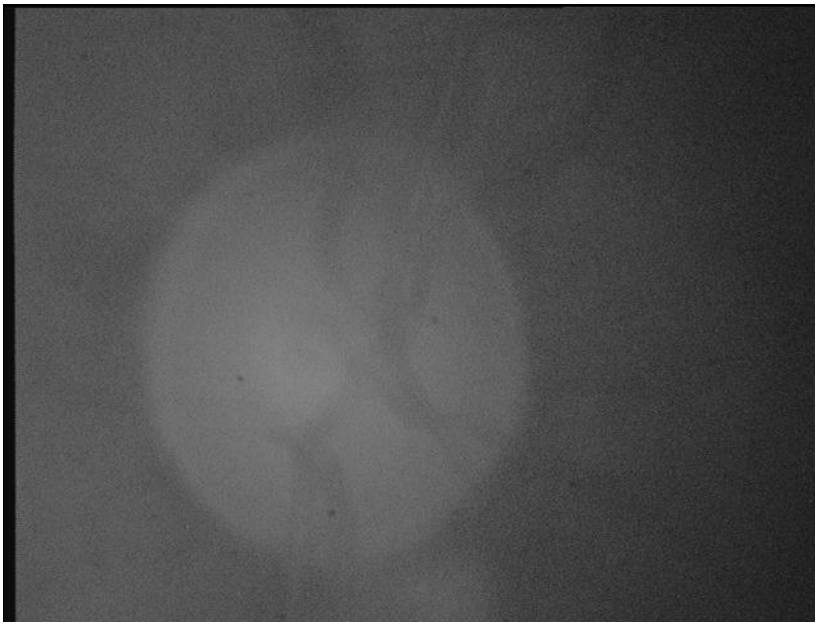

(c)

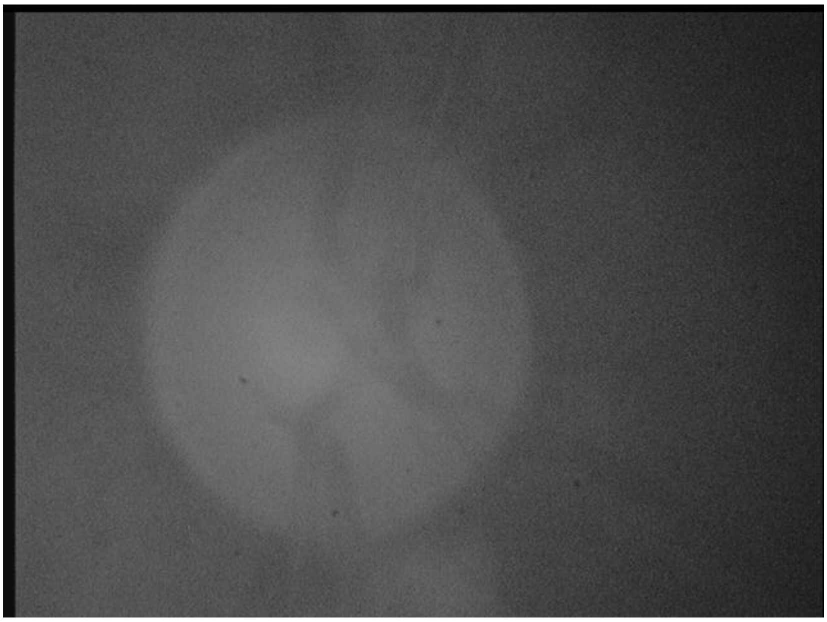

(d)

Figure 5.39 Ocular fundus images. (a) Source image (b) Target image (c) Software aligned image and (d) linear regression curve based aligned image

The locations of regions of interest used for reflectivity calculation are numbered from 1 to 5 is shown in Figure 5.40. The changes in reflectivity of software aligned and linear regression based aligned images are shown in Figure 5.41.

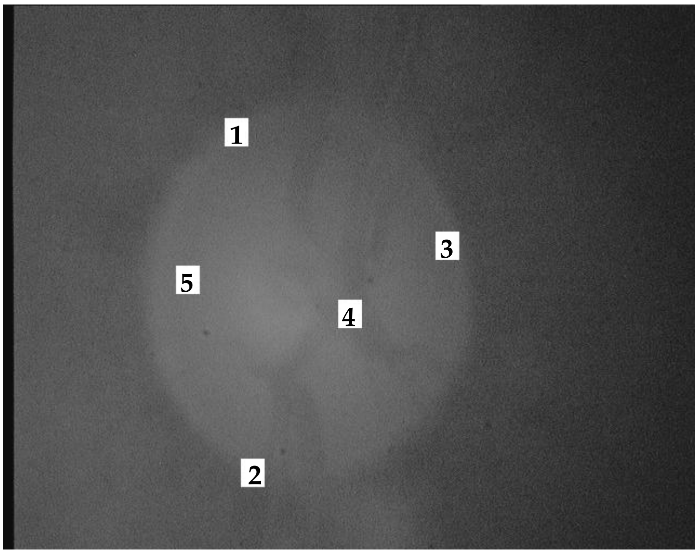

Figure 5.40 Measurement sites at optic disc. The white squares marked with 1 to 5 are the actual sampling areas

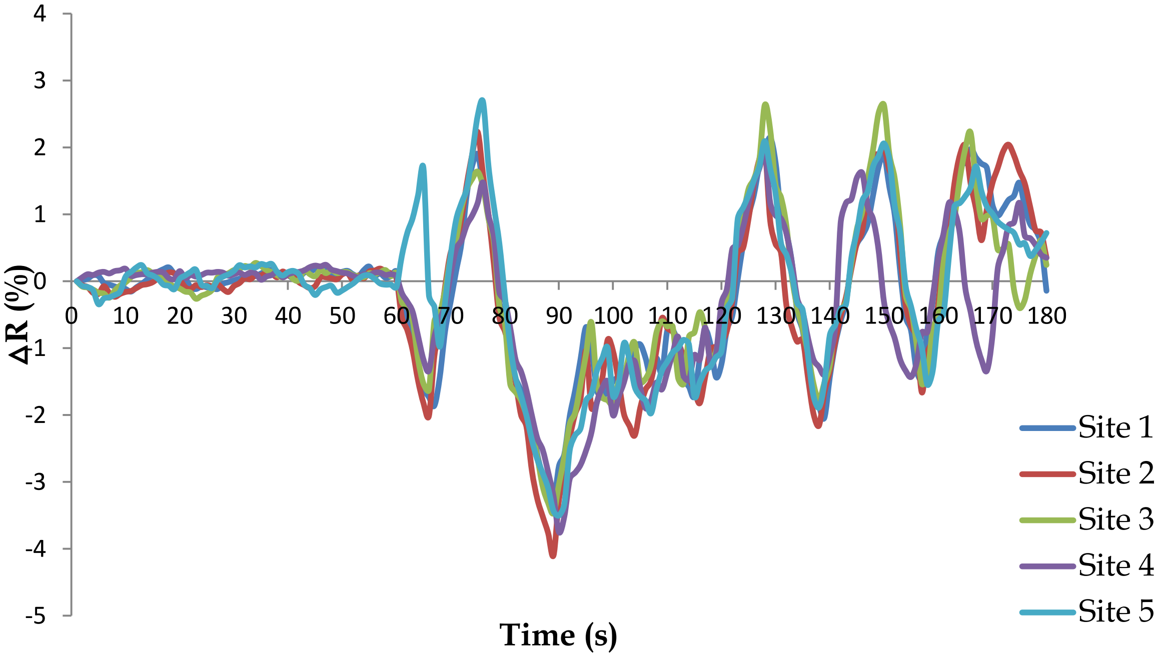

(a)

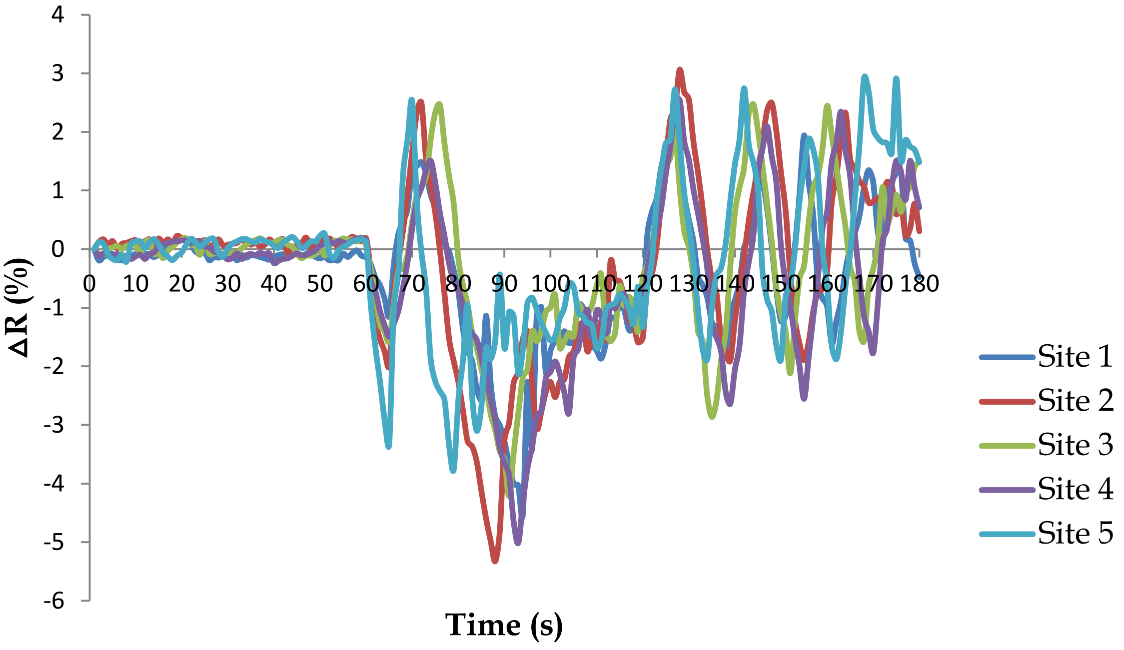

(b)

Figure 5.41 Reflectance variations at the 5 measurement sites. (a) software aligned images (b) linear regression curve based aligned images

The peak reflectance variations at the 5 measurement sites of both software and linear regression based aligned images are presented in Table 5.2

Table 5.2 Peak reflectance variations

Measurement sites	Peak reflectance variations (%)	
	Software based aligned images	Linear regression based aligned images
1	- 3.83	- 4.12
2	- 4.47	- 5.07
3	- 3.89	- 4.11
4	- 4.35	- 4.91
5	- 3.59	- 3.72

A non-invasive method to measure the light reflectance changes in response to diffuse flicker stimulation has been described. The detail description of the development of instrument for functional imaging of human retina has been described. Image registration techniques to minimize the effect of involuntary eye motion were described. Visual stimulus induced changes in reflectance and increased neuronal activity have been obtained. The significant decrease in reflectance is most probably due to the increase in blood volume during stimulation.

Conclusions

In this thesis, non-invasive methods for ocular blood flow measurement are presented. In particular, laser Doppler flowmetry (LDF) technique for the moving red blood cells (RBCs) in the choroidal region of human fundus and ocular fundus reflectometry for measurement of reflectance changes in the optic nerve in presence of visual stimulation was presented.

The experimental activities performed on effect of timolol on subfoveal choroidal blood flow using LDF technique in normal subjects confirms that a drop of timolol produces statistically significant increases the ocular blood flow (43%, $p<0.05$) and ocular perfusion pressure(3.8%, $p<0.05$), and statistically significant decreases in intraocular pressure (16%, $p<0.05$) and heart rate(11%, $p<0.05$). Previous studies [97, 98] showed much weaker effects of timolol on ocular hemodynamics. Therefore our experimental observation requires a deeper investigation, taking also into account that we observed a similar behaviour for the timolol and placebo-treated eyes. Our technique suffers some drawbacks: (i) it does not provide absolute value of blood flow (ii) uncertainty in knowing the sampling volume (iii) optical properties of ocular tissue (iv) angle of impinging and scattering beams (v) changes in pupil diameter.

The experimental activities performed on the effect of one drop of 1% tropicamide using a 4mm artificial pupil directly in front of the cornea does not produce any change in LDF flow parameters (0.7% for Velocity($p>0.05$), 2.8% for Volume($p>0.05$), 1.1% for ChBF ($p>0.05$)). However, we observed statistically significant changes in LDF flow parameters in the measurement performed without any pupil in front of the eye (9.0% for Velocity($p=0.01$), 15% for Volume($p<0.02$), 17% for ChBF ($p<0.01$)). The increases in pupil diameter during both experimental activities are similar. The use of an artificial pupil resulted in Velocity, Volume and ChBF data which were not affected by the pupil dilatation process (2.4% for Velocity ($p>0.05$), 3.1% for Volume ($p>0.05$), 1.3% for ChBF ($p>0.05$)). The changes in pupil diameter resulted in larger scattering angles for the beam emerging out of the pupil and also bigger variations of the location of the incident beam at the pupil and induces large variability in LDF values (5.4% for Velocity ($p<0.05$), 9.0% for Volume ($p=0.03$), 10% for ChBF ($p<0.01$)).

The clinical usages of LDF measurements are limited due to the variations in the measured parameters. We proposed use of an artificial pupil to measure the effect of various pharmacological agents on choroidal blood flow (ChBF) using LDF reduces the variability and increases the sensitivity of this technique to detect the changes in ChBF.

We developed a complete instrument useable for clinical application for the functional imaging of human fundus. Being an instrument used in clinical application, this requires well defined standard and safety regulations. Series of in-vivo measurements demonstrated for proper functions of the system and the results have proved that the functionality of developed system is more encouraging. Two dimensional images of the changes in reflectance induced by increased retinal neuronal activity have been obtained. A significant decrease in reflectance was observed in the temporal sites are most probably due to increase in blood volume during neural stimulation.

Bibliography

1. C.E.Riva, J.E.Grunwald, S.H.Sinclair, and B.L.Petrig. Blood velocity and volumetric rate in human retinal vessels. *Invest. Ophthalmol. Vis. Sci.* 26: 1124–1132, 1984.
2. G.Michelson, M.J.Langhans, and M.J.Groh. Perfusion of the juxtapapillary retina and the neuroretinal rim area in primary open angle glaucoma. *J. Glaucoma.* 5: 91–98, 1996.
3. R.Bonner and R.Nossal. Model for laser Doppler measurement of blood flow in tissue. *Appl. Optics*. 20: 2097-2107, 1981.
4. C.E.Riva, S.D.Cranstoun, J.E.Grunwald, and B.L.Petrig. Choroidal blood flow in the foveal regionof the human fundus. *Invest. Ophthalmol. Vis. Sci.* 35: 4273–4281, 1994.
5. C.E.Riva, S.Harino, B.L.Petrig, and R.D.Shonat. Laser Doppler flowmetry in the optic nerve. *Exp Eye Res*. 55: 499-506, 1992.
6. C.E.Riva, M.Geiser, and B.L.Petrig. Ocular blood flow using continuous laser Doppler flowmetry. *Acta Ophthalmol*. 88: 622-629, 2010.
7. D.Malonek and A.Grinvald. Interactions between electrical activity and cortical microcirculation reealed by imaging spectroscopy: implications for functional brain mapping. *Science*. 272: 551-554, 1996.
8. L.B.Cohen. Changes in neuron structure during action potential and synaptic transmission. Physiol Rev. 53: 373-418, 1973.
9. O.Zarfati, A.Harris, H.J. Garzozi, M. Zacish , L.Kagemann, C.P. Jonescu-Cuypers, and B.Martin. A review of blood flow measurement techniques. *Neuro Ophthalmology*, 24(3): 401-409, 2000.
10. A.Heijl, M.C.Leske, B.Bengsston, and M.Hussein. Measuring visual field progression in the early manifest glaucoma trial. *Acta Ophthalmol Scand.*, 81(3):286-293, 2003.

11. J.W.Keil. The ocular circulation. Integrated systems physiology: From molecule to function. Edited by D.N. Granger and J. Granger. Margan and Claypool life sciences, 2011.
12. C.E.Riva, B.Ross, and G.B. Benedek. Laser Doppler measurements of blood flow in capillary tubes and retinal arteries. *Invest Ophthalmol*, 11(11): 936-44, 1972.
13. G.E.Nilsson, E.G.Salerud, N.O.T.Stromberg, and K.Wardell. Laser Doppler Perfusion Monitoring and Imaging. In: Vo-Dinh T, editor. Biomedical photonics handbook. Boca Raton, Florida: *CRC Press*, 15: 1-24, 2003.
14. International Commission on Illumination - International Lighting Vocabulary. Number 17.4: CIE, 4th edition. ISBN 978-3-900734-07-7.
15. C.E.Riva and B.L.Petrig. *Laser Doppler techniques in ophthalmology. Principles and applications.* In Lasers in Ophthalmology-Basic, Diagnostic and Surgical Aspects edited by Fankhauser, F. and Kwasniewska, S., 51-59, *Kugler Publications*, 2003.
16. C.F.Bohren and D.R.Huffman. *Absorption and Scattering of Light by Small Particles*. Wiley, ISBN 0-471-29340-7, 1983.
17. E.Hecht, *Optics*, Addison Wesley, San Francisco, 2002.
18. J.Mobley and T.Vo-Dinh. *Optical Properties of Tissue, in Biomedical photonics handbook*. T. Vo-Dinh, 2.1 -2.75, CRC Press, 2003.
19. A.Jakobsson and G.E.Nilsson. Prediction of sampling depth and photon path length in laser Doppler Flowmetry. *Med Biol Eng Comput*, 31(3): 301-7, 1993.
20. H.Nilsson and G.E.Nilsson. Monte Carlo simulations of light interaction with blood vessels in human skin in the red-wavelength region In: Priezzhev AV, Asakura T, Briers JD, editors. *Optical Diagnostics of Biological Fluids III, SPIE*, 44-53, 1998.
21. T.P.Newson, A.Obeid, R.S.Wolten, D.Boggett, and P. Rolfe. Laser Doppler velocimetry: the problem of fibre movement artifacts. *J Biomed Eng*, 9:169–172, 1987.

22. M.J.Leahy, F.F.de Mul, G.E.Nilsson, and R.Maniewski. Principles and practice of the laser-Doppler perfusion technique. *Technol Health Care*, 7(2-3): 143-62, 1999.
23. R.J.Gush and T.A.King. Investigation and improved performance of optical fibre probes in laser Doppler blood flow measurement. Med Biol Eng Comput, 678: 29–36, 1987.
24. F.F.M.de Mul, J.van Spijker, D.van der Plas, J.Greve, J.G.Aarnoudse, and T.M.Smits. Mini laser-Doppler (blood) flow monitor with diode laser source and detection integrated in the probe. *Appl Opt*, 23: 2970–2973, 1984.
25. E.Higurashi, R.Sawada, and T.Ito. An integrated laser blood flowmeter. *J Light wave Technol*, 21: 591–595, 2003.
26. A.N.Serov, J.Nieland, S.Oosterbaan, F.F.M.de Mul, H.van Kranenburg, H.H.P.T.Bekman, and W.Steenbergen. Integrated optoelectronic probe including a vertical cavity surface emitting laser for laser Doppler perfusion monitoring. *IEEE Trans Biomed Eng*, 53: 2067–2074, 2006.
27. M.G.D.Karlsson, M.Larsson, T.Stromberg, and K.Wardell. Influence of tissue movements on laser Doppler perfusion imaging. *Proc SPIE* 4624: 106–114, 2002.
28. D.H.Sliney. Laser safety. Lasers in Surg Med, 16: 215-225, 1995.
29. IEC. Laser safety, standards 825. Technical report, International Electrotechnical Commission, Geneva, Switzerland, 2001. Variant A1 and A2 of IEC 60825-1.
30. T.Berendschot, T.J.M.DeLint, P.Jaap, and D.VanNorren. Fundus reflectance –historical and present ideas. *Progress in Retinal and Eye Research*, 22: 171–200, 2003.
31. D.K.Gardiner and J.H.Malcom. Occupational hygiene. *Blackwell publishers*, Third edition, 2005.
32. ISO. Ophthalmic instruments – *fundamental requirements and test methods – part 2: Light hazard protection.* Technical Report 15004-2, Int. Org. Standardization, Geneva, Switzerland, 2007.

33. ANSI – American National Standard for safe use of lasers – ANSI Z136.1, Laser institute of America, Orlando, USA, 2007.
34. M.D.Stern. In vivo evaluation of microcirculation by coherent light scattering. *Nature*, 254: 56–58, 1975.
35. D.Watkins and G.A.Jr.Holloway. An instrument to measure cutaneous blood flow using the Doppler shift of laser light. *IEEE Trans Biomed Eng*, BME-25: 28–33, 1978.
36. G.E Nilsson, T.Tenland, and P.A.Oberg. Evaluation of a laser Doppler flowmeter for measurement of tissue blood flow. *IEEE Trans Biomed Eng*, BME-27: 597–604, 1980.
37. G.E.Nilsson. Signal processor for laser Doppler tissue flowmeters. *Med Biol Eng Comput,* 22: 343–348, 1984.
38. A.P.Shepherd and P.A.Oberg, *Laser-Doppler blood flowmetry*, Kluwer Academic Publishers, Boston, 1990.
39. V.Rajan, B.Varghese, T.G.Van Leeuwen, and W.Steenbergen. Review of methodological developments in laser Doppler flowmetry. *Lasers in Medical Science,* 24(2):269-83, 2009.
40. R.Lohwasser and G.Soelkner. Experimental and theoretical laser-Doppler frequency spectra of a tissue like model of a human head with capillaries. *Applied Optics*, 38(10): 2128-2137, 1999.
41. O.Andree Larsen, N.A.Lassen, and F.Quaade. Blood Flow through Human Adipose Tissue Determined with Radioactive Xenon. A*cta Physiologica Scandinavica,* 66(3): 337-345, 1966.
42. A.M.Rudolph and M.A.Heymann. The Circulation of the Fetus in Utero: Methods for Studying Distribution of Blood Flow, Cardiac Output And Organ Blood Flow. *Circulation Research*, 21(2): 163-184, 1967.
43. M.A.Heymann, B.D.Payne, J.I.Hoffman, and A.M.Rudolph. Blood flow measurements with radionuclide-labeled particles. *Progress in Cardiovascular Diseases*, 20(1): 55-79, 1977.

44. C.M.Black, R.P.Clark, K.Darton, M.R.Goff, T.D.Norman, and H.A.Spikes. A pyroelectric thermal imaging system for use in medical diagnosis. *Journal of Biomedical Engineering*, 12(4): 281-6, 1990.
45. S.Bornmyr, H.Svensson, B.Lilja, and G.Sundkvist. Skin temperature changes and changes in skin blood flow monitored with laser Doppler flowmetry and imaging: a methodological study in normal humans. *Clinical Physiology*, 17(1): 71-81, 1997.
46. A.Merla and G.L.Romani. Functional Infrared Imaging in Medicine: A Quantitative Diagnostic Approach. *In Engineering in Medicine and Biology Society, 2006. EMBS '06. 28th Annual International Conference of the IEEE*, 2006.
47. J.Bellmunt, M.Navarro, S.Morales, L.Jolis, J.Carulla, H.Knobell, M.Vilardell, and L.A.Sole. Capillary microscopy is a potentially useful method for detecting bleomycin vascular toxicity. *Cancer,* 65:303-309, 1990.
48. D.J.Pine, D.A.Weitz, P.M.Chaikin, and E.Herbolzheimer. Diffusing-Wave Spectroscopy. *Physical Review Letters*, 60(12): 1134-1137, 1988.
49. G.S.Brindley and E.N.Willmer. The reflexion of light from macular and peripheral fundus oculi in man. *J. Physiol*, 116(3): 350-356, 1952.
50. W.M.Buchanan, T.Gloster, and D.P.Greaves. Examination of the choroidal circulation in vivo. *J.Physiol*. 162:P2, 1962.
51. K.Mizuno, A.Majima, K.Ozawa, and H.Ito. Red-free light fundus photography. *Invest. Ophthalmol. Vis. Sci,* 7 (3): 241-249, 1968.
52. R.W.Flower, D.S.McLeod, and S.M.Pitts. Reflection of light by small areas of the ocular fundus. *Invest. Ophthalmol. Vis. Sci,* 16(10):981-985, 1977.
53. H.Ridley. Television in ophthalmology. *Proceedings of the 16th International Congress of Ophthalmology, London*, 2: 1397-404, 1950.
54. A.M.Potts and M.C. Brown. A colour television ophthalmoscope. *Trans Am Acad Ophthalmol Otolaryngol* , 62: 136-7, 1958.
55. W.M.Haining. Video funduscopy and fluoroscopy. *British journal of ophthalmology*, 65:702-706, 1981.

56. R.H.Webb, G.W.Hughes, and F.C.Delori. Confocal scanning laser ophthalmoscope. *Applied optics*, 26(8): 1492-1499, 1987.
57. R.H.Webb and G.W. Hughes. Scanning laser ophthalmoscope. *IEEE trans. Biomed. Eng.*, 28(7): 488-492, 1981.
58. R.H.Webb, G.W.Hughes, and O.Pomerantzeff. Flying spot TV ophthalmoscope. *Appl. Opt*, 19: 2991-2997, 1979.
59. T.Wilson and C.J.R.Sheppard. Theory and Practice of Scanning Optical Microscopy. Academic Press London, 1984.
60. J.Ossewaarde-Van Norel, P.R.van Den Biesen, J.van De Kraats, T.T.Berendschot, and D.van Norren. Comparison of fluorescence of sodium fluorescein in retinal angiography with measurements in vitro. *J Biomed Opt.*, 7(2):190-198, 2002.
61. A.Plesch and U.Klingbeil. 1988. Confocal laser scan system for imaging and analysis of the fundus. *Fortschr. Ophthalmol.*, 85(5): 565–568, 1988.
62. R.P.Tornow, S.Beuel, and E.Zrenner. Modifying a rodenstock scanning laser ophthalmoscope for imaging densitometry. *Appl. Opt.*, 36(22):5621–5629, 1997.
63. P.Vieira, A.Manivannan, C.S.Lim, P.Sharp, and J.V.Forrester. Tomographic reconstruction of the retina using a confocal scanning laser ophthalmoscope. *Physiol. Meas*. 20(1): 1–19, 1999.
64. A.Manivannan, H.J.Van der, P.Vieira, A.Farrow, J.Olson, P.F.Sharp, and J.V.Forrester. Clinical investigation of a true color scanning laser ophthalmoscope. *Arch. Ophthalmol*, 119(6): 819–824, 2001.
65. A.E.Elsner, Q.Zhou, F.Beck, P.E.Tornambe, S.A.Burns, J.J.Weiter, and A.W.Dreher. Detecting AMD with multiply scattered light tomography. *Int. Ophthalmol.*, 23(4-6): 245–250, 2001.
66. D.Schweitzer, M.Hammer, and M.Scibor. Imaging spectrometry in ophthalmology- principle and applications in microcirculation and in investigation of pigments. *Ophthalmic Res.*, 28(Suppl. 2): 37–44, 1996.

67. T.T.J.M.Berendschot, P.J.DeLintb, and D.van Norren. Fundus reflectance – historical and present ideas. *Progress in Retinal and Eye Research*, 22: 171-200, 2003.

68. D.Van Norren and J.Van De Kraats. Imaging retinal densitometry with a confocal scanning laser ophthalmoscope. *Vision research*, 29(12): 1825-1830, 1989.

69. F.C.Delori and K.P.Pflibsen. Reflectance properties of the optic disc non-invasive assessment of the visual system. *Technical Digest Series, Optical Society of America, Washington, DC,* 7:154–157, 1989.

70. F.C.Delori**.** Spectrophotometer for noninvasive measurement of intrinsic fluorescence and reflectance of the ocular fundus. *Applied optics*, 33(31): 7439-7452, 1994.

71. M.Hammer, D.Schweitzer, L.Leistritz, M.Scibor, K.H.Donnerhacke, and J.Strobel. Imaging spectroscopy of the human ocular fundus in-vivo. *J. Biomed. Opt.*, 2: 418–425, 1997.

72. J.M.Gorrand and F.C.Delori. A reflectometric technique for assessing photoreceptor alignment. *Vision Res.*, 35: 999–1010, 1995.

73. C.E.Riva. New ocular fundus reflectometer. *Applied optics*, 11(8): 1845-1849, 1972.

74. E.A.Boettner and J.R.Wolter. Transmission of the ocular media. *Invest. Ophthalmol.* 1: 777-783, 1962.

75. F.C.Delori and K.P.Pflibsen. Spectral reflectance of the human ocular fundus. *Applied optics,* 28(6):1062–1077, 1989.

76. G.Michelson, M.J.Langhans, and M.J.M.Groh. Clinical investigation of the combination of a scanning laser ophthalmoscope and laser Doppler flowmeter. *Ger. J. Ophthalmol.*, 4(6): 342-349, 1995.

77. T.Gherezghiher, H.Okubo, and M.C.Koss. Choroidal and ciliary body blood flow analysis: Application of laser Doppler flowmetry in experimental animals. *Exp. Eye Res.*, 53(2):151-156, 1991

78. J.W.Kiel and A.P.Shepherd. Autoregulation of choroidal blood flow in the rabbit. *Invest Ophthalmol Vis Sci.*, 33(8): 2399-2410, 1992.

79. C.E.Riva, C.J.Pournaras, C.L.Poitry Yamate, and B.L.Petrig. Rhythmic changes in velocity, volume, and flow of blood in the optic nerve head tissue. *Microvasc Res.*, 40(1):36-45, 1990.

80. C.E.Riva, S.D.Cranstoun, R.Mann, and C.E.Barnes. Local choroidal blood flow in the cat by laser Doppler flowmetry. *Invest Ophthalmol Vis Sci.*, 35(2): 608-618, 1994.

81. E.Friedman. Update of the vascular model of AMD. *Br J Ophthalmol*. 88(2): 161-163, 2004.

82. J.E.Grunwald, S.M.Hariprasad, J.DuPont, M.G.Maguire, S.L.Fine, A.J.Brucker, A.M.Maguire, and A.C.Ho. Foveolar choroidal blood flow in age-related macular degeneration. *Invest. Ophthalmol. Vis. Sci.*, 39(2):385–390, 1998.

83. T.A.Ciulla, A.Harris, and B.J.Martin. Ocular perfusion and age-related macular degeneration. *Acta Ophthalmol. Scand.*, 79(2): 108–115, 2001.

84. M.E.Fitzgerald, E.Tolley, S.Frase, Y.Zagvazdin, R.F.Miller, W.Hodos, and A.Reiner. Functional and morphological assessment of age-related changes in the choroid and outer retina in pigeons. *Vis. Neurosci.,* 18(2):299–317, 2001.

85. L.Schmetterer and M.Wolzt. Ocular blood flow and associated functional deviations in diabetic retinopathy. *Diabetologia*, 42(4): 387–405, 1999.

86. A.Harris, L.Kagemann, and G.A.Cioffi. ssessment of human ocular hemodynamics. *Surv. Ophthalmol*. 42(6): 509–533, 1998.

87. M.P.Leonard. Temperature modulating action of choroidal blood flow. *Eye*, 5: 181- 185, 1991.

88. J.J.Steinle, D.K.Agbas, and P.G.Smith. Regional regulation of choroidal blood flow by automatic innervation in the rat. *American journal of physiology*, 279(1): R202-R209, 2000.

89. J.Sebag, M.Tang, S.Brown, A.A.Sudan, and M.A.Charles. Effect of pentoxifylline on choroidal blood flow in nonproliferative diabetic retinopathy. *The journal of vascular diseases*, 45(6): 429-433, 1994.

90. B.L.Petrig, J.P.Gehrig, and P.Pompili. New multi-channel DSP based laser Doppler flowmetry analysis system for quantification of ocular blood flow. *Proce. of SPIE 4156*, 318-327, 2000.

91. J.E.Grunwald. Effect of timolol on the human retinal circulation. *Invest Ophthalmol Vis Sci*, 27(12):1713-1719, 1986.

92. I.M.Katz, W.A.Hubbard, A.J.Getson, and A.L.Gould. Intraocular pressure decrease in normal volunteers following timolol ophthalmic solution. *Invest Ophthalmol.* 15(6): 489-492, 1976.

93. T.J.Zimmerman and H.E.Kaufman. Timolol, a beta-adrenergic blocking agent for the treatment of glaucoma. *Arch. Ophthalmol.*, 95(4): 601-604, 1977.

94. R.L.Radius, G.R.Diamond, I.P.Pollack, and M.E.Langham. Timolol, a new drug for management of chronic simple glaucoma. *Arch. Ophthalmol.*, 96(6): 1003-1008, 1978.

95. C.L.Leier, N.D.Baker, and P.A.Weber. Cardiovascular effects of ophthalmic timolol. *Annals of internal medicine*, 104(2):197-199, 1986.

96. J.E.Grunwald and C.Furubayashi. Effect of topical timolol maleate on the ophthalmic artery blood pressure. *Invest Ophthalmol. and Vis Sci.,* 30(6):1095-1100, 1989.

97. J.E.Grunwald. Effect of timolol maleate on the retinal circulation of human eyes with ocular hypertension. *Invest Ophthalmol and Vis Sci.*, 31(3): 521-526, 1990.

98. J.E.Grunwald. Effect of two weeks of timolol maleate treatment on the normal retinal circulation. *Invest Ophthalmol and Vis Sci.*, 32(1): 39-45, 1991.

99. R.P.Wilson, N.Kanal, and G.L.Spaeth. Timolol: its effectiveness in different types of glaucoma. *Trans Am Acad Ophthalmol*, 86(1): 43-50, 1979.

100. R.L.Coakes and R.F.Brubaker. The mechanism of timolol in lowering intraocular pressure. *Arch Ophthalmol.* 96(11):2045-2048, 1978.

101. J.W.Kiel and P.Patel. Effects of timolol and betaxolol on choroidal blood flow in the rabbit. Exp. Eye Res., 67: 501-507, 1998.

102. A.L.Cohen. Ultrastrucutral aspects of human optic nerve. Invest Ophthalmol. and Vis. Sci., 6(3): 294-308, 1967.

103. F.Robinson, C.Sanford, B.L.Petrig, J.E.Grunwald, and C.E.Riva. The acute effect of topical epinephrine on macular blood flow in humans. *Invest Ophthalmol. and Vis. Sci.*, 33(1): 18-22,1992.

104. A.H.Neufeld. Experimental studies on the mechanism of action of timolol. *Surv Ophthalmol.*, 23(6): 363-370, 1979.

105. G.Richard and J.Weber. Influence of beta blockers timolol and pindolol on retinal hemodynamics: A video-angiography study. *Klinische Monatsblatter fur Augenheilkunde,* 190(1):34-39, 1987.

106. W.Gunther, R.Hemma, G.Gerbard, F.M.Gabriele, and S.Leopolad. Effects of topical clonidine versus brimonidine on choroidal blood flow and intraocular pressure during squatting. *Invest Ophthalmol. and Vis. Sci.,* 48 (9): 4220-4224, 2007.

107. N.Palanisamy, L.Rovati, M.Cellini, C.Gizzi, E.Strobbe, E.C.Campos, and C.E.Riva. Effect of timolol on sub-foveal choroidal blood flow using laser Doppler flowmetry. *Proceedings of SPIE*, 7885: 78850E1 – 78850E9, 2011.

108. C.E.Riva, B.L.Petrig, and J.E.Grunwald. *Retinal blood flow*. In Laser-Doppler blood flowmetry edited by A.P.Shepered and P.A.Oberg, Developments in cardio-vascular medicine. Kluwer Academic Publishers, Boston, 107: 349-383, 1989.

109. H.Z.Cummins and H.L.Swinney HL. *Light beating spectroscopy*. In Progress in optics, Volume VIII edited by E.Wolf, North Holland Publishing Company, Amsterdam, 133-200, 1970.

110. D.Deldado, P.Michel, and S.D.Jaanus. Effect of tropicamide on ocular blood flow in the rabbit. *Am J Optom Physiol Opt.*, 59(5): 410-412, 1982.

111. F.Robinson, B.L.Petrig, S.H.Sinclair, C.E.Riva, and J.E.Grunwald. Does topical phenylephrine, tropicamide, or proparacaine affect macular blood flow?. *Ophthalmology,* 92(8): 1130-1132, 1985.

112. T.Tomihiko, K.Itaru, O.Yuichiro, and M.Yukihiko. Effects of tropicamide and phenylephrine on optic nerve circulation evacuate by scanning laser Doppler flowmeter. *Journal of Eye*, 18: 414-416, 2001.

113. R.Bonner and R.Nossal. *Principles of laser-Doppler flowmetry*. In Laser-Doppler blood flowmetry edited by A.P.Shepered and P.A.Oberg, Developments in cardio-vascular medicine. Kluwer Academic Publishers, Boston, 107: 17-45, 1990.

114. J.Takayama, A.Mishima, and K.Ishii. Effect of topical phenylephrine on blood flow in posterior segments of monkey and aged human eyes. *Jpn. J. Ophthalmol*, 48: 243-248, 2004.

115. N.Palanisamy, C.E.Riva, L.Rovati, M.Cellini, C.Gizzi, E,Strobbe and E.C.Campos. Does tropicamide affect choroidal blood flow in humans?- A laser Doppler flowmetry study. *Proceedings of SPIE*, 8209, 2012.

116. E. Berman, *Biochemistry of the Eye*. Plenum Press, 1991.

117. C.E.Riva, E.Logean, and B.Falsini., Visually evoked hemodynamical response and assessment of neurovascular coupling in the optic nerve and retina. *Prog. Retin. Eye Res.*, vol. 24, 2005.

118. M.Crittin and C.E.Riva. Functional imaging of the human papilla and peripapillary region based on flicker-induced reflectance changes. *Neuro sci. Lett.*, vol. 360, 2004.

119. G.Hanazono, K.Tsunoda, K.Shinoda, K Tsubota, Y.Miyake, and M.Tanifuji. Intrinsic signal imaging in macaque retina reveals different types of flash induced light reflectance changes of different origins. *Invest. Ophthalmol. Vis.Sci.*, vol. 48(6), 2007.

120. C.E.Riva, E.Logean, and B.Falsini. Temporal dynamics and magnitude of the blood flow response at the optic disk in normal subjects during functional retinal flicker-stimulation. *Neuro sci. Lett.*, vol. 356, 2004.

121. M.Crittin and C.E.Riva. Optic nerve and retinal reflectance changes in response to physiological stimuli. *Optics and Laser in Engineering,* Vol. 43, 583-589, 2005.

122. J.Millman and C.Halkias. *Integrated electronics: analog and digital circuits and systems*. McGraw Hill, 1972.

123. A.V.Cideciyan. Registration of fundus *images. IEEE Engineering in medicine and biology,* 14(1): 52-58, 1995.

124. B.Zitova and J.Flusser,J. Image registration methods: a survey. *Image and Vision Computing*, 21: 977-1000, 2003.

125. A.J.B.Maintzand M.A.Viergever. A survey of medical image registration. *Medical Image Analysis*, 2(1):1-36, 1998.

126. B.Rezaie and M.D.Srinath. Algorithms for fast image registration. *IEEE transactions on Aerospace and Electronic Systems*, 20(6):716-727, 1984.

127. B.K.P.Horn. *Robot Vision.* McGraw Hill, 130-132, 1986.

128. P.A.Devijver and J.Kittler. *Pattern recognition*: A statistical approach. Prentice-Hall international, 232, 1982

129. D.I.Barnea and H.F.Silverman. A class of algorithms for fast digital image registration. *IEEE Trans. Computers*, 21(2): 179–186, 1972.

130. H.Li and O.Chutatape. Fundus image features extraction. *Proceedings of the 22nd Annual EMBS international conference - Chicago*, 3071-3073, 2000.

131. F.L.Bookstein. Thin-plate splines and the atlas problem for biomedical images. *Information processing in medical imaging*, 511:326-342, 1991.

132. W.S.Kerwin and C.Yuan. Active edge maps for medical registration. *Proceedings of the SPIE*, 4322: 516-526, 2001.

133. W.S.V.Shih, W.C.Lin, and C.T.Chen. Contour model guided nonlinear deformation model for intersubject image registration. *Proceedings of the SPIE,* 3034: 611-620, 1997.

134. X.Dai and S.Khorram. A feature-based image registration algorithm using improved chain-code representation combined with invariant moments. *IEEE transactions on Geoscience and remote sensing*, 37(5): 2351-2362, 1999.

135. S.Periaswamy and H.Farid. Elastic registration in the presence of intensity variations. *IEEE transactions on medical imaging*, 22(7): 865-874, 2003.
136. R.J.Althof, G.J.Wind, and J.T.Dobbins. A rapid and automatic image registration algorithm with subpixel accuracy. *IEEE transactions on medical imaging*, 16(3): 308-316, 1997.
137. E.H.Adelson and J.R.Bergen. Spatiotemporal energy models for the perception of motion. *Journal of the optical society of America*, 2(2): 284-299, 1985.
138. J.K.Aggarwal and N.Nandhakumar. On the computation of motion for sequences of images – a review. *Proceedings of IEEE*, 76(8): 917-935, 1988.
139. J.L.Barron, D.J.Fleet, and S.S.Beauchemin. Performance of optical flow techniques. *International journal of computer vision*, 12(1): 43-77, 1994.
140. K.Berberidis and I.Karybali. A new efficient cross-correlation based image registration technique with improved performance. *Proceedings of 11th European signal processing conference- France*, 2002.
141. P.Thevenaz, U.E.Ruttimann, and M.Unser. A pyramid approach to subpixel registration. *IEEE transactions on Image Processing*, 7(1): 27-41, 1998.